PLASMA DYNAMICS

XII. PLASMA DYNAMICS

Academic and Research Staff

Prof. William P. Allis
Prof. George Bekefi
Prof. Abraham Bers
Prof. Flora Y. F. Chu
Prof. Bruno Coppi
Prof. Thomas H. Dupree
Prof. Elias P. Gyftopoulos
Prof. Hermann A. Haus
Prof. Lawrence M. Lidsky
Prof. James E. McCune
Prof. Peter A. Politzer
Prof. Dieter J. Sigmar
Prof. Louis D. Smullin
Prof. James T. Woo
Dr. Bamandas Basu
Dr. Giuseppe Bertin
Dr. George L. Johnston
Dr. David J. Kaup
Dr. Giampietro Lampis
Dr. Kim Molvig
Dr. Francesco Pegoraro
Dr. Tiete Schep
Dr. Daan Schram
Kevin Hunter
John J. McCarthy
William J. Mulligan
Allan H. Reiman

Graduate Students

Charles T. Breuer
Warren K. Brewer
Leslie Bromberg
Timothy A. Brunner
Natale M. Ceglio
Frank W. Chambers
Hark C. Chan
Franklin R. Chang
Tsi-Pin Choong
Wing Shek Chow
Paul W. Chrisman, Jr.
John A. Combs
Donald L. Cook
David A. Ehst
Antonio Ferreira
Nathaniel J. Fisch
Alan S. Fisher
Jay L. Fisher
Alan R. Forbes
Ricardo M. O. Galvao
Keith C. Garel
Mark Gottlieb
James S. Herring
Ady Hershcovitch
Steven P. Hirshman
James C. Hsia
Dennis J. Huber
Saeed Z. Jabbawy
Mark D. Johnston
David L. Kaplan
Masayuki Karakawa
Charles F. F. Karney
Peter T. Kenyon
David S. Komm
Craig M. Kullberg
John L. Kulp, Jr.
David B. Laning
Ping Lee
Edward W. Maby
Francois Martin
Mark L. McKinstry
Thomas J. McManamy
John L. Miller
Paul E. Morgan
Thaddeus Orzechowski
David O. Overskei
Aniket Pant
Louis R. Pasquarelli
Robert E. Potok
Robert H. Price
Donald Prosnitz
John E. Rice
Burton Richards
Kenneth Rubenstein
Richard E. Sclove
Michael D. Stiefel
David S. Stone
Miloslav S. Tekula
David J. Tetrault
Kim Theilhaber
Clarence E. Thomas
Alan L. Throop
Ben M. Tucker
Ernesto C. Vanterpol
Marcio L. Vianna
Yi-Ming Wang
David M. Wildman
Michael A. Zuniga

XII. PLASMA DYNAMICS

A. Basic Plasma Research

1. NONLINEAR WAVE INTERACTIONS AND SYMBOLIC COMPUTATIONS

National Science Foundation (Grant ENG75-06242)

Abraham Bers, George L. Johnston, Kevin Hunter, Nathaniel J. Fisch,
John L. Kulp, Jr., Allan H. Reiman, Alan E. Throop

During the past year we have completed three studies of nonlinear interactions in a plasma.[1-3] The first two have direct bearing on understanding and describing laser-plasma (pellet) interactions and RF plasma heating in general. In the third study we have achieved an analytic description of the onset of nonlaminarity in streaming instabilities, and this deepens our understanding of one of the most fundamental of plasma instabilities, the beam-plasma interaction. Each of these studies has produced a doctoral thesis, and the results have been presented at various national[4,5] and international[6-8] plasma meetings. Journal articles are being prepared for publication.

We have successfully arrived at a rather complete solution of the three-wavepacket nonlinear interaction problem in time and space.[9-11] Thus we have been able to show that certain decay interactions can lead to the generation of solitons, and that explosive instabilities (negative and positive energy wave interactions) have a threshold that depends on the wavepacket extent. We have also determined in what way the reflection in backscattering interactions depends upon pulse shape. We have recently generalized our results to describe such nonlinear interactions in two dimensions in steady state, and to account for plasma inhomogeneities. We plan to pursue this work to obtain a broad understanding of this fundamental nonlinear problem. Our approach makes use of the powerful analytical methods of inverse scattering, together with computer simulations and symbolic computation.

We have also discovered a new and simple way of formulating equations for strong turbulence in plasmas.[12,13] Thus we have shown how resonance-broadening corrections can be found for all weak-turbulence interactions. We plan to pursue this further to find out how our results extend to interactions in more than one dimension, and to plasmas in a magnetic field.

Our plans also include the active use of symbolic computation in all aspects of our work. Use of the computer system MACSYMA has become habitual within our group. Our pioneering work in achieving this will be detailed in a forthcoming report.[14]

References

1. D. C. Watson, "Third-Order Theory of Pump-Driven Plasma Instabilities — Laser-Pellet Interactions," Ph.D. Thesis, Department of Electrical Engineering, M. I. T., February 1975.

2. F. W. Chambers, "Space-Time Evolution of Instabilities in Laser-Plasma Interactions," Ph.D. Thesis, Department of Physics, M. I. T., August 1975.

3. M. L. Vianna, "Theory of Beam-Plasma Interaction in a Longitudinal Density Gradient," Ph.D. Thesis, Department of Physics, M. I. T., May 1975.

4. D. C. Watson and A. Bers, "Magnetized Vlasov Wave Coupling and Lower Hybrid-to-Bernstein Parametric Downconversion," Bull. Am. Phys. Soc., Ser. II, 20, 1376 (1975).
5. F. W. Chambers and A. Bers, "One-Dimensional Inhomogeneous Coupling of Modes in a Finite Interaction Length," Bull. Am. Phys. Soc., Ser. II, 20, 1367 (1975).
6. A. Bers, "Three-Dimensional Stability Analysis for Coupled Waves," in R. C. Cross (Ed.), Proceedings of the U. S.-Australian Workshop on Plasma Waves, University of Sydney, Australia, 1975, pp. 19.1-19.4.
7. A. Bers, "Three-Dimensional Pulse Shapes of Laser-Plasma Instabilities," in R. C. Cross (Ed.), Proceedings of the U. S.-Australian Workshop on Plasma Waves, University of Sydney, Australia, 1975, pp. 20.1-20.6.
8. A. Bers, "Theory of Beam-Plasma Interactions," Survey Lecture, International Congress on Waves and Instabilities in Plasmas, Innsbruck, Austria, March 1975.
9. A. Reiman, D. J. Kaup, and A. Bers, "Time-Space Evolution of Nonlinear Pulse Interactions in a Homogeneous Plasma – Theory and Simulation," Bull. Am. Phys. Soc., Ser. II, 20, 1291 (1975).
10. D. J. Kaup, A. Reiman, and A. Bers, "Nonlinear Evolution of Stimulated Back-scattering," Bull. Am. Phys. Soc., Ser. II, 20, 1291 (1975).
11. A. Bers and A. Reiman, "Time-Space Evolution of 3-Wave Interactions in an Inhomogeneous Plasma," Bull. Am. Phys. Soc., Ser. II, 20, 1291 (1975).
12. N. J. Fisch and A. Bers, "Resonance Broadening for Wave-Particle and Wave-Wave Turbulence," Phys. Rev. Letters 35, 373 (1975).
13. N. J. Fisch and A. Bers, "Model for New Renormalized Turbulence Equations," Bull. Am. Phys. Soc., Ser. II, 20, 1367 (1975).
14. J. L. Kulp, C. F. F. Karney, and A. Bers, "Symbolic Computation in Nonlinear Plasma Wave Interactions," R. L. E. and Project MAC Report, M. I. T., 1975 (in preparation).

2. STUDIES OF NONLINEAR WAVE-PARTICLE INTERACTIONS

National Science Foundation (Grant ENG75-06242)

Peter A. Politzer, Ady Hershcovitch

Recent work on plasma theory has concentrated on analyses of the nonlinear interactions between the plasma and the self-consistent electromagnetic radiation fields. Interpretation of experimental observations in terms of theoretical predictions has been hampered because of the generally complex nature of the interaction between a plasma and the device in which it is produced. In order to study in detail the phenomenon of nonlinear wave-induced diffusion of plasma particles, and to overcome many of the experimental problems, we use a counterstreaming electron-beam facility, which represents a close approximation to the idealized plasma models used in theoretical calculations. In this device we are able to observe the time history of both the particle distribution function and the electric field spectrum. We are specifically concerned with the nonlinear evolution of the "half-cyclotron frequency" instability that occurs spontaneously in this device. Using the formalism developed by T. H. Dupree and others, we have calculated the nonlinear velocity space diffusion coefficients appropriate to this unstable system. The experimental configuration allows direct measurement of this diffusion and thus good comparison with the theory. These theories of plasma turbulence also distinguish between resonant and nonresonant wave-particle interactions, as well as between large-amplitude single-wave effects and the effects of broadband turbulence. In particular, we have shown that the presence of a broad turbulent-wave spectrum should significantly modify the velocity space diffusion coefficient and lead to stabilization of the half-cyclotron instability. We are now undertaking to test this prediction by application of a controlled spectrum of turbulent electric fields to the electron beams. These calculations and experiments should provide a direct test of the theory of wave-induced diffusion of particles in velocity space, and indicate applications of this theory to more complex plasma configurations.

3. TRAPPED-PARTICLE EXPERIMENTS

National Science Foundation (Grant ENG75-06242)

Lawrence M. Lidsky, Louis R. Pasquarelli

We have developed the theory of the cylindrical geometry analog of the toroidal trapped-particle mode predicted by B. Coppi and used this theory to predict the behavior of a particular set of trapped-particle modes. These modes were detected, their linear properties have been measured, and the results have been published. We are now investigating the saturation mechanism of these modes, paying particular attention to the effect of weak electron-neutral collisions. The experimental apparatus on which the earlier measurements were conducted has been improved so that we can operate in a lower collision frequency regime.

4. DRIFT-WAVE TURBULENCE

National Science Foundation (Grant ENG75-06242)

Thomas H. Dupree, David J. Tetrault

Great progress has been made in obtaining the solution to the nonlinear equations describing drift-wave turbulence. Many of the features of the spectrum observed experimentally are predicted by the solutions. In the collisionless case there is good agreement for the number of modes observed and the amplitude and frequency width of each mode. The theory also predicts the very interesting transition between the single, zero-width mode spectrum of the collisional case and the many-mode, finite-width collisionless case. The transition occurs at the point where inertial and viscous effects are equal. The basic concepts used to gain an understanding of drift-wave turbulence appear to have wide application to other kinds of plasma turbulence.

5. INTENSE RELATIVISTIC ELECTRON BEAMS

National Science Foundation (Grant ENG75-06242)

U.S. Energy Research and Development Administration (Contract E(11-1)-2766)

George Bekefi, Thaddeus Orzechowski

During the past year, we have studied the motion of electrons and ions in a relativistic diode subjected to a crossed magnetic field. This work has been largely completed. We have found that the electron motion agrees with predictions from theory that take account in a self-consistent way of the self-electric and self-magnetic fields in the diode.

We have also found that the motion of plasma can be substantially reduced by an externally imposed crossed magnetic field of several kilogauss. This slowing down of plasma motion agrees with a magnetohydrodynamic computer code for the case of moving hydrogen plasma.

During the coming year, we shall concentrate on two areas of study.

a. Our relativistic diode is a crossed-beam microwave device and we already have evidence of copious microwave radiation. Our program is to study the microwave spectrum ranging from 3-cm wavelengths down to 8-mm wavelengths.

b. A relativistic electron diode also has great potential as a source of intense ion beams. We have begun a study of various promising geometries, using the perpendicular magnetic field as a means of suppressing electron motion.

6. CHARGE EXCHANGE IN OPTICALLY EXCITED ALKALI METAL VAPORS

National Science Foundation (Grant ENG75-06242)

Edward W. Maby, Louis D. Smullin, Richard R. Freeman

A promising means of heating a plasma to the high temperatures required to support a controlled fusion process is by injection of high-energy neutral hydrogen. This neutral beam may best be produced by converting the low-energy output of an H^+ ion source into H^- ions by means of a double charge-exchange reaction with cesium, accelerating the H^- ions to the desired energy and neutralizing the beam by stripping away the excess electrons. We intend to study this charge-exchange mechanism in detail and to investigate improvement in its efficiency by optically exciting the cesium. Work on this project began September 1, 1975.

For our preliminary effort, an experimental configuration is being constructed similar to that shown in Fig. XII-1. A sodium oven has been designed and fabricated

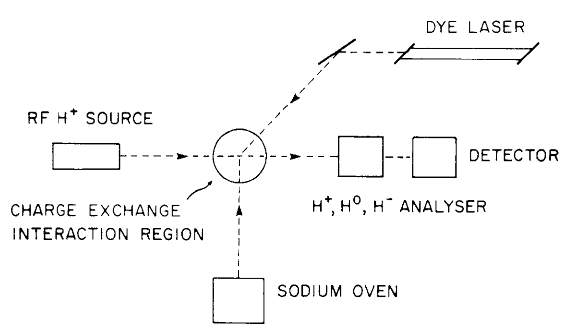

Fig. XII-1. Experimental configuration.

to produce a narrow molecular beam to intersect the H^+ and dye laser beams at right angles. The H^+ source is RF activated and potentially capable of 500 μA output. Its characteristics are now being studied, and use of a dye laser has been arranged. Associated vacuum and other peripheral equipment has been constructed.

B. Plasma Research Related to Fusion

Confinement Systems

1. PHYSICS OF HIGH-TEMPERATURE PLASMAS

U. S. Energy Research and Development Agency (Contract E(11-1)-3070)

Bruno Coppi

An understanding of the physics of high-temperature plasmas is of primary importance in the solution of the problem of controlled thermonuclear fusion. One of the goals in this field of research is the magnetic confinement and heating of plasmas with densities of the order of or larger than 10^{14} particles/cm^3 and thermal energies between 5 keV and 10 keV. The macroscopic transport properties (e. g., particle diffusion, thermal conductivity, and electrical resistivity) of plasmas in these regimes are weakly affected by two-body collisions between particles. These transport coefficients are significantly influenced by the types of collective modes that can be excited in them such as density fluctuations caused by microinstabilities.

In this general area we have carried out a theoretical and experimental program during 1975 and relevant contributions have been presented at national and international conferences. Several papers have been published in professional journals. The primary focus has been on the experimental effort developed around the Alcator machine. Our purpose has been to realize plasmas capable of sustaining very high current densities without becoming macroscopically unstable, in order to achieve the highest possible rate of resistive heating of the plasma itself.

Alcator's unique properties of lack of impurities ($Z \approx 1$), high current density, and large toroidal field, have led to its emergence as the preeminent toroidal confinement device. Specifically, we can point to the following achievements:

(i) Peak plasma densities up to $\sim 6.5 \times 10^{14}/\mathrm{cm}^{-3}$, with energy confinement times of ~20 ms, which yields $n\tau$ values of approximately 10^{13} which exceed those of any existing confinement system by a considerable factor.

(ii) Plasma currents up to 220 kA, corresponding to approximately 1100 A/cm^2 current density.

(iii) Stable discharges sustained for up to 650 ms without feedback control of the vertical (positioning) magnetic field.

(iv) Since the particle density can be varied over two orders of magnitude while obtaining microscopically stable plasma, we have been able to study a sequence of plasma regimes with a varying degree of collisionality and to derive valuable information about the nature of various transport coefficients such as electrical resistivity and energy replacement time. In particular, we have identified a new ("slide-away") regime where strong noncollisional ion heating occurs as a result of current-driven microinstabilities that we have investigated experimentally and theoretically.

(v) The confinement device Rector, which was realized for the purpose of studying noncircular plasma cross sections, has produced stable toroidal equilibria with this feature. Detailed measurements of temperature and density distributions in a noncircular toroidal plasma column have been obtained for the first time by Thomson scattering measurements.

We have also profited from continuing collaborations with scientists from overseas institutions and, in particular, with teams from Jutphaas (Holland), Frascati (Italy) and the Kurchatov Institute (Moscow).

Research – Theoretical

2. RADIO-FREQUENCY HEATING AND HIGH-FREQUENCY MICROTURBULENCE

U.S. Energy Research and Development Administration (Contract E(11-1)-3070)

Abraham Bers

We are now studying two major problems relevant to toroidal plasmas.

a. RF Heating with External Power near the Lower Hybrid Frequency

This research is directed toward exploring the possibilities of supplementary heating of Tokamak plasmas. Theoretical studies are being carried out to determine the extent of the penetration of microwave power into a Tokamak through the density gradient. Further study of the nonlinear processes by which the associated field energy can be imparted to the plasma particles and eventually randomized so that plasma heating actually results is under way. The question is also being raised about what negative effects, if any, might be caused by introducing such fields into a fusion plasma. In particular, possible effects on the plasma transport properties should be studied.

During the past year, we have completed several studies relevant to these problems. We have made a detailed analysis of linear wave penetration from a waveguide array at the wall, including finding the criteria for the array design[1] and for either electrostatic or whistler-Alfvén excitation.[2] We have determined the conditions under which such fields in the plasma can excite electrostatic ion cyclotron waves[1,3] and ion Bernstein waves[4] parametrically. We have also initiated studies of nonlinear stochastic mechanisms that can lead to ion heating,[5,6] and of nonlinear self-modulation effects that may affect the penetration of the fields.[6] We plan to pursue these studies to evaluate toroidal effects that are important in this type of heating. Symbolic computation using MACSYMA has been found extremely valuable for this problem. We also plan to interact with experiments on Alcator and ATC in which this type of heating is being tried.

References

1. A. Bers, in R. C. Cross (Ed.), Proceedings of the U.S.-Australian Workshop on Plasma Waves, University of Sydney, Sydney, Australia, 1975, p. 5.1.

2. A. Bers, C. F. F. Karney, and K. Theilhaber, Progress Report No. 115, Research Laboratory of Electronics, M.I.T., January 1975, pp. 184-204.

3. C. F. F. Karney and A. Bers, Progress Report No. 116, Research Laboratory of Electronics, M.I.T., July 1975, pp. 94-106.

4. D. C. Watson and A. Bers, Progress Report No. 116, Research Laboratory of Electronics, M.I.T., July 1975, pp. 107-116.

5. A. Bers, C. F. F. Karney, and D. C. Watson, Proc. Seventh European Conference on Controlled Fusion and Plasma Physics, Lausanne, Switzerland, September 1-5, 1975, Vol. II, p. 193.

6. C. F. F. Karney, A. Bers, and D. C. Watson, "Linear and Nonlinear Absorption of RF Power near the Lower Hybrid Frequency," Bull. Am. Phys. Soc., Ser. II, 20, 1313 (1975).

b. High-Frequency Instabilities and Microturbulence

At present we are studying instabilities that have their energy source in the tail of the electron velocity distribution function. Such tails are prominent in Tokamaks when the applied field is moderate, i. e., not so high that the distribution function is in the runaway regime but still high enough that the electron density in the tail is an appreciable fraction of the bulk density.[1] There are many reasons why it is important to study such microinstabilities. First, the weak turbulence resulting from such instabilities may be useful in heating the ions. Second, such turbulence may be useful in eliminating trapped-particle effects and their associated deleterious instabilities and transport. Third, the study should lead to a better understanding of the formation and/or inhibition of the electron distribution function tail. Also, in the evolving (early time) stages of any Tokamak, discharge conditions exist under which high-frequency microinstabilities can be excited. This may be of significance in understanding the scaling of plasma characteristics that are reached in the steady (long-time) stage of Tokamak discharges. Heretofore this aspect of Tokamak plasma scaling has been completely ignored. Finally, such microinstabilities can lead to enhanced transport and/or radiation from a plasma that may be significant for a reactor.

During the past year, we have directed this work toward understanding the observed anomalous radiation and ion heating in the Alcator low-density regime. In this regime the effective drift velocity is an appreciable fraction of the electron thermal velocity, and an appreciable high-energy tail has been observed. We have shown that such an anisotropy in the electron distribution function can generate instabilities of the low-frequency electron plasma waves ($\omega_{pe} \cos \theta$) which parametrically downconvert to very short-wavelength lower hybrid waves at ω_{pi}, and propagate across the magnetic field.[2] We have also developed a nonlinear model to describe how the short-wavelength fields at ω_{pi} can heat the ions.[2, 3] Much of this theoretical work is still being refined and strongly coupled to further experimental refinements of the data from Alcator in this regime of its operation. We also plan to pay attention to the recently observed anomalous emission at ω_{pe} and in the electron cyclotron harmonic regime. Such observations have been made on the French Tokamak (TFR) and on Alcator and we plan to interact with these.

References

1. A. Bers, "High-frequency Microturbulence in Tokamak Plasmas," part of an invited talk presented to the Second International Congress on Waves and Instabilities in Plasmas, Institute for Theoretical Physics, University of Innsbruck, Austria, March 17-21, 1975.

2. A. Bers and M. S. Tekula, Proc. Seventh European Conference on Controlled Fusion and Plasma Physics, Lausanne, Switzerland, September 1-5, 1975, Vol. II, p. 194.

3. M. S. Tekula and A. Bers, "Theory of Anomalous RF Radiation and Ion Heating by Microinstabilities in Alcator," Bull. Am. Phys. Soc., Ser. II, 20, 1359 (1975).

3. TRANSPORT COEFFICIENTS AND COLLECTIVE MODES

U. S. Energy Research and Development Administration (Contract E(11-1)-3070)

Bruno Coppi

We expect that the most important transport coefficient in magnetically confined thermonuclear plasmas will be determined by collective modes. In this case the analysis of the nonlinear effects caused by microinstabilities that can be excited in high-temperature regimes becomes of primary consequence. In particular, we need to know whether certain modes arising from the presence of trapped particles produce sufficient scattering of their orbits to inhibit the more violent interchange modes involving the majority of trapped particles that are subject to unfavorable magnetic curvature drifts in a typical Tokamak geometry. We are also concerned with the anomalous slowing down and diffusion of a fast population of injected ions at α particles, and so forth.

The problem of electrical resistivity in high-temperature toroidal systems in the presence of trapped particles has been studied under restrictive and often unrealistic conditions (e. g. , where the Spitzer-Härm approximation is valid). This involves understanding the evolution of the runaway portion of the electron distribution, the effects of current-driven modes, wave-particle resonance processes for the transfer of energy and momentum to the ions, and so forth. Our effort in this area is also directed at providing a basis for an interpretation of the experimental results produced by the Alcator experiment.

An effort is being undertaken to understand the regimes of operation of a toroidal material testing reactor, a high-density deuterium-tritium experiment operating close to ignition conditions. For this purpose numerical transport codes are being developed, including the effects of collisions and collective modes as well as empirical information from the most recent experiments.

Work is being carried out on the transport theory of impurities in thermonuclear plasmas; in particular, on self-decontamination processes[1] that lead to accumulation of impurities toward the outer edge of the plasma column. The results are being correlated with observations made on the Alcator device. The transport of a dense cold plasma accumulated at the edge of a hot-plasma column by appropriate microinstabilities is also being studied, because of the high-density regimes realized in Alcator and Pulsator experiments.

References

1. B. Coppi, "Plasma Modes Due to Impurity and Magnetically Trapped Ions," Phys. Rev. Letters 31, 1443-1446 (1973).

4. NONLINEAR AND TURBULENCE THEORY

U. S. Energy Research and Development Administration (Contract E(11-1)-3070)

Thomas H. Dupree, David A. Ehst

We are studying a variety of problems that arise when strong mode coupling and wave-particle interactions occur simultaneously. The nonlinear theory of trapped-particle modes and drift waves are examples. Other examples are low-frequency equilibrium hydrodynamic fluctuations such as convective modes. We hope to develop a theory that will predict the nonlinear state, including transport properties, fluctuation amplitudes, and spectra.

5. TOKAMAK TRANSPORT THEORY

U. S. Energy Research and Development Administration (Contract E(11-1)-3070)

Dieter J. Sigmar, Steven P. Hirshman, Hark C. Chan, Kenneth Rubenstein

This research is focused on three areas of Tokamak plasma transport theory: Neoclassical transport in multi-ion species plasmas including the alpha particles, MHD equilibrium and collisional transport in Tokamak plasmas at large values of beta poloidal, and interaction of neutral hydrogen with plasma and buildup of Tokamak plasma density by hydrogen gas feed.

The severe effect of small impurity ion concentrations on the energy confinement time and fusion plasma dynamics in general has been widely recognized. The alpha particles, an impurity species themselves, are needed in the plasma to impart their energy but if they accumulate in the center they threaten to choke the fusion process. We have approached the time evolution of these phenomena through impurity transport theory and alpha-particle turbulence.[1,2]

To be economical, fusion reactors have to work at large ratios β_p of particle pressure to poloidal magnetic field pressure. Both experimentally and theoretically, the regime $\beta_p \sim A$ (where A is the toroidal aspect ratio) has been largely unexplored. A paper on this subject will appear soon.[3]

The pioneering $n\tau$-values of Alcator rely on the fact that neutral hydrogen bled in at the wall is converted to plasma without significantly lowering the plasma temperature or destroying the equilibrium. We hope to obtain the scaling laws of this process[4] through a self-consistent theory of the hydrogen and plasma components.

References

1. D. Sigmar and S. P. Hirshman, "Approximate Fokker-Planck Collision Operators for Transport Theory Applications" (submitted to Phys. Fluids).
2. S. P. Hirshman, "Transport Properties of Toroidal Plasmas in a Mixed Collisionality Regime," Phys. Fluids 19, 155-158 (1976).
3. D. Sigmar and J. P. Freidberg, "Tokamak Transport at Large Poloidal Beta, Considering MHD Stability Limits," Fluid Topical Conference on High Beta Plasmas, Culham, England, September 9-12, 1975.
4. J. F. Clarke and D. Sigmar, "Interaction of Neutral Hydrogen and Plasma Including Wall Reflection," Seventh European Conference on Controlled Fusion and Plasma Physics, Lausanne, Switzerland, September 1-5, 1975, Vol. I, p. 134.

6. TEMPORAL BEHAVIOR OF A TOROIDAL PLASMA DISCHARGE

U. S. Energy Research and Development Administration (Contract E(11-1)-3070)

James E. McCune, Paul W. Chrisman, Jay Fisher

Introduction

Our goal is to understand the time development of a toroidal plasma discharge (Tokamak). As a first step, we have investigated the effects of resistivity and viscosity on the dynamics of such a plasma discharge in the "high-collisionality" regime, for which the dissipative MHD equations are applicable. A general invariant form for the viscous force density in this magnetized plasma has been derived from the results of Braginsky[1] in the limit $\omega_c \tau_{ei} \gg 1$, and has been shown to be consistent with the results of other recent studies[2-4] that were carried out under more restrictive assumptions. Anticipating conclusion of our work in this regime, we have also begun work in lower collisionality situations.

Finite-β effects are included throughout. This provides a yardstick whereby we can decide, by comparison with other less general studies, whether and when such phenomena actually affect the results materially. For example, it has become customary to use the "model" field of Pfirsch and Schlüter[5,6] in many calculations, calling on the low-β assumption for justification not to relate the poloidal field, for example, with the plasma current density. As long as caution is exercised, we find that many "steady-state" phenomena can indeed be described adequately by the model field,[3] since the influence of the toroidal geometry is dominant over many finite-β effects in the long-time limits of the various temporal stages of the discharge.

On the other hand, time-dependent phenomena are materially affected by the relationship between the plasma current density and the induced field. This is obviously true in the study of the "field-penetration" phase,[7] during which Faraday induction occurs in conjunction with the setting up of those portions of the magnetic field associated with the currents driven in the plasma. A less obvious fact is that the well-known poloidal spin-up instability[8,9] is vitally affected by finite-β because the nature of this instability can be greatly changed, depending on whether or not $\partial \underline{B}/\partial t = 0$.

We believe that study of the time-dependent problem will emerge gradually as a key to understanding "steady-state" and quasi-steady operation of both present toroidal plasma experiments and eventual fusion devices. It appears essential to recognize the different time scales over which various important phenomena occur in order to establish the actual regime(s) in which a given experiment will operate. This belief is accentuated by the fact that actually many experiments do not have a sufficiently long operating time to achieve a steady state; interpretation of the results can be vitally changed, once this is recognized.

Equally interesting is the recognition of the possibility that it may turn out to be <u>desirable</u> to operate a fusion device on a pulsed, quasi-steady basis. For example, we may wish to scale such a machine so that a sufficient confinement period for net fusion power production can be achieved over an operating time that is still too short for certain deleterious "long-time" effects to set in. The exploration of this possibility provides further motivation for the present research.

Time-Scale Formalism

In the initial part of our work[10-13] we studied the dissipative MHD equation and obtained a general form for the viscous stresses. The use of a multiple-time-scale formalism was introduced and shown to be advantageous in setting forth in an understandable fashion the sequence of events occurring in a toroidal plasma discharge. It then became possible to study the conditions under which the plasma spin-up in a torus can be stabilized by viscosity or other effects.[11-14] This question is treated under the assumption that $\dot{\underset{\sim}{B}} = 0$ or, in other words, that complete field penetration has already occurred prior to spin-up.[8,9] It has been shown in complete generality for that case that the spin-up is always stabilized at a poloidal speed such that the "geodesic speed," i.e., the poloidal speed projected onto the field lines at the same radius, remains subsonic for any finite viscosity. Thus there is no need to speculate on the existence of a shock wave[8] as the mechanism required to provide such stabilization.

Two useful features of the time-dependent theory deserve special mention. First, we find that the energy-transport problem, which we have not yet treated, can be discussed virtually independently of the dynamical problem. This provides a fresh framework within which many crucial energy-transport questions can be posed.[14] Second, since many machines operate "initially" (over a short time scale) in the high collisionality (MHD) regime and only then pass into lower collisionality regimes, the multiple-time-scale concept is useful even in deciding which physical description of the plasma is relevant. For example, we can readily visualize a situation in which the MHD description is relevant at the start (over the "fast" time period, including the field-penetration phenomenon), whereas the more complex description of kinetic theory is required in later phases of the discharge. If such a picture is applicable, the present theory of the short-time behavior of the plasma will be useful even for devices designed to operate (eventually) in the low-collisionality situation. In this case the field penetration (and spin-up) may well be described by the classical resistive MHD picture, whereas the long-time plasma mass diffusion (particle loss) may require a kinetic description.

With regard to time scales, provided MHD waves and instabilities are "unresolved" or averaged out, the field penetration time τ_1 is measured by

$$\tau_1 = \frac{\mu_o r_o^2}{\eta}, \tag{1}$$

where r_o is the plasma minor radius, and η the resistivity. This time is the same as

$$\tau_1 = \tau_{ei}\left(\frac{r_o}{c/\omega_{pe}}\right)^2 \tag{2}$$

with τ_{ei} = electron-ion collision time, and c/ω_{pe} = the classical skin depth of the resistive plasma. For densities and machine sizes of fusion interest, τ_1 is many times τ_{ei}. From (2) and the formulas of Spitzer[15] it is trivial to work out numerical values for τ_1. For an MHD discharge the next slower time scale, τ_2, is longer by the inverse square of the aspect ratio,[12, 13] i.e., by a factor $\epsilon^{-2} = R^2/r_o^2$.

Recent Results and Projected Work

The spin-up instability in a viscous, toroidal, MHD plasma has been treated by Chrisman[14] for the case $\dot{\underline{B}} \neq 0$. The results provide an important example of "finite-β" effects; that is, self-consistent induced fields can change the spin-up stability criteria qualitatively (compare these results with those of Hazeltine et al.[8, 9]). Chrisman has also discussed possible energy-transport phenomena in the light of the new theory with the hope of gaining new insight into this crucial problem.

As we have pointed out, over time τ_1 a toroidal plasma discharge may evolve from an initial "MHD plasma" to a "low-collisionality" plasma in which trapping phenomena become significant. In order to treat this problem in a general way, we are investigating relevant time scales that are appropriate to low-collisionality regimes. An obvious time scale is the "bounce-time" $\sim r_o/\langle v_{11} \rangle$. We expect that there will be others, which we shall sort out by a multiple-time-scale formalism.

Direct treatment of the time-dependent problem at low collisionalities makes use of the drift-kinetic equation for the guiding-center distribution. Our approach to solution, in addition to the use of multiple-time-scale methods, is to model this distribution in terms of a finite set of its velocity-space moments, monitor these moments in time with the help of the standard set of moment equations, and "close" this set with appropriate use of the collision operator. The latter procedure is in effect a generalization of the neo-classical transport studies, with due emphasis on flux-averaged quantities and their (averaged) time dependence.

A portion of this work was carried out in collaboration with the late Dr. Karl U. von Hagenow (d. November 20, 1975), at the Max-Planck-Institut für Plasmaphysik, under the terms of the agreement between the Institute and EURATON. Two of us (J. E. McCune and P. W. Chrisman) wish to express their deep gratitude for the opportunity of collaborating with Dr. von Hagenow and their profound sorrow at his passing from us.

References

1. S. I. Braginsky, Reviews of Plasma Physics, Vol. I, p. 205 (Consultants Bureau, New York, 1968).
2. R. C. Grimm and J. L. Johnson, Plasma Phys. 14, 617 (1972).
3. M. A. Hellberg, N. K. Winsor, and J. L. Johnson, Phys. Fluids 17, 1258 (1974).
4. H. Okuda, Phys. Fluids 17, 375 (1974).
5. D. Pfirsch and A. Schlüter, MPI/PA/7/62, Max-Planck-Institut für Physik und Astrophysik, Munich, 1962.
6. G. Knorr, Phys. Fluids 8, 1334 (1965).
7. H. Grad and J. Hogan, Phys. Rev. Letters 24, 1337 (1970).
8. R. D. Hazeltine, E. P. Lee, and M. N. Rosenbluth, Phys. Fluids 14, 361 (1970).
9. R. D. Hazeltine, E. P. Lee, and M. N. Rosenbluth, Phys. Rev. Letters 25, 427 (1970).
10. P. W. Chrisman and J. E. McCune, Annual Meeting on Theoretical Aspects of Controlled Thermonuclear Research, Arlington, Virginia, April 7-9, 1975.
11. P. W. Chrisman, K. U. von Hagenow, and J. E. McCune, IPP 6/138, Max-Planck-Institut für Plasmaphysik, Munich, August 1975.
12. P. W. Chrisman, K. U. von Hagenow, and J. E. McCune, "Self-Consistent Time Dependent MHD Toroidal Flow with Finite Resistivity and Viscosity" (submitted to Nucl. Fusion).
13. P. W. Chrisman, K. U. von Hagenow, and J. E. McCune, Seventeenth Annual Plasma Physics, American Physical Society Meeting, St. Petersburg, Florida, November 10-14, 1975.
14. P. W. Chrisman, "Inertial Viscous and Finite Data Effects in a Resistive Time-Dependent Tokamak Discharge" (Doctoral thesis research to be submitted to Department of Nuclear Engineering, M. I. T.).
15. L. Spitzer, Jr., Physics of Fully Ionized Gases (Interscience Publishers, New York, 1962).

Research – Experimental

7. TOKAMAK RESEARCH

U. S. Energy Research and Development Administration (Contract E(11-1)-3070)

George Bekefi, Lawrence M. Lidsky, Peter A. Politzer, Louis D. Smullin

We propose to carry out a wide-range program on hot toroidal discharges using Tokamaks of research size specifically designed for easy accessibility with a variety of diagnostic apparatus.

Our operating facility, at present, is Versator I, a toroidal device with major radius 54 cm, and minor radius 14 cm. The maximum toroidal magnetic field is 5 kG; the ohmic current driven by an air core transformer does not exceed 12 kA. The electron density N lies in the range 10^{12} cm^{-3}-3×10^{13} cm^{-3}, the electron temperature $T_e \leq$ 100 eV, and the ion temperature $T_i \lessapprox 50$ eV.

Versator I is being upgraded to increase the capacitor bank that energizes the toroidal field from 40 kJ to 200 kJ. This will raise the toroidal magnetic field from ~5 kG to a little over 10 kG. It is hoped that T_e will be raised to ~300 eV thereby, and hence allow operation in the "collisionless" electron regime.

The usefulness of Versator I is limited by two constraints. First, it has few large diagnostic windows, and the overall accessibility leaves much to be desired. Second, the base pressure is of order 5×10^{-7} Torr. For certain impurity and vacuum studies, base pressures of $\sim 1 \times 10^{-8}$ Torr are mandatory. For these reasons, we are planning partly to build and partly to purchase a new facility, Versator II. Versator II would be similar in design to "Erasmus" but would have much better vacuum capability and diagnostic portholes that are better engineered. We expect to place the order for this new system and have it fully operational within a year.

Our research will encompass the following subjects.

(a) Parameter Studies of Tokamak Plasmas

There is evidence from studies on Alcator that after suitable preparation and thorough discharge cleaning, the toroidal discharge can be run over a wide range of densities ($10^{12} \lesssim N \lesssim 10^{14}$ cm^{-3}) and possibly of electron temperatures. We plan to map out the entire range carefully, making detailed measurements of electron and ion temperatures, densities, and density gradients. The greater part of this work will be done with Thomson-scattering methods, microwave interferometry, and by measurement of charge-exchange neutrals.

Versator II will be designed specifically to allow us to measure, by Thomson scattering, the electron temperature parallel to the toroidal field. Hitherto, only $T_\perp$ has been measured in Tokamak research.

(b) Development of Novel Diagnostics

We propose to concentrate on the development of new techniques for simultaneous determination of <u>time</u> and <u>space</u> spectra of various fluctuating plasma parameters.

Thus, for example, when an instability is observed the aim will be to determine the ω-k dispersion characteristics. If the turbulence is broadband, we would wish to measure simultaneously the time and space correlation functions. This requires development of on-line data acquisition and processing, and novel (say TV-like) displays. Spatial Fourier analysis and spatial filtering techniques are being considered.

Specifically, we shall begin by using as our probe the fluctuations of the light intensity emanating from the plasma. We shall make two-point crosscorrelation and autocorrelation measurements in time and space. An alternative scheme that is under consideration is to use laser excitation of specific atomic transitions and then to study the line intensity and linewidth of the excited transitions. This can yield the plasma density and temperature spatially resolved along the laser beam.

(c) Electromagnetic Millimeter-Wave Diagnostics

We propose to study more elaborate probing techniques than conventional millimeter-wave interferometry for measuring average density, in an effort to learn more about the structure of the discharge. In Tokamaks the large plasma current produces a poloidal field that twists the dc field lines. Thus an incident RF wave will have its polarization twisted as it passes through the plasma. We hope to be able to determine something about the current distribution in the cross section by measuring the complex values of the emerging parallel and perpendicular fields, using independent measurements of total plasma current and of density distribution (from scattering). The theory is now being developed and will be verified on Versator.

Another approach toward measuring plasma structure is the use of probing signals sent along the column and detected at a number of points away from the source. The intent here is to discover whether the subsurface exploration techniques used on the Moon and in some geophysical studies can be applied to plasmas that not only are inhomogeneous but also anisotropic. Professor J. A. Kong has been a major contributor to the theory of such geophysical explorations and he proposes to study the extension of these ideas to plasmas.

(d) Quantitative UV Spectroscopy (50 Å-1000 Å)

Quantitative spectroscopy of highly ionized atoms is a relatively new field, and has not yet been well explored. Absolute measurements of line radiation, for example, can serve as a powerful diagnostic of plasma impurities. For this, radiative transition probabilities, oscillator strengths, level excitation, cross sections, and so forth, must be known. They can be measured only in hot discharges of known properties. In this work we are seeking cooperation with a team of scientists from Johns Hopkins University who are now actively engaged in UV spectroscopy.

(e) Vacuum Technology

The discharge-cleaning procedure for Alcator has resulted in a breakthrough concerning plasma purity of these hot discharges, although the reason why this particular technique gives such a uniquely low impurity level is still not understood. We propose to measure absolute impurity levels spectroscopically, in conjunction with careful studies of the surface physics when materials are in contact with hot electrons and ions of the Tokamak plasma. Specifically, we shall measure the time development of impurities during discharge cleaning. The variable parameters will be the fill pressure of the gas, the partial pressures of the different gases, if mixtures are tried, and the power of the RF oscillator generating the discharge plasma. There is preliminary evidence that the species of impurity (oxygen, carbon) depends on the strength of the discharge.

The use of pulsed gas feed has been an important element in our ability to push Alcator to high-density operation. But we have only had available pulsed valve feeding at a single location. Nothing is known about the effects of filling and spreading time or of asymmetries. Would two or four equally spaced valves be better than one? Would a programmed gas fill have any advantages over a simple gas burst? We intend to study this problem on Versator.

(f) Fluctuations and Instabilities

As we sweep through the available range of plasma densities and temperatures of Tokamak discharges, different fine-grained instabilities are expected. Among these, the two most interesting are an ion-acoustic instability when the electron drift becomes comparable with the electron thermal velocity, and trapped-particle instability when the temperature becomes sufficiently high to make the electrons "collisionless" (i.e., the mean-free path becomes greater than the bounce length). Neither instability has been positively identified; the last-named has probably never been seen in toroidal geometry. We shall study these fluctuations in time and space.

(g) Cyclotron Radiation

There is evidence from other Tokamaks that anomalously large emission occurs at the electron cyclotron frequency and its harmonics. We are instrumenting a microwave detector designed to study the electron cyclotron emission from Versator I.

8. NEUTRAL-BEAM RESEARCH

U. S. Energy Research and Development Administration (Contract E(11-1)-3070)

Louis D. Smullin

We are studying the problem of designing more efficient plasma sources for positive ion extraction. The study of injected electron-beam systems with high order σ-cusp insulation of the lateral walls is proceeding well, and we expect to demonstrate full-sized units during this year. We do not plan to exploit them technically; we would prefer to study in greater detail the mechanisms of the low-pressure, hot-cathode discharge whose details are still largely unknown and hardly more understood than Langmuir's initial ideas of the 1920s. We also plan to study some of the details of plasma leakage through a high-order σ-cusp system.

We are also addressing the problem of producing intense negative ion beams by double charge exchange in a Cs vapor cell. We have begun to study enhanced charge exchange in optically excited alkali vapors (under National Science Foundation support) and are building the first-generation apparatus for these studies. It is not yet clear that this would be a technically practical system even if the physics works out as we hope. We plan, however, to broaden and expand our studies in order to arrive at practical, efficient configurations of vapor cells that are compatible with the requirements of high-current, large cross-section, well-focused beams.

9. NEUTRAL-BEAM SOURCES FOR PLASMA HEATING

U. S. Energy Research and Development Administration (Contract E(11-1)-3070)

Louis D. Smullin, Leslie Bromberg, Peter T. Kenyon

We are studying the behavior of plasma discharges from which high-current positive ion (H^+ or D^+) beams are extracted at currents of 10-50 A. Our goal is to achieve a significantly lower power consumption than that of existing devices (Berkeley Multifilament Arc, duo-PIGatron, etc.) which require approximately (1-5 kW)/A (discharge power)/(extracted ion current). We reduce plasma losses to the walls by providing a high-order cusp field around the plasma chamber with permanent magnets. The fringing field of the solenoid at the cathode reduces loss to the back walls. We find that the efficiency of the discharge depends on the details of the cathode geometry and have compared several different configurations. Present experimental results with arc powers <2 kW indicate that we should be able to construct a 10 A, 40 cm^2 device consuming no more than 4-5 kW. The performance of these devices depends in an important way on the details of the cathode geometry. We are testing a family of different cylindrical cathodes to determine the best L/D ratio and to understand the scaling laws. We shall undertake the design of a 100 cm^2, 50 A system later this year.

We have developed a model capable of predicting quantitatively the performance of the Berkeley Multifilament Arc (see Part II, Sec. XII-B. 8). We propose to continue these studies in the more complex geometry of our magnetically confined plasma sources.

10. COHERENT SCATTERING EXPERIMENT: SCATTERING OF 10.6 μm RADIATION

U. S. Energy Research and Development Administration (Contract E(11-1)-3070)

Lawrence M. Lidsky

We have completed the first stages of an experimental investigation of coherent scattering from a well-diagnosed steady-state laboratory plasma. The experiment is based on the use of an extremely stable 10.6 μm CO_2 laser oscillator-amplifier system and a completely liquid nitrogen-cooled viewing system utilizing an electrically scanned Fabry-Perot interferometer and a liquid helium-cooled interference filter. We have successfully measured the plasma frequency wing of the scattered spectrum and compared it with theoretical predictions based on other measurements. We are attempting to measure the low-frequency "ion" feature of the spectrum, but we have encountered difficulties because the necessity of operating the interferometer near liquid nitrogen temperature puts very severe requirements on it. We have extended the theory of the low-frequency wing to include the effect of moderately strong collisions.

Fusion Technology Studies

Our research into various technological problems associated with the design, construction, and operation of controlled thermonuclear reactors continues. Our goals are to evaluate the engineering requirements for fusion reactors, assess the possible applications of this power source, and produce the engineering data required for the design of a reactor. As well as this work in progress, we have completed an experimental study simulating the cyclic stresses that are expected in the first wall of a theta-pinch reactor.

11. FISSION-FUSION SYMBIOSIS

U. S. Energy Research and Development Administration (Contract E(11-1)-3070)

Lawrence M. Lidsky, Donald L. Cook, Mark Gottlieb, Kenneth J. Laskey

Because of various high-energy neutron multiplying reactions, fusion reactors operating on the D-T cycle will be copious sources of excess neutrons. We are investigating the possibility of using these neutrons for the production of fissile U^{233} in a thorium containing blanket and assessing the relative merits of various schemes with respect to engineering and economic constraints. We have developed the requisite neutronic codes, performed a simplified analysis of the value of fusion-produced fuel in a fission fuel in a fission reactor economy, and have analyzed several reference engineering designs. We have found that reprocessing costs will play a dominant role in the economics of fissile reactors. At the present stage in our studies, the most economical design appears to be based on a highly thermalized molten salt system.

12. HIGH-INTENSITY NEUTRON SOURCE

U. S. Energy Research and Development Administration (Contract E(11-1)-3070)

Lawrence M. Lidsky, Alan R. Forbes

The gas target source is a prime candidate for the intense 14 MeV neutron facility that must be developed for testing fusion reactor material. We are planning to perform experimental measurements of the detailed behavior of a beam-heated jet in a quarter-scale intermittently pulsed model of such a device. Our goal is to compare theoretical predictions and extensive numerical computations with experimental results. In this effort we expect to be working in close collaboration with the Los Alamos Scientific Laboratory. All major components of our system have been procured or constructed and preliminary assembly is now taking place.

13. EBT-RX

U. S. Energy Research and Development Administration (Contract E(11-1)-3070)

Lawrence M. Lidsky, David A. Ehst, Aniket Pant, David L. Kaplan

In close collaboration with the Oak Ridge National Laboratory we have begun a study of the fusion-reactor potential of the EBT concept.

The primary goal of the EBT-RX study is development by October 15, 1976 of two conceptually realizable, first-order optimized EBT reactor models and a list of the critical assumptions and approximations implicit in these models. One of the conceptual designs will be completely microwave-driven; with the other design we shall explore the possibilities inherent in beam-augmented systems. The reference designs will help delineate the appropriate scale sizes, operating regimes, and support system requirements, and will demonstrate the sensitivity of scale and operating characteristics to changes in system or plasma parameters. The ultimate aims of this study are to focus the attention of the experimental-theoretical group on the physics of the most plausible operating regimes, define support system (microwave, neutral-beam, instrumentation and control) technology goals, and encourage action as early as possible on particularly critical design problems such as magnet shielding. The Oak Ridge National Laboratory-Massachusetts Institute of Technology interaction will be structured to take advantage of the existing strengths of both organizations. In particular, the wide range of technological expertise available within the M. I. T. community will be combined with the experimental and theoretical understanding of the EBT concept at ORNL. This joint study will also serve to augment these strengths. It will acquaint a wider range of faculty and research staff at M. I. T. with problems of controlled thermonuclear research interest, set up an organizational model for implementing future "moderate scale" technology studies (e. g., high-field Tokamaks), and furnish an excellent medium for motivating and educating students.

14. PELLET FUELING OF FUSION REACTORS

U. S. Energy Research and Development Administration (Contract E(11-1)-3070)

Peter A. Politzer, Mark L. McKinstry, Warren K. Brewer,

Clarence E. Thomas

There are several serious questions associated with the operation of a quasi steady-state fusion reactor. Among these is the problem of introducing cold deuterium and tritium fuel material into the core of the reacting plasma. We are exploring the feasibility of injecting small solid D-T pellets at high velocity. The ablation rate of the pellet surface, and hence the distribution of fuel in the plasma, is determined by a complex interaction between the energy input from the hot dilute plasma and the outward flow of cold dense fuel. The dominant effect is the shielding of the pellet surface by the surrounding cold-plasma cloud that excludes the magnetic field from the region around the pellet. We are pursuing a theoretical analysis of this shielding phenomenon in order to make an estimate of the ablation rate and the pellet lifetime. We are also undertaking an experimental test that will simulate for short times the energy flux that would be encountered by a pellet in a thermonuclear reactor.

C. Other Plasma Research

1. PLASMA TURBULENCE IN THE VICINITY OF A MAGNETIC NEUTRAL LINE

Research Laboratory of Electronics, M. I. T. Industrial Fellowship

Peter A. Politzer, David O. Overskei

The behavior of a collisionless plasma in the vicinity of a magnetic neutral line has been investigated. The geometry is of interest for certain types of laboratory plasma-containment devices such as Tokamaks with limiters, and for astrophysical processes such as solar flares and the neutral sheet in the geomagnetic tail. An electric field applied along the neutral line results in a redistribution of plasma density that is consistent with $\underline{E} \times \underline{B}$ flows. The development of a complex spectrum of low-frequency waves, $\omega_{ci} < \omega < \omega_{pi}$, is observed. These waves are spatially localized to the vicinity of the neutral line and propagate antiparallel to the applied electric field. As the electric field is increased the wave spectrum changes from a complex mode structure to a broad turbulence spectrum. Heating of both bulk and tail of the electron energy distribution is observed. Typical measured values of density, electron temperature, and electric field indicate an anomalously large resistivity. Preliminary theoretical stability analyses indicate that the observed instability is a variant of the current-driven ion-acoustic mode, which gives rise to significant heating of the electron distribution. Such a process may play an important role in the generation of energetic particles in solar flares and in the geomagnetic neutral sheet. For the first time, an equilibrium model has been developed for this configuration and it is being used in a more detailed stability analysis.

PLASMA DYNAMICS

A. Basic Plasma Research

1. TIME-SPACE EVOLUTION OF THE THREE-WAVE INTERACTION IN A HOMOGENEOUS PLASMA

National Science Foundation (Grant ENG75-06242)

Abraham Bers, Allan H. Reiman, David J. Kaup

In this report and in Sections XII-A. 2 and XII-A. 3 we describe the complete time-space evolution of the lowest order nonlinear conservative coupling of three undamped waves in a medium. The homogeneous interaction has been described[1] by

$$\left(\frac{\partial}{\partial t} + v_1 \frac{\partial}{\partial x}\right) a_1 = p_1 K a_2 a_3 \tag{1a}$$

$$\left(\frac{\partial}{\partial t} + v_2 \frac{\partial}{\partial x}\right) a_2 = -p_2 K^* a_1 a_3^* \tag{1b}$$

$$\left(\frac{\partial}{\partial t} + v_3 \frac{\partial}{\partial x}\right) a_3 = -p_3 K^* a_1 a_2^*. \tag{1c}$$

Here the $a_i(x,t)$ are (complex) wave packet amplitudes, the v_i are group velocities, the $p_i = \pm 1$ are signs of the wave energies, and K is the (complex) coupling coefficient. Our results are based upon a numerical simulation of various interactions[2,3] and upon a formulation of the solution of Eqs. 1 in the inverse scattering framework.[4] These approaches complement each other, and have allowed us to extract and analyze the important characteristics of the explosive, decay, and backscattering interactions that we shall now summarize.[5] A more complete description of both simulation and analytic work will appear in another publication.[6] Backscattering will be discussed in detail in Section XII-A. 2 and the effects of inhomogeneities in Section XII-A. 3.

<u>Explosive Interactions</u> ($p_1 = -1 = -p_2 = -p_3$ or $p_1 = 1 = -p_2 = -p_3$)

It is well known that when the spatial variation in the envelopes $a_i(x,t) = a_i(t)$ is ignored the solution to Eqs. 1 always becomes unbounded in a finite time.[7] That this need not be so for finite-extent envelopes has also been recognized.[8] Figure XII-2 shows the results of our numerical solution of Eqs. 1 for this case with the initial amplitudes of a_2 and a_3 chosen small compared with a_1. The interaction is only found to be explosive, as shown in Fig. XII-2c, if initially a_2 and a_3 can evolve into growing normal modes, as shown in Fig. XII-2b. This condition can be established from Eqs. 1b and 1c by assuming that since a_1 is large it does not change much during the initial buildup of a_2 and a_3. A WKB analysis then shows that the buildup of normal modes requires $(v_2-v_1)(v_1-v_3) \geqslant 0$ and

$$M_1 \equiv \int_{-\infty}^{\infty} \frac{|Ka_1(x,t=0)|}{|(v_2-v_1)(v_3-v_1)|^{1/2}} dx \geq \frac{\pi}{2}. \tag{2}$$

In arriving at Eq. 2 we assumed that $|a_1|$ goes to zero only at the pulse edges and that arg (a_1) is independent of x. If this is not so, the WKB analysis can still be carried out but the condition for growing normal modes is more complicated.

If the inequality in Eq. 2 is satisfied, the interaction will evolve "explosively" in the sense that all wave packets grow in a finite time to produce a singularity, as shown by the large spatially narrow spike in Fig. XII-2c. On the other hand, if $M_1 < \pi/2$ there is essentially no interaction in the time during which the wave packets separate and move apart.

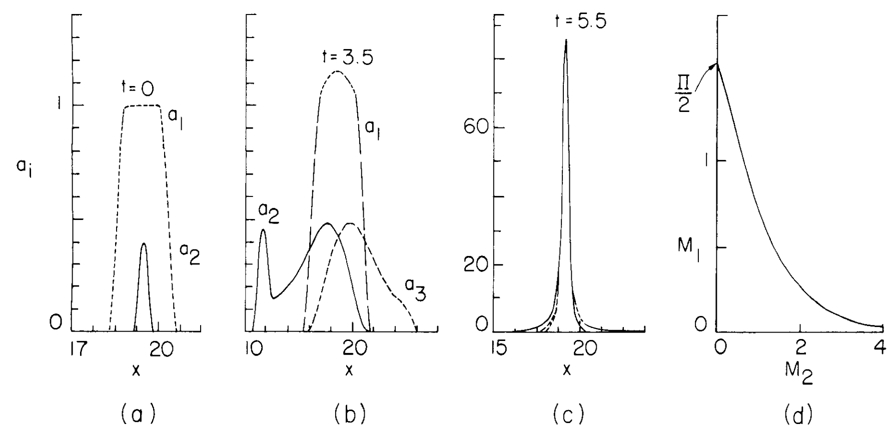

Fig. XII-2. Interaction of three waves with $p_1 = -1$, $p_2 = p_3 = 1$. (a)-(c) Time development for initial configuration with $a_3(x,t=0) \equiv 0$, $M_1 = 2.4 > \pi/2$, $M_2 = .14$. Times are normalized to $1 = |K(a_1 = 1)|$. Other units arbitrary. Note change of scale in (c). (d) Threshold condition for nonoverlapping colliding pulses 1 and 2 with $a_3(x,t=0) \equiv 0$. Parameters above the curve give explosive instability.

In the inverse scattering formalism for solving Eqs. 1, Eq. 2 corresponds to the WKB condition that the initial a_1 envelope contain at least one soliton. This follows by recognizing that the integrand of M_1 is the scattering potential of the associated Zakharov-Shabat (Z-S) eigenvalue problem.[4,9] In this formalism the explosive instability is identified by the fact that when the middle group velocity envelope has a soliton and the envelopes do not separate, the solution of the scattering problem becomes singular. The condition for infinitesimal stability is that the middle group velocity envelope contain no solitons (bound states). In the WKB approximation this gives $M_1 < \pi/2$; a sufficient condition, even if the WKB analysis is not valid, is $M_1 < 0.903$. From the inverse scattering formalism we also find a stability condition for finite perturbations,

$$\left(\tan^2 M_1\right)\left(\sinh^2 M_2\right) \leqslant 1, \tag{3}$$

which is plotted in Fig. XII-2d. Even if $M_1 < \pi/2$ an explosive instability may ensue if M_2 is sufficiently large. M_2 is defined analogously to M_1 of Eq. 2 with $a_1 \rightarrow a_2$, $v_1 \rightarrow v_2$, $v_2 \rightarrow v_3$, and $v_3 \rightarrow v_1$.

Decay Interactions with Solitons ($p_1 = p_2 = p_3 = +1$)

Again we consider the case wherein the highest frequency wave packet $a_1(x,t)$ has the middle group velocity $(v_2-v_1)(v_1-v_3) > 0$. In a case of prime interest this wave packet is initially of an amplitude $|a_1(x,t)|$ much larger than both $|a_2(x,t=0)|$ and $|a_3(x,t=0)|$. Figure XII-3a gives the results of computations on the evolution of the nonlinear interaction from such initial conditions. We note that the buildup of wave packets 2 and 3 causes the pump wave packet 1 to deplete as expected, but when 2 and 3 leave as a pair of oppositely directed pulses, wave packet 1 is not fully depleted (Fig. XII-3b) and 2 and 3 begin to grow again and are emitted as two more pulses (Fig. XII-3c). As shown in Fig. XII-3c, the pump is then sufficiently depleted and no longer able to generate any more of pulses 2 and 3. The generation of pulses 2 and 3 is clearly tied to the ability of 1 to build up 2 and 3 from small amplitudes, i.e., to the initial normal mode buildup

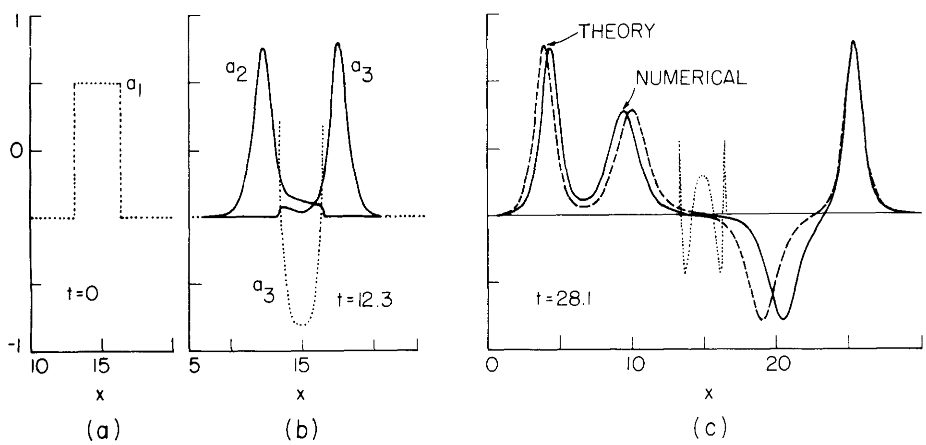

Fig. XII-3. Time development of a decay interaction with rectangular pulses initially. $M_1 = 6.4$, $M_2 = .003$, $M_3 = 0$. $a_1(t=0)$ is too small to be visible in (a). Units arbitrary, except for t, which is normalized to $|K(a_1 = 1)| = 1$. In (c) the prediction of the two-soliton formula for the asymptotic profiles of a_1 and a_3 is included.

when 1 is essentially constant. The WKB criterion for having N normal modes in the pump wave packet 1 is just

$$\left(N-\frac{1}{2}\right)\pi \leq M_1 < \left(N+\frac{1}{2}\right)\pi, \tag{4}$$

and this leads to the generation of N pairs of pulses (a_2, a_3).

In the inverse scattering formalism the initial and final conditions of this problem correspond to approximately separated envelopes for which the scattering problem reduces to the well-known Zakharov-Shabat (Z-S) problem. From the relations between initial and final scattering data we can show that for $p_1 = p_2 = p_3 = +1$ and $(v_2-v_1)(v_1-v_3) > 0$ the interaction is such that a_1 will give up its solitons to a_2 and a_3. Thus the final envelopes of wave packets 2 and 3 are determined by an N soliton formula. The number of solitons N is determined by the number of bound states in the Z-S scattering potential appropriate to a_1, which is just the integrand of Eq. 2. Thus N is determined by the same equation that determines the number of normal modes (a_2, a_3) that can build up within the pump a_1, i.e., Eq. 4.

The parameters of the N soliton formula are completely determined by the spatial profile and growth rate of the eigenmodes. Our numerical solutions show that the emitted pulses are always well separated. Thus each pulse of a_3 is approximately described by $2\eta_i\sqrt{(v_1-v_3)(v_2-v_3)}\ \mathrm{sech}\,(2\eta_i(x+v_3t-x_o))$. The inverse scattering eigenvalue η_i is defined by $\eta_i = p_i/2(v_3-v_1)$, where p_i is the growth rate of the i^{th} normal mode. Thus when the initial profile of a_1 is a rectangle of height $a_1(t=0)$, the heights of the emitted pulses will be bounded by $\left|(v_3-v_2)^{1/2}\, a_1(t=0)/(v_3-v_1)^{1/2}\right|$ and will approach that limit as M_1 becomes large. When the initial profile of a_1 is not rectangular, a more general bound on the heights is provided by the WKB condition on p, $\int_{-\infty}^{\infty}\left(\left|Ka_1(x,t=0)\right|^2-p^2\right)^{1/2} dx = 0$.

When the profile of a_1 is initially rectangular we can write closed-form time asymptotic solutions for a_2 and a_3 by solving the associated scattering problem at t = 0 and then applying the relations between initial and final scattering data. Let $a_1(x, t=0)$ be a rectangle of width L and height $|a_1(t=0)|$ with its left edge at x = 0. Let $a_2(x, t=0)$ be a small pulse centered at $x = \ell_o$, $0 \leq \ell_o \leq L$. Assume that a_3 is zero at t = 0. Then

$$a_3 = \sum_{j,k} D_j \exp(-(\eta_j+\eta_k)x)\left(1+\overleftrightarrow{N}^2\right)^{-1}_{jk} \tag{5}$$

with the sum taken over the growing eigenmodes of the linearized equations (bound states of the associated scattering problem), where

$$N_{ij} = D_j \frac{\exp(-(\eta_j+\eta_i)x)}{\eta_j+\eta_i} \tag{6}$$

$$D_j = (-1)^{j+1} \frac{A_j \hat{a}_2(\eta_j, t=0)}{2L(1+\eta_j L)} \sin(\eta_j \ell_o) \exp(\eta_j(L+v_3 t)) \tag{7}$$

$$A_j = \left(Q_1^2 L^2 - \eta_j^2\right)^{1/2}, \tag{8}$$

and $\hat{a}_2$ is the Fourier transform of the initial profile of a_2. There is a similar formula for a_2.

Collision of Wave Packets Containing Solitons ($p_1 = p_2 = p_3 = 1$)

Next, we consider collisions of pulses of a_2 and a_3 with the same p_i and the same velocity ordering that we have just considered. Figure XII-4 shows numerical solutions of such interactions. The interaction is weak at large velocities (or small initial amplitudes) as shown in Fig. XII-4b. Some energy is transferred to a_1, but not enough to cause significant depletion of a_2 and a_3. The profile of a_1 in Fig. XII-4b could be determined to a good approximation by assuming that a_2 and a_3 are undepleted. The solution is then a convolution of $a_2(t=0)$ and $a_3(t=0)$. At lower velocities (or larger initial amplitudes) the interaction is stronger, and may lead to almost total depletion of a_2 and a_3, as shown in Fig. XII-4c. The time development is now truly nonlinear and leads to the formation of a sharp spike in a_1. The determination of the subsequent behavior of a_1 is just the same problem that we considered in discussing decay interactions with solitons. In particular, note that the interaction leading to Fig. XII-4c has deposited a soliton in a_1. This will result in the subsequent appearance of solitons in a_2 and a_3. The normal mode buildup is already apparent in Fig. XII-4c.

An inverse scattering analysis allows us to determine roughly the heights and widths

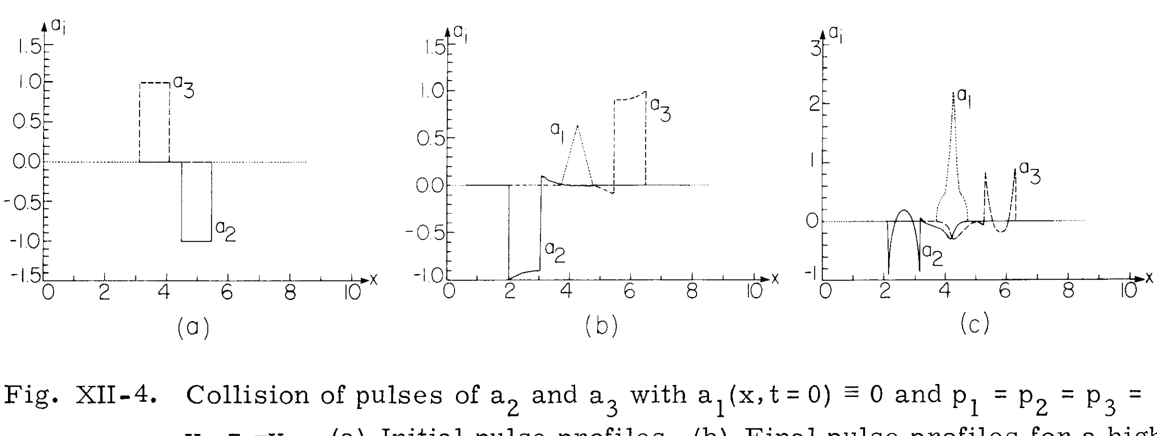

Fig. XII-4. Collision of pulses of a_2 and a_3 with $a_1(x, t=0) \equiv 0$ and $p_1 = p_2 = p_3 = 1$. $v_3 = -v_2$. (a) Initial pulse profiles. (b) Final pulse profiles for a high-velocity collision: $M_2 = M_3 = .34$ at $t = 0$. (c) Pulse profiles after collision with lower velocities: $M_2 = M_3 = 2.0$ initially.

of the pulses after collision. The procedure for doing so will be discussed elsewhere.[6]

Equivalent Two-Dimensional Steady-State Interactions

There is a class of two-dimensional steady-state equations whose solution reduces to that of Eqs. 1. The two-dimensional time-independent generalization of (1) is

$$\left(v_{1x}\frac{\partial}{\partial x}+v_{1y}\frac{\partial}{\partial y}\right)a_1 = p_1Ka_2a_3$$

$$\left(v_{2x}\frac{\partial}{\partial x}+v_{2y}\frac{\partial}{\partial y}\right)a_2 = -p_2K^*a_1a_3^*$$

$$\left(v_{3x}\frac{\partial}{\partial x}+v_{3y}\frac{\partial}{\partial y}\right)a_3 = -p_3K^*a_1a_2^*.$$

If v_{1x}, v_{2x}, and v_{3x} are all positive, then if we let $a_1 = \sqrt{v_{2x}v_{3x}}\ b_1$, $a_2 = \sqrt{v_{1x}v_{3x}}\ b_2$, $a_3 = \sqrt{v_{1x}v_{2x}}\ b_3$ and $\hat{v}_i = v_{iy}/v_{ix}$, the new variables obey (1). The solutions of the parametric interactions that we have discussed then translate to time-independent solutions for a system with a beam of a_1 of finite width propagating in from the edge of the medium.

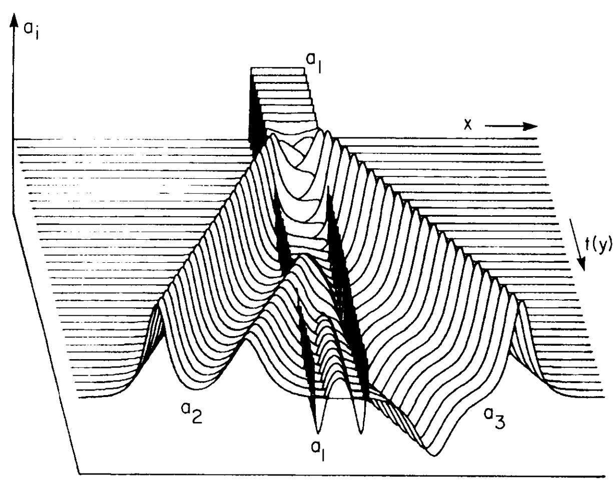

Fig. XII-5. Three-dimensional plot of the interaction shown in Fig. XII-3.

The correspondence between these two-dimensional steady-state equations and the one-dimensional equations is clarified by Figs. XII-5 and XII-6. Figure XII-5 is a three-dimensional plot of the solution shown in Fig. XII-3. Note that the t axis can equally well correspond to another spatial dimension, y. The steady-state solution corresponds to a nonlinear filamentation of the decay products of a parametric decay.

Figure XII-6 is a three-dimensional plot of an explosively unstable interaction. Again the t axis could equally well correspond to another spatial dimension.

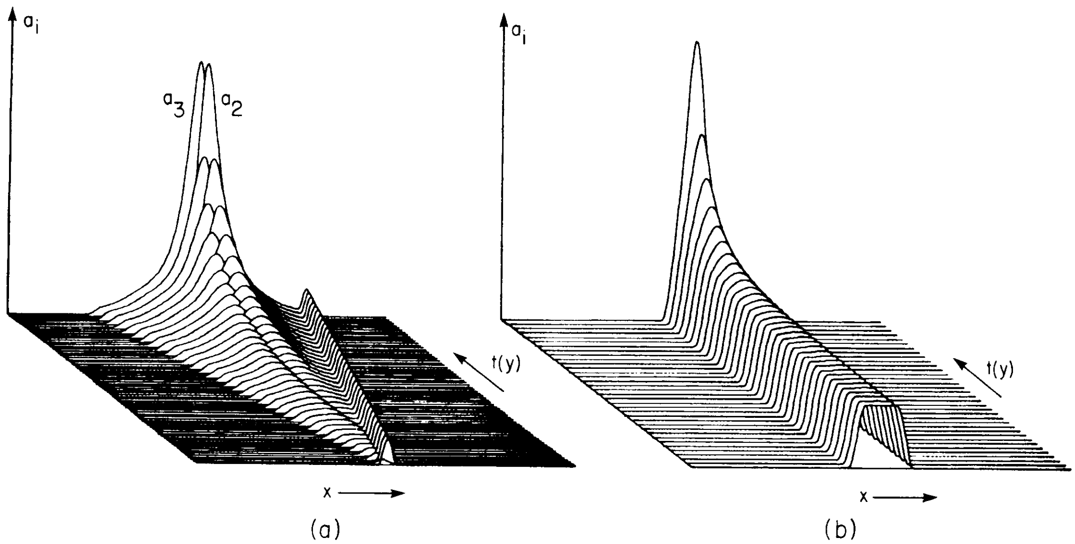

Fig. XII-6. Three-dimensional plot of an explosively unstable interaction, $p_1 = -1$, $p_2 = p_3 = 1$. (a) Development of a_2 and a_3. (b) Development of a_1.

Figure XII-6a is a plot of a_2 and a_3. We have omitted a_1 from this plot to allow the buildup of the normal mode to be visible. The development of a_1 is plotted in Fig. XII-6b. Note that a_1 is perturbed only slightly until $|a_2|$ and $|a_3|$ become comparable to it. It then begins to grow explosively.

References

1. A. Bers, in Plasma Physics – Les Houches 1972 (Gordon and Breach Science Publishers, New York, London, Paris, 1975), Section V.
2. A. Reiman and A. Bers, in Proceedings of the Seventh Conference on Numerical Simulation of Plasmas, Courant Institute, New York University, 1975, pp. 188-191.
3. A. Bers and A. Reiman, in Proceedings of the Seventh Conference on Numerical Simulation of Plasmas, Courant Institute, New York University, 1975, pp. 192-195.
4. D. J. Kaup (to appear in Stud. Appl. Math.).
5. V. E. Zakharov and S. V. Manakov, Soviet Phys. – JETP Letters 18, 243 (1973); S. V. Manakov and V. E. Zakharov (to be published). We note that our results directly contradict some of the claims made by Zakharov and Manakov. The most significant such contradiction is our finding that when wave 1 has a velocity intermediate between that of the other two waves it can indeed lose most of its energy to the other waves.
6. A. Bers, A. Reiman, and D. J. Kaup, Bull. Am. Phys. Soc. 20, 1291 (1975).
7. R. C. Davidson, Methods in Nonlinear Plasma Theory (Academic Press, Inc., New York, 1972), Section 6.4.
8. A. Bers, Plasma Physics – Les Houches 1972, op. cit., p. 197.
9. M. J. Ablowitz, D. J. Kaup, A. C. Newell, and H. Segur, Stud. Appl. Math. 53, 249 (1974).

2. NONLINEAR EVOLUTION OF STIMULATED BACKSCATTERING

National Science Foundation (Grant ENG75-06242)

David J. Kaup, Allan H. Reiman, Abraham Bers

The stimulated backscatter interaction in a homogeneous plasma is described by

$$\left(\frac{\partial}{\partial t} + v_1 \frac{\partial}{\partial x}\right) a_1 = K a_2 a_3 \tag{1a}$$

$$\left(\frac{\partial}{\partial t} + v_2 \frac{\partial}{\partial x}\right) a_2 = -K^* a_1 a_3^* \tag{1b}$$

$$\left(\frac{\partial}{\partial t} + v_3 \frac{\partial}{\partial x}\right) a_3 = -K^* a_1 a_2^* \tag{1c}$$

with $v_1 > v_2 > v_3$ and $|v_1 - v_2| \approx |v_2 - v_3|$. Previous work by others has been concerned with solutions that are dominated by the presence of a boundary, focusing in particular on the steady-state solution.[1-3] We have investigated the fully nonlinear stimulated backscatter interaction of pulses.

Figures XII-7 and XII-8 show solutions of Eqs. 1 for two different sets of parameters. Graphs of the initial pulse profiles are shown in Figs. XII-7a and XII-8a. The initial parameters corresponding to Fig. XII-7 are such that little interaction takes place. The pulse profiles after interaction (Fig. XII-7b) show that the backscattered pulse a_3 is small relative to the injected pulse a_1. In Fig. XII-8 we decrease the velocities by a factor of 5 and find that the interaction is quite large. The pulse profiles after interaction (Fig. XII-8b) show that much of the energy of the incoming pulse goes into the backscattered pulse. Note also the striking spatial modulation of the final amplitudes.

In our investigation of the stimulated backscatter interaction using the inverse scattering method we have been particularly concerned with the calculation of the reflection coefficient R. We define R as the ratio of backscattered-to-injected action.

$$R \equiv \frac{\int_{-\infty}^{\infty} |a_2(x, t \to \infty)|^2 \, dx}{\int_{-\infty}^{\infty} |a_1(x, t=0)|^2 \, dx}. \tag{2}$$

The ratio of backscattered-to-injected energy is $\frac{\omega_2}{\omega_1} R$. This is a particularly important number in determining the feasibility of the laser-pellet fusion scheme.

In the inverse scattering formulation there is a Zakharov-Shabat (Z-S) scattering problem associated with each initial pulse:[4,5]

$$v_{1x} + i\lambda v_1 = q v_2 \tag{3a}$$

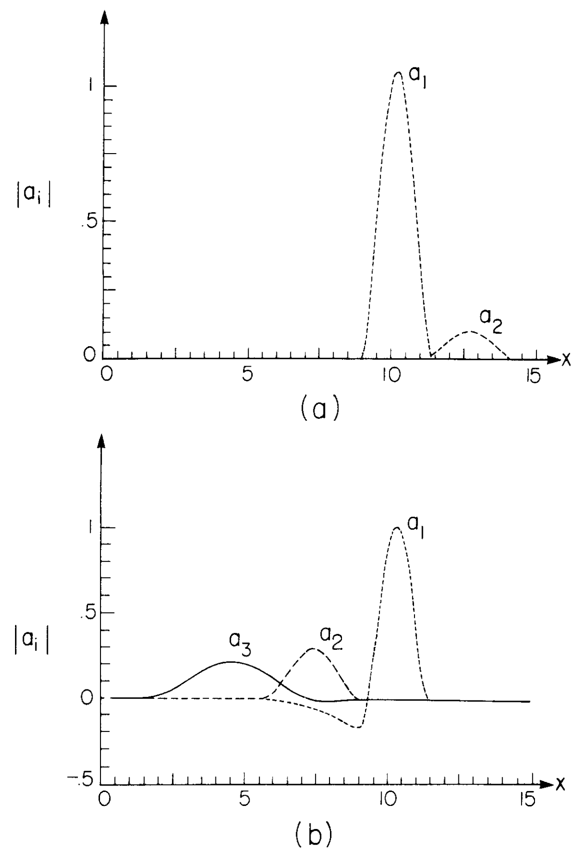

Fig. XII-7. Numerical solution of Eqs. 1 for $v_3 = -1$, $v_2 = .5$, $K = 1$. Graphs are in the reference frame of a_1. (a) Initial profiles. (b) Profile after interaction.

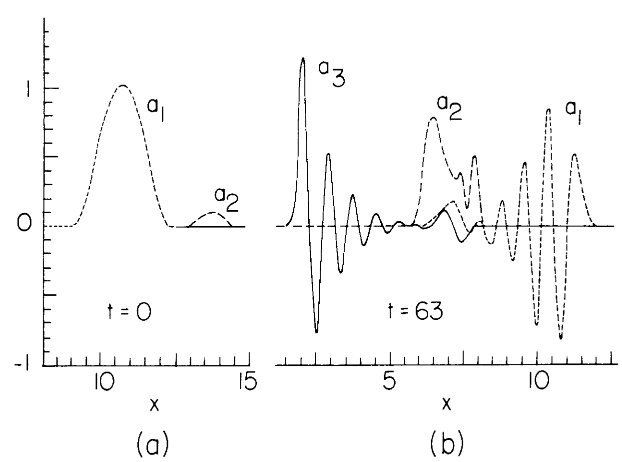

Fig. XII-8. Numerical solution of Eqs. 1 for $v_3 = -.2$, $v_2 = -.1$. (a) Initial profiles. (b) Profile after interaction.

$$v_{2x} - i\lambda v_2 = rv_i. \tag{3b}$$

The q for each pulse is

$$q_1 = \frac{|K|\ e^{i\nu/3}\ a_1^*}{\sqrt{(v_2-v_1)(v_3-v_1)}} \tag{4a}$$

$$q_2 = \frac{|K|\ e^{-i\nu/3}\ a_2}{\sqrt{(v_2-v_1)(v_3-v_2)}} \tag{4b}$$

$$q_3 = -\frac{|K|\ e^{i\nu/3}\ a_3}{\sqrt{(v_2-v_3)(v_1-v_3)}}, \tag{4c}$$

where $K = |K|\ e^{i\nu}$. For pulses a_1 and a_2, $r = q^*$, while for pulse a_3, $r = -q^*$. Because of the self-adjointness of the Z-S operator for $r = q^*$, pulses a_1 and a_3 can contain no solitons. Therefore there can be no soliton exchange. To understand the behavior of the stimulated backscatter interaction, we must look more closely at the continuous part of the spectrum of the Z-S operator.

Let $\phi(x)$ be a solution of Eqs. 3 such that $\phi(x) \to \begin{pmatrix} 1 \\ 0 \end{pmatrix} e^{-i\lambda x}$ as $x \to -\infty$. We define

$$a(\lambda) \equiv \lim_{x\to\infty} \phi_1(x). \tag{5a}$$

Similarly, let $\bar{\phi}(x)$ be a solution of Eqs. 3 such that $\bar{\phi}(x) \to \begin{pmatrix} 0 \\ -1 \end{pmatrix} e^{i\lambda x}$ as $x \to -\infty$. Then

$$\bar{a}(\lambda) \equiv - \lim_{x\to\infty} \bar{\phi}_2(x). \tag{5b}$$

Define also

$$\Gamma(\lambda) \equiv [\bar{a}(\lambda)\, a(\lambda)]^{\pm 1} \tag{6}$$

for $r = \pm q^*$. The action contained in each wave can be expressed directly in terms of Γ. Equate the integral representation for a with the asymptotic expansion for a as $|\lambda| \to \infty$ in the upper half-plane. The coefficient of the first-order term in $1/\lambda$ gives

$$\int_{-\infty}^{\infty} |q|^2\ dx = \frac{1}{\pi} \int_{-\infty}^{\infty} d\lambda\ \ln\,[1 + \Gamma(\lambda)] \tag{7}$$

when there are no solitons. This gives us a formula for the total backscattered action if we can determine the time asymptotic value of $\Gamma^{(3)}(\lambda)$.

To express the time asymptotic Z-S scattering data in terms of the initial Z-S scattering data, we employ the factorized form of the scattering matrix for the Zakharov-Manakov (Z-M) scattering problem.[5,6] Initially we have

$$S = S_o^{(1)} S_o^{(2)}, \tag{8}$$

where $S_o^{(1)}$ and $S_o^{(2)}$ are the matrices for scattering off pulses a_1 and a_2 at $t = 0$. The elements of $S_o^{(1)}$ and $S_o^{(3)}$ are determined by the solution of the corresponding Z-S scattering problem at $t = 0$. As $t \to \infty$ the envelopes again separate to give

$$S = S_f^{(3)} S_f^{(2)} S_f^{(1)}. \tag{9}$$

The elements of these matrices are determined by the solution of the corresponding Z-S scattering problem for $t \to \infty$. By equating the elements of expressions (8) and (9) for S, we find the time asymptotic scattering data in terms of the initial scattering data. In particular, we find

$$\Gamma_f^{(3)} = \frac{\Gamma_o^{(1)} \Gamma_o^{(2)}}{1 + \Gamma_o^{(2)}}. \tag{10}$$

In conjunction with Eqs. 7 and 2, this gives the exact expression for R:

$$R = \frac{\int_{-\infty}^{\infty} d\lambda \ln\left(1 + \dfrac{\Gamma_o^{(1)} \Gamma_o^{(2)}}{1 + \Gamma_o^{(2)}}\right)}{\pi \int_{-\infty}^{\infty} |q_1|^2 \, dx}. \tag{11}$$

To calculate the backscattered energy, we need only calculate the Z-S scattering data. This is particularly simple if initially we have square pulses. In that case the Z-S equations have closed-form solutions that for the Γ_o yield

$$\Gamma_o^{(1)}(\lambda) = A_1^2 G\left(L_1^2 \lambda^2 - A_1^2\right) \tag{12a}$$

$$\Gamma_o^{(3)}(\lambda) = A_3^2 G\left(4L_3^2 \lambda^2 - A_3^2\right) \tag{12b}$$

where

$$G(x) = \frac{\sin^2((x)^{1/2})}{x}, \tag{12c}$$

L_i is the width of pulse a_i, and $A_i = |q_i|\ L_i$.

Equations 12 may now be substituted in Eq. 11 to obtain the reflection coefficient for the given initial parameters. In Fig. XII-9 we have plotted R against L_1 for several values of L_2. Note the threshold in R as a function of L_1. We can obtain an expression for this threshold by solving for $\Gamma_f^{(3)} > 1$ using Eqs. 10 and 12. Making the approximations $|q_3(t=0)| \ll |q_1(t=0)|$ and $A_3 \ll 1$ at $t = 0$, at threshold we obtain

$$A_2 e^{A_3} = 1. \tag{13}$$

In particular, note that in the vicinity of the threshold pulse compression can have a great effect on the reflection coefficient.

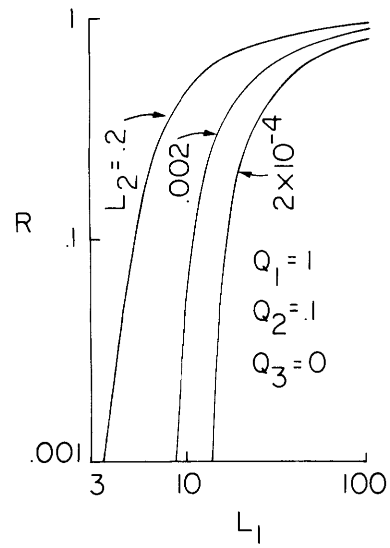

Fig. XII-9.
R plotted as a function of L_1 using Eqs. 11 and 12.

We may derive the reflection threshold in an alternative fashion if we ask for the conditions under which the linear undepleted pump solution of Eqs. 1 becomes invalid. The linear solution is $a_2(t) = a_2(0)\, e^{\gamma t}$, $a_3(t) = a_3(0)\, e^{\gamma t}$ with $\gamma = |Ka_1(t=0)|$ at the point of maximum growth. The condition that depletion be important across the width of a_3 is $L_3 \frac{\partial a_1}{\partial x} = a_1$. Substituting in Eq. 1a and assuming an interaction time of $\frac{L_1}{v_1 - v_2}$, we find that the threshold amplitudes obey $A_3 e^{A_1} = \frac{\sqrt{2}}{2}$. This is approximately the same as Eq. 13.

We can obtain an approximate closed-form expression for the reflection coefficient of square pulses when $A_1 \gg 1$ and $A_1A_3 \ll 1$ at $t = 0$. An approximate evaluation of Eqs. 11 and 12 then gives

$$R \approx 1 - \frac{2}{\pi} \sin^{-1}\left(\frac{B}{A_3}\right) - \frac{2}{\pi}\frac{B-1}{A_3}\left(1 - \frac{B^2}{A_3^2}\right)^{1/2}$$

$$- \frac{2}{\pi A_3} \ln \left| \frac{1 + \left(1 - B^2/A_3^2\right)^{1/2}}{1 - \left(1 - B^2/A_3^2\right)^{1/2}} \right| \tag{14}$$

for $B < A_3$ and $R \approx 0$ for $B > A_3$, where B is the solution of

$$\frac{\sinh(B)}{B} = \frac{1}{A_3A_2}.$$

References

1. R. Harvey and G. Schmidt, Stevens Institute of Technology Research Report No. COO-3004-6 (1974).
2. W. M. Manheimer, Phys. Fluids 17, 1634 (1974).
3. D. W. Forslund, J. M. Kindel, and E. L. Lindman, Phys. Fluids 18, 1002 (1975).
4. M. J. Ablowitz, D. J. Kaup, A. C. Newell, and H. Segur, Stud. Appl. Math. LIII, 249 (1974).
5. D. J. Kaup (to appear in Stud. Appl. Math.).
6. V. E. Zakharov and S. V. Manakov, Sov. Phys. – JETP Letters 18, 243 (1973).

3. SPACE-TIME EVOLUTION OF THREE-WAVE INTERACTIONS IN AN INHOMOGENEOUS PLASMA

National Science Foundation (Grant ENG75-06242)

Allan H. Reiman, Abraham Bers, David J. Kaup

We have extended the theory of three-wave nonlinear interactions described in Section XII-A.1 and XII-A.2 to include the effects of linear inhomogeneity. The effect of such an inhomogeneity on just the linear initial stage of parametric interaction has been studied extensively.[1] Inhomogeneity effects are of particular importance in the laser-pellet interaction where strong density gradients may be driven by the laser.[2] These effects can also influence the absorption of microwave energy by a Tokamak plasma.

We have found an exact transformation of the equations with a linear inhomogeneity to the homogeneous equations. This allows us to apply inverse scattering techniques developed for the homogeneous case. We do this in conjunction with numerical solution of the inhomogeneous equations for initial conditions that we investigated previously for the homogeneous interaction.

The x-t equations describing the time development of the three-wave parametric interaction in a one-dimensional plasma with linear inhomogeneity are

$$\left(\frac{\partial}{\partial t} + v_1 \frac{\partial}{\partial x}\right) a_1 = p_1 K a_2 a_3 \exp(ik'x^2/2) \tag{1a}$$

$$\left(\frac{\partial}{\partial t} + v_2 \frac{\partial}{\partial x}\right) a_2 = -p_2 K^* a_1 a_3^* \exp(-ik'x^2/2) \tag{1b}$$

$$\left(\frac{\partial}{\partial t} + v_3 \frac{\partial}{\partial x}\right) a_3 = -p_3 K^* a_1 a_2^* \exp^{(-ik'x^2/2)}, \tag{1c}$$

where k' is the spatial derivative of the wave number mismatch. To transform these equations we define hatted amplitudes.

$$\hat{a}_j \equiv a_j \exp\left(i(x-v_j t)^2 k'\theta_j/2\right) \tag{2a}$$

$$\theta_1 \equiv -\frac{v_2 v_3}{(v_2-v_1)(v_3-v_1)} \tag{2b}$$

$$\theta_2 \equiv \frac{v_1 v_3}{(v_1-v_2)(v_3-v_2)} \tag{2c}$$

$$\theta_3 \equiv \frac{v_1 v_2}{(v_3-v_1)(v_3-v_2)}. \tag{2d}$$

We have simply multiplied the a by phase factors quadratic in x and t. We then substitute in Eqs. 1 to find that the hatted variables satisfy

$$\left(\frac{\partial}{\partial t} + v_1 \frac{\partial}{\partial x}\right) \hat{a}_1 = p_1 K \hat{a}_2 \hat{a}_3 \tag{3a}$$

$$\left(\frac{\partial}{\partial t} + v_2 \frac{\partial}{\partial x}\right) \hat{a}_2 = -p_2 K^* \hat{a}_1 \hat{a}_3^* \tag{3b}$$

$$\left(\frac{\partial}{\partial t} + v_3 \frac{\partial}{\partial x}\right) \hat{a}_3 = -p_3 K^* \hat{a}_1 \hat{a}_2^*. \tag{3c}$$

These are just the equations describing the three-wave interaction in a homogeneous medium. Thus we see that the nonlinear three-wave interaction with a linear k mismatch is equivalent to a homogeneous three-wave interaction of pulses that have been chirped (that is, have a frequency modulation quadratic in t).

The effect of a linear inhomogeneity on the two-dimensional steady-state (x-y) equations can be somewhat more complicated. Now the gradient of the inhomogeneity can have components in both x and y directions. Thus we now have a tensor $\overleftrightarrow{k}$: the vector derivative of the vector $\vec{k}$ mismatch. The equations are

$$\left(v_{1y} \frac{\partial}{\partial y} + v_{1x} \frac{\partial}{\partial x}\right) b_1 = p_1 K b_2 b_3 \exp(i\vec{r} \cdot \overleftrightarrow{k} \cdot \vec{r}) \tag{4a}$$

$$\left(v_{2y} \frac{\partial}{\partial y} + v_{2x} \frac{\partial}{\partial x}\right) b_2 = -p_2 K^* b_1 b_3^* \exp(-i\vec{r} \cdot \overleftrightarrow{k} \cdot \vec{r}) \tag{4b}$$

$$\left(v_{3y} \frac{\partial}{\partial y} + v_{3x} \frac{\partial}{\partial x}\right) b_3 = -p_3 K^* b_1 b_2^* \exp(-i\vec{r} \cdot \overleftrightarrow{k} \cdot \vec{r}), \tag{4c}$$

where $\vec{r}$ is the position vector.

The transformation to be applied to Eqs. 4 is correspondingly more compliceted than that for Eqs. 1, although it still corresponds to multiplying by a phase factor quadratic in x and y. Define

$$\hat{b}_j \equiv b_j \exp\left(i(v_{jx}y - v_{jy}x)^2 \phi_j/2\right) \tag{5a}$$

$$\phi_1 \equiv \frac{(k'_{yy}v_{2y} + k'_{xy}v_{2x})\, v_{3y} + (k'_{xy}v_{2y} + k'_{xx}v_{2x})\, v_{3x}}{(v_{1x}v_{2y} - v_{1y}v_{2x})(v_{1x}v_{3y} - v_{1y}v_{3x})} \tag{5b}$$

$$\phi_2 \equiv \frac{(k'_{yy}v_{1y} + k'_{xy}v_{1x})\, v_{3y} + (k'_{xy}v_{1y} + k'_{xx}v_{1x})\, v_{3x}}{(v_{1x}v_{2y} - v_{1y}v_{2x})(v_{2x}v_{3y} - v_{2y}v_{3x})} \tag{5c}$$

$$\phi_3 \equiv -\frac{(k'_{yy}v_{1y} + k'_{xy}v_{1x})\, v_{2y} + (k'_{xy}v_{1y} + k'_{xx}v_{1x})\, v_{2x}}{(v_{1x}v_{3y} - v_{1y}v_{3x})(v_{2x}v_{3y} - v_{2y}v_{3x})}. \tag{5d}$$

The hatted variables then satisfy

$$\left(v_{1y} \frac{\partial}{\partial y} + v_{1x} \frac{\partial}{\partial x}\right) \hat{b}_1 = p_1 K \hat{b}_2 \hat{b}_3 \tag{6a}$$

$$\left(v_{2y} \frac{\partial}{\partial y} + v_{2x} \frac{\partial}{\partial x}\right) \hat{b}_2 = -p_2 K^* \hat{b}_1 \hat{b}_3^* \tag{6b}$$

$$\left(v_{3y} \frac{\partial}{\partial y} + v_{3x} \frac{\partial}{\partial x}\right) \hat{b}_3 = -p_3 K^* \hat{b}_1 \hat{b}_2^*. \tag{6c}$$

These are the equations describing the homogeneous steady-state interaction in two dimensions. If all of the v_{iy} are positive, Eqs. 6 can be further transformed to Eqs. 3.

What we must solve, of course, is not just the equations themselves but the equations subject to initial and boundary conditions. We must see how these initial and boundary conditions are modified by the transformations that we have employed.

As $x \to \pm\infty$, we require that $a_j(x,t) \to 0$, $b_j(x,y) \to 0$. We are looking at interactions of pulses. This condition remains unchanged for the hatted variables: as $x \to \pm\infty$, $\hat{a}_j(x,t) \to 0$, $\hat{b}_j(x,y) \to 0$.

For the x-t equations we impose an initial condition at $t = 0$. The corresponding initial condition for $\hat{a}_j$ is

$$\hat{a}_j(x, t=0) = \exp\left(ik'\theta_j x^2/2\right)\, a_j(x, t=0).$$

Similarly, since we assume $v_{jy} > 0$ in Eqs. 4, we impose a boundary condition at $y = 0$ for these equations. The corresponding boundary condition for $\hat{b}_j$ is

$$\hat{b}_j(x, y=0) = \exp\left(iv_{iy}^2\phi_j x^2/2\right) b_j(x, y=0).$$

Once the initial conditions are imposed, the time development of $\hat{a}_j$ (spatial development of $\hat{b}_j$) is determined completely by the homogeneous equations. To find $a_j(x,t)$ or $b_j(x,y)$ we use Eqs. 2 or 5. Thus the three-wave interactions of pulses in a plasma with linear inhomogeneity is exactly equivalent to the homogeneous three-wave interaction of pulses with chirped initial conditions. This result is of particular interest because the interaction of chirped pulses has been the subject of much research.

In Fig. XII-10 we illustrate the transformation of an initial square pulse of constant phase. We have plotted the real parts of a_j and $\hat{a}_j$ at $t = 0$.

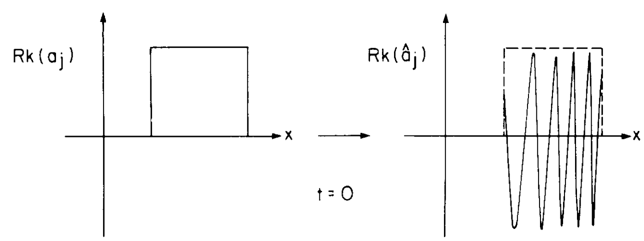

Fig. XII-10. Transformation of the initial condition for amplitudes.

Simulated Scatter

In Fig. XII-11a we have plotted initial and final pulse profiles obtained from a numerical solution of the homogeneous three-wave interaction with $v_1 > v_2, v_3$. In the context of the x-t equations (1) this interaction corresponds to stimulated backscatter. The interaction has an alternative interpretation in the context of the two-dimensional steady-state equations (4) as sidescatter off an obliquely incident beam. We assumed the latter interpretation in inserting the linear inhomogeneity to obtain the numerical solutions shown in Fig. XII-11b and XII-11c. Note that the scattered energy has been reduced in Fig. XII-11b. In Fig. XII-11c the inhomogeneity has been increased still further, and the scatter is almost completely suppressed.

In Fig. XII-12 we have indicated schematically the dependence of the reflection coefficient R on the length of pulse a_1 and on the inhomogeneity. For the homogeneous interaction with L_1 small, R is approximately zero. As L_1 is increased we reach a threshold, enter a nonlinear regime, and then see a saturation as R approaches 1. By allowing k' to increase at constant L_1, R decreases and again enters a nonlinear region, and finally approaches zero.

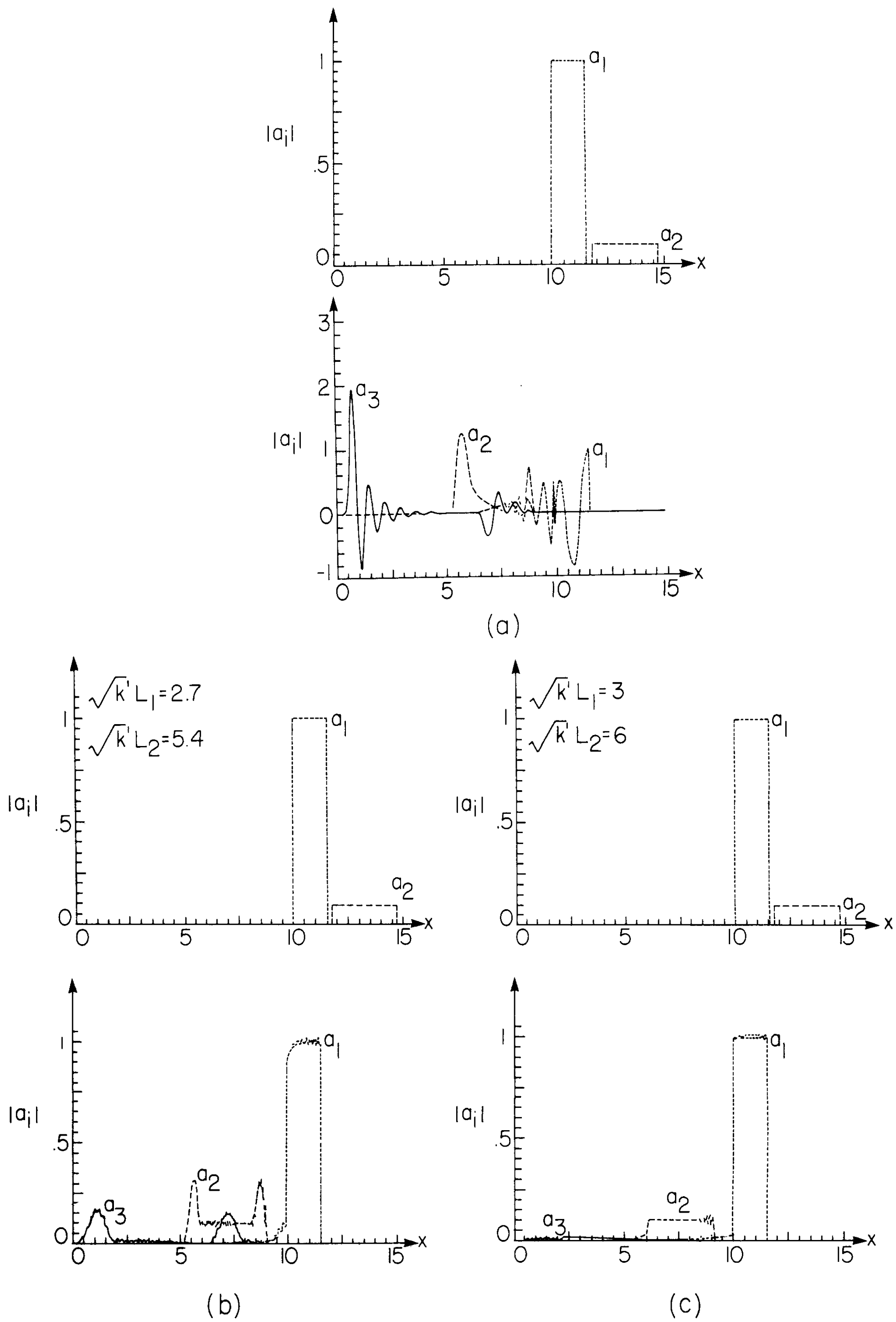

Fig. XII-11. (a) Pulse profiles before and after interaction for a homogeneous scattering interaction. Graphs are in the reference frame of a_1. $v_3 = -.3$, $v_2 = -.15$, $K = 1$.

(b) Same interaction as (a) except for inhomogeneity inserted in the reference frame of a_1.

(c) Same interaction as (b) except for larger k'.

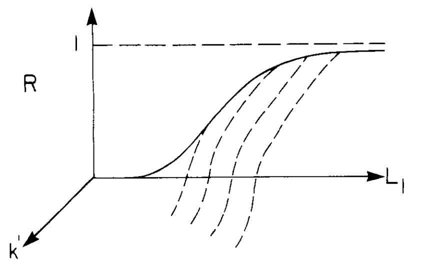

Fig. XII-12.
Schematic dependence of the reflection coefficient on the length of a_1, L_1 and on the inhomogeneity parameter k'.

We have found an exact expression for R which includes the effects of the inhomogeneity. The scattered action $N_f^{(3)}$, defined by

$$N_f^{(3)} \equiv \int_{-\infty}^{\infty} |a_3(x, t\to\infty)|^2 \, dx$$

can be expressed directly in terms of the time asymptotic scattering data

$$N_f^{(3)} = \frac{|(v_2-v_3)(v_1-v_3)|}{|K|^2 \pi} \int_{-\infty}^{\infty} dx \ln\left[1+\Gamma_f^{(3)}(\lambda)\right].$$

The formula that we used in the homogeneous case to express Γ_f in terms of the initial scattering data is still applicable.

$$\Gamma_f^{(3)} = \frac{\Gamma_o^{(1)}\Gamma_o^{(2)}}{1+\Gamma_o^{(2)}}.$$

From the solution of the scattering problem for the Z-S equations we obtain the Γ_o:

$$\phi_{1x} + i\lambda\phi_1 = q\phi_2$$

$$\phi_{2x} - i\lambda\phi_2 = r\phi_1$$

with q and r determined by the initial pulse profiles and $r = \pm q^*$. In the homogeneous case, if we take the a_j to be square pulses of constant phase, then q and r are also square pulses of constant phase. The Z-S scattering problem is then exactly soluble in terms of trigonometric functions. In the inhomogeneous case, if we take the a_j to be square pulses, then $\hat{a}_j$ and q are modulated square pulses. The Z-S scattering problem is still exactly soluble, but now in terms of parabolic cylinder functions rather than trigonometric functions.

Parametric Decay to Solitons

In Fig. XII-13a we show a three-dimensional plot of a homogeneous parametric decay of wave 1. In the context of the two-dimensional steady-state equations this corresponds to the steady-state decay of a beam incident from the top of Fig. XII-13a, with nonlinear filamentation of the decay products. Note that by the time the interaction has gone to completion there is little energy left in the pump. In Fig. XII-13b we see the same interaction with the linear inhomogeneity present. The low-frequency waves now take longer to build up. The resulting filaments are more closely spaced, narrower, and have smaller amplitude. Even after the interaction has gone to completion much of the initial energy remains in the pump.

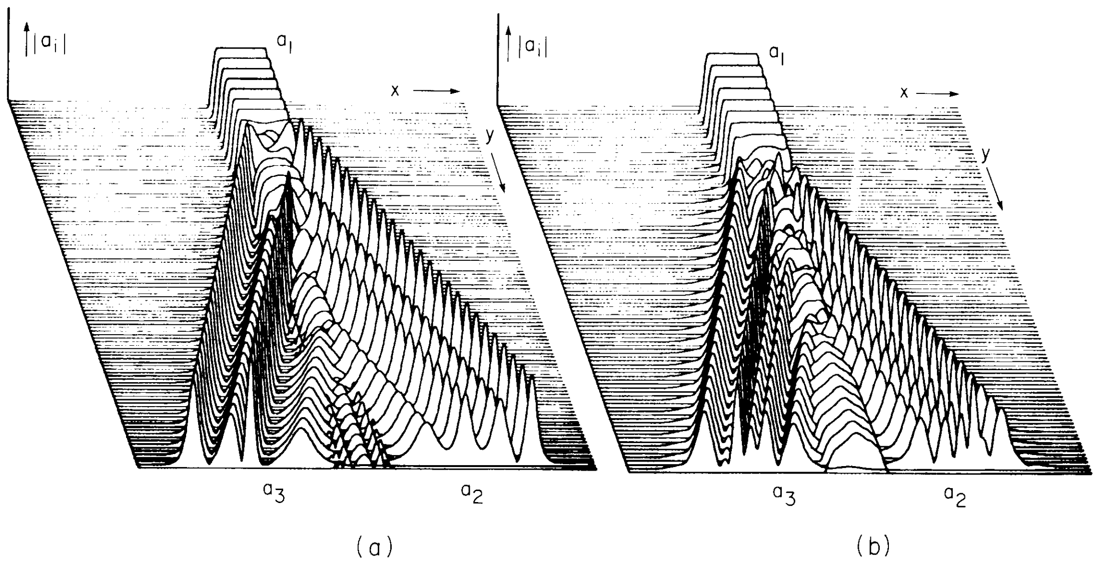

Fig. XII-13. (a) Homogeneous parametric decay: $-v_{3x} = v_{2x} = 1$.
$$\frac{|Ka_1(y=0)|\, L_1}{\sqrt{|v_2 v_3|}} = L_1 = 12.8.$$
(b) Same interaction as (a) except for the inhomogeneity inserted. $\sqrt{k'}\, L = 9.05$. $\lambda \equiv \dfrac{|Ka_1(y=0)|^2}{k' v_1 v_2} = 2.$

As in the homogeneous case, we may express the asymptotic profiles of the filaments in terms of an n-soliton formula. The Z-S equations for a_1 are again equivalent to the linearized three-wave equations for large a_1 and small a_2, a_3. In the x-t interaction these are the familiar equations for parametric decay in the presence of a linear inhomogeneity.

$$\left(\frac{\partial}{\partial t} + v_2 \frac{\partial}{\partial x}\right) a_2 = -p_2 K^* a_1 a_3^* \exp(-ik'x^2/2) \tag{7a}$$

$$\left(\frac{\partial}{\partial t} + v_3 \frac{\partial}{\partial x}\right) a_3 = -p_3 K^* a_1 a_2^* \exp(-ik'x^2/2). \tag{7b}$$

The number of solitons in the inverse scattering formulation, and hence the number of filaments formed, is just equal to the number of growing normal modes of the linear equations (7). The soliton eigenvalues, and hence the heights and widths of the filaments, are proportional to the growth rates of the corresponding modes. The soliton phase, and hence the position of the corresponding filament, may be determined from the eigenfunction of the corresponding eigenmode.

The growing normal modes of Eqs. 7, of course, have been thoroughly investigated numerically, by the WKB method and through the exact solution for $|a_1(x, t=0)|$ square. In Fig. XII-14 we show the numerical solution of Dubois, Forslund, and Williams[3] for the growth rates in a square pump vs the width of the pump. The inhomogeneity is the same as in Fig. XII-13b. We have indicated by an arrow the corresponding width of our pump. Note that this graph predicts the existence of 5 growing normal modes for a pump of that width (two pairs of which have degenerate growth rates). We do indeed see the formation of 5 filaments in Fig. XII-13b.

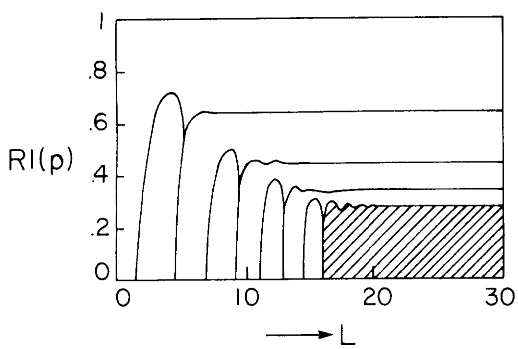

Fig. XII-14.
Dispersion graph of Dubois, Forslund, and Williams[3] for a square pump with inhomogeneity parameters $\lambda \equiv \frac{|Ka_1(t=0)|^2}{k'v_1v_2} = 2.$ Arrow indicates that L = 12.8, corresponding to $\sqrt{k'}\ L = 9.05$, the pump width used to obtain Fig. XII-13b.

Conclusion

We have found an exact transformation of the inhomogeneous nonlinear problem to the homogeneous nonlinear problem. The homogeneous nonlinear problem can be solved by using the complementary techniques of a numerical integration of the equations, the inverse scattering method, and the theory of the linear mode buildup.

References

1. For a review of this work, see F. W. Chambers, "Space-Time Evolution of Instabilities in Laser-Plasma Interactions," Ph.D. Thesis, Department of Physics, M.I.T., August 1975.
2. W. L. Kruer, E. J. Valeo, and K. G. Estabrook, Phys. Rev. Letters 35, 1076 (1975).
3. D. F. Dubois, D. W. Forslund, and E. A. Williams, Phys. Rev. Letters 33, 1013 (1974).

B. Plasma Research Related to Fusion

Research – Theoretical

1. NONLINEAR SATURATION OF THE DISSIPATIVE TRAPPED ION INSTABILITY

U. S. Energy Research and Development Administration (Contract E(11-1)-3070)

David A. Ehst, Thomas H. Dupree

Introduction

Recently, it has been predicted by linear theory that several low-frequency instabilities jeopardize plasma confinement in Tokamaks. We consider one of these, the dissipative trapped ion mode, which occurs in the banana regime $\left(\frac{\nu_i}{\epsilon}, \frac{\nu_e}{\epsilon} \ll \omega_i^T, \omega_e^T\right)$ but is characterized by a negligible magnetic drift frequency $\left(\omega^{\nabla B} \ll \frac{\nu_i}{\epsilon}, \frac{\nu_e}{\epsilon}\right)$. Our interest centers on flutelike modes which have small linear Landau damping, $\omega_r \ll \omega^T$ and $\omega_r/K_{\|} \ll V_{th}$ but $K_{\|} \ll (Rq)^{-1}$. Our goal is to understand the mechanism driving the linear instability and to evaluate various nonlinear phenomena to determine the saturated amplitude of the fluctuations and their influence on particle transport.

The original work on this mode[1] utilized the fluid equations to analyze wave motion. For the trapped species (those particles which, in the absence of collisions, are restricted by the $\underline{B}$ field modulation to localized regions along $\underline{B}$) the continuity equation may be written

$$\frac{\partial n^T}{\partial t} + \frac{\partial}{\partial \underline{r}} [n^T \underline{V}] = -\frac{\nu}{\epsilon}\left(n^T - \sqrt{2\epsilon}\; n_o\right). \tag{1}$$

Substituting $\underline{V}$ from the momentum equation, we see that the trapped fluids have linear wave perturbations

$$\tilde{n}_j^T = \frac{\sqrt{2\epsilon}\; i\omega_{*j}}{-i\omega + \nu_j/\epsilon} \frac{e_j\phi}{T_j} n_o. \tag{2}$$

Circulating particles are adiabatic with

$$\tilde{n}_j^C \approx -\frac{e_j\phi}{T_j} n_o. \tag{3}$$

Invoking quasi neutrality, we find the dispersion relation for $T_e = T_i$:

$$\omega = \frac{\sqrt{2\epsilon}}{2}\,\omega_{*e} - i\frac{\nu_i}{\epsilon} + \frac{i\omega_r^2}{\nu_e/\epsilon}, \qquad \frac{\nu_i}{\epsilon} \ll \omega_r \ll \frac{\nu_e}{\epsilon}. \tag{4}$$

Our model points out that collisionally induced transitions of particles from trapped to circulating and vice versa allow a "current" of trapped particles along $\underline{B}$. These transitions occur at random; hence, if a (wave) density perturbation exists, trapped particles appear to diffuse from high- to low-density regions. This is the meaning of the collision term in Eq. 1. This erratic motion (diffusion) of trapped particles along $\underline{B}$ means that the trapped particles do not stay in phase with the potential fluctuations, which is reflected by their nonadiabatic response to ϕ (Eq. 2). We shall see that there is a random change of a particle's kinetic energy $\mathscr{E}$ associated with this trapping-detrapping process; this particle energy is exchanged with the wave energy to drive the instability.

Kinetic Theory

Some nonlinear effects (enhanced detrapping) are best studied by following individual particle behavior via the kinetic theory. Circulating particles are assumed to have

$$V_{\parallel} = \text{constant} \equiv V_{\parallel}^{C}$$

$$\underline{r}_{\perp} = \text{constant}$$

so their linear collisionless orbits are represented by

$$g_o^C(-t) = e^{i[K_{\parallel}(s-V_{\parallel}^C t)+\underline{K}_{\perp}\cdot\underline{r}_{\perp}]}.$$

This orbit function is a solution to the linearized, collisionless drift equation, as required: $0 = \left\{\frac{\partial}{\partial t} + V_{\parallel}^{C}\cdot\frac{\partial}{\partial s}\right\} g_o^C(-t)$.

By virtue of the magnetic field modulation, the trapped particles have $V_{\parallel} = V_{\parallel}(\mathscr{E},\mu,\underline{r})$, and their parallel orbits are approximated by a sinusoidal function $S(t) = s + Rq\Theta_o[\sin\{\alpha+\sigma\omega^T t\} - \sin\alpha]$. The magnetic drift is responsible for the radial orbit fluctuation, which gives these orbits their characteristic shape: $R(t) = r_o + \rho_p \cos\{\alpha - \sigma\omega^T t\}$. Thus the linear collisionless orbit is

$$g_o^T(-t) \propto e^{i[K_{\parallel}S(-t)+K_r R(-t)]}. \tag{5}$$

We are aware that the (nonlinear) effect of ϕ is to destroy the constants of the linear motion. One such constant is the banana center r_o; a Lagrangian analysis shows

$$\dot{r}_o = \frac{-cE_{\zeta}}{B_p}. \tag{6}$$

The trapped particles move across a flux surface with $\dot{b} = \frac{-cE_r}{B}$, and their kinetic energy changes as

$$\dot{\mathscr{E}} = eV_{\|}E_{\|}. \tag{7}$$

In terms of the variables $(t, s, r_o, b, \mathscr{E}, \mu)$ the drift equation is

$$C(f) = \left\{\frac{\partial}{\partial t} + \dot{s}\,\frac{\partial}{\partial s} + \dot{r}_o\,\frac{\partial}{\partial r_o} + \dot{b}\,\frac{\partial}{\partial b} + \dot{\mathscr{E}}\,\frac{\partial}{\partial \mathscr{E}}\right\} f$$

$$= \left\{\frac{\partial}{\partial t} + V_{\|}\,\frac{\partial}{\partial s} - \frac{cE_{\zeta}}{B_p}\,\frac{\partial}{\partial r_o} - \frac{cE_r}{B}\,\frac{\partial}{\partial b} + eV_{\|}E_{\|}\,\frac{\partial}{\partial \mathscr{E}}\right\} f. \tag{8}$$

This equation can also be derived from Hazeltine's drift equation[2] by a suitable change of variables. By direct substitution we can show that g_o^T (Eq. 5) is a solution to the linear collisionless version of Eq. 8.

In the presence of collisions or wave turbulence trapped particles will be stochastically perturbed away from their linear collisionless orbits and $g^T(-t)$, which represents wave-particle correlation, will diminish with time:

$$g^T(-t) \approx g_o^T(-t)\, e^{-dt}, \tag{9}$$

where d^{-1} is the time required for a particle's position to randomize relative to the wave motion. In the case of the trapped electrons, their orbits certainly have a random component, since their dynamics is dominated by collisions ($\omega_r \lesssim \nu_e/\epsilon$). Moreover, the ion orbits are also probably randomized because of the presence of a broad wave spectrum. Experiments have consistently shown a wide bandwidth in plasmas containing a collisionless species.[3] We shall show how to replace the collision operator and the nonlinear (wave turbulence) terms in Eq. 8 by constants representing the rate at which various effects act to randomize the linear orbits:

$$0 = \left\{\frac{\partial}{\partial t} + V_{\|}\,\frac{\partial}{\partial s} + d\right\} f. \tag{10}$$

We note that this generalized decorrelation frequency d stresses the similar roles of collisions and turbulence, since it is a sum of terms representing these different effects. Direct substitution shows the perturbed orbit function, Eq. 9, to be a solution to the collisional, nonlinear kinetic equation, Eq. 10.

By following standard methods, the drift equation is solved for the perturbed distribution in terms of an integral over these perturbed orbits.

$$\tilde{f}_j^{C,T} = \frac{-e_j\Phi}{T_j}\, f_{Mj} + \sum_{\underline{K}} i(\omega_{*j} - \omega)\,\frac{e_j}{T_j}\int_0^\infty d\tau\, e^{i[\omega(\tau-t)+\delta]}\,\phi_{\underline{K}}\, g^{C,T}(\tau)\, f_{Mj}.$$

We find the dispersion relation

$$2 \approx \sqrt{2\epsilon}\left\{\frac{\omega-\omega_{*i}}{\omega+id_i}+\frac{\omega-\omega_{*e}}{\omega+id_e}\right\} - \mathcal{R}(d_i, d_e). \tag{11}$$

The "nonresonant" frequencies d within the braces are different from those in $\mathcal{R}$ which serve to broaden the Landau resonances; this emphasizes the fact that the various d must be carefully constructed in light of the many ways in which the linear collisionless orbits can be perturbed.

Quasi-linear Theory

Our first goal is to derive the collisional terms d_c that determine the linear growth rate γ^L. In the process of examining the linear mechanism we also formulate a quasi-linear theory of the dissipative trapped-particle instabilities. By using linear orbits, Eq. 7 is integrated as we follow a particle's history. If the particle is initially circulating with $V_{th} \gg \omega/K_{\parallel}$, it moves quickly through an almost stationary potential wave so $\mathscr{E}(t) \approx \mathscr{E}_o - e\phi'(t)$, where ϕ' is the potential along the particle orbit and $\mathscr{E}_o$ is the (constant) average kinetic energy. Once a collision increases the magnetic moment μ sufficiently to trap the particle, its parallel velocity becomes $V_{\parallel} \approx 0$. Consequently Eq. 7 shows $\mathscr{E}(t) \approx$ constant for the period during which it is trapped. Meanwhile the potential at the trapped particle's position is fluctuating at the wave frequency ω_r, so if another

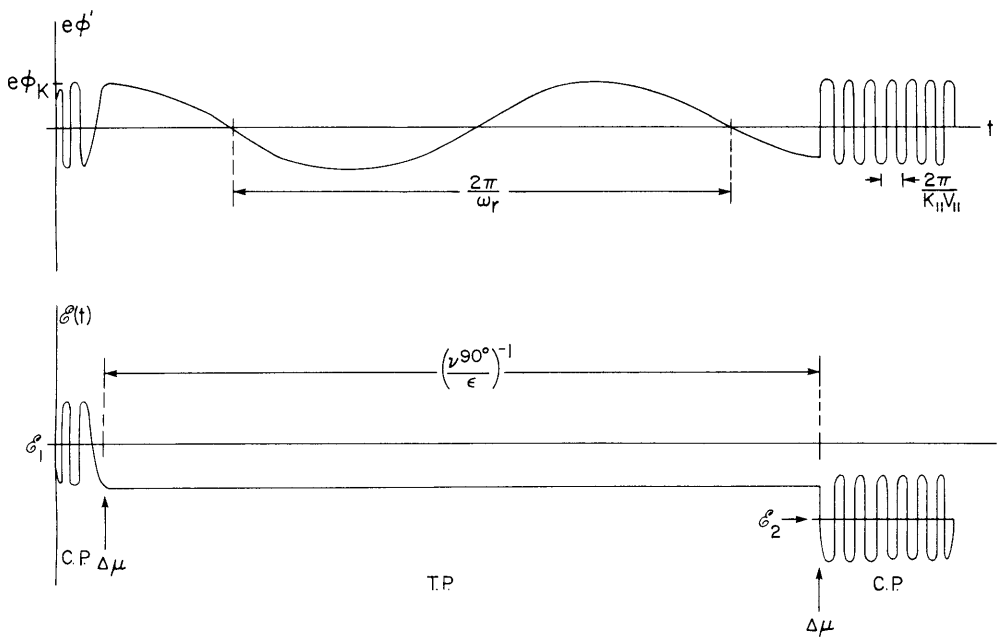

Fig. XII-15. Kinetic energy of particle undergoing trapping and detrapping when $\frac{\nu^{90°}}{\epsilon} \ll \omega_r$.

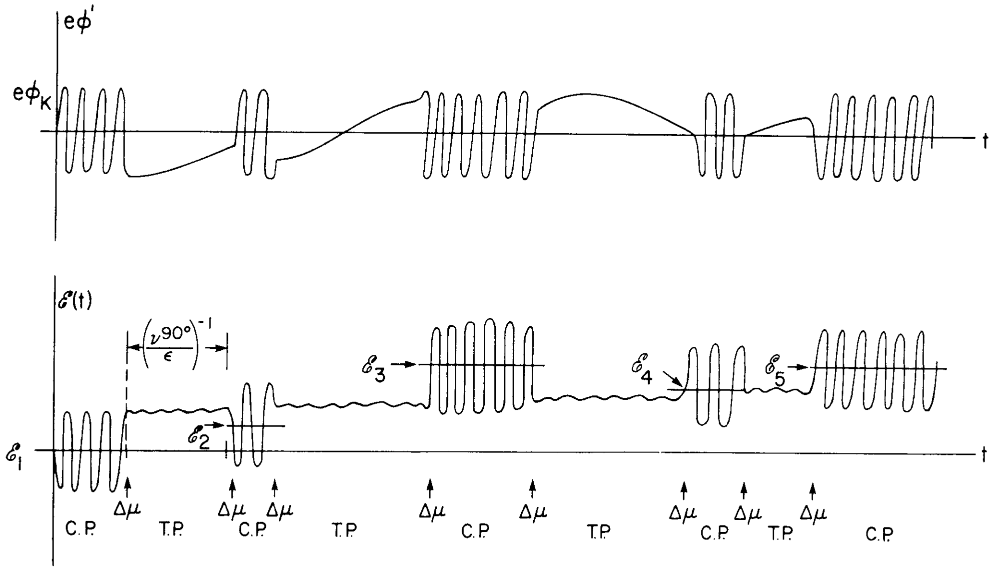

Fig. XII-16. Kinetic energy of particle alternately trapped and circulating when $\frac{\nu^{90°}}{\epsilon} \gg \omega_r$.

collision reduces μ sufficiently to allow further circulation along $\underline{B}$ with $\mathscr{E}(t) = \mathscr{E}_1 - e\phi'(t)$, we find that the initial condition has changed so that $\mathscr{E}_1 - \mathscr{E}_o = \Delta\phi$, the change in potential while the particle is trapped. Note that in this model the collisions change μ but not $\mathscr{E}$. The energy history of typical particles is displayed in Figs. XII-15 and XII-16 for different limits of the detrapping frequency ν/ϵ. We find a particle going from circulating to trapped to circulating suffers a secular change in average energy:

$$\Delta\mathscr{E}_o \approx \begin{cases} e\phi, & \frac{\nu}{\epsilon} \ll \omega_r \\[2ex] e\phi \dfrac{\omega_r}{\nu/\epsilon}, & \omega_r \ll \frac{\nu}{\epsilon}. \end{cases} \tag{12}$$

In a similar fashion the linear orbits can be used to integrate Eq. 6 for $r_o(t)$ (see Figs. XII-17 and XII-18). We find

$$\Delta r_o \approx \begin{cases} \dfrac{cK_\zeta\phi}{B_p\omega_r}, & \frac{\nu}{\epsilon} \ll \omega_r \\[2ex] \dfrac{cK_\zeta\phi}{B_p\omega_r} \dfrac{\omega_r}{\nu/\epsilon}, & \omega_r \ll \frac{\nu}{\epsilon}. \end{cases} \tag{13}$$

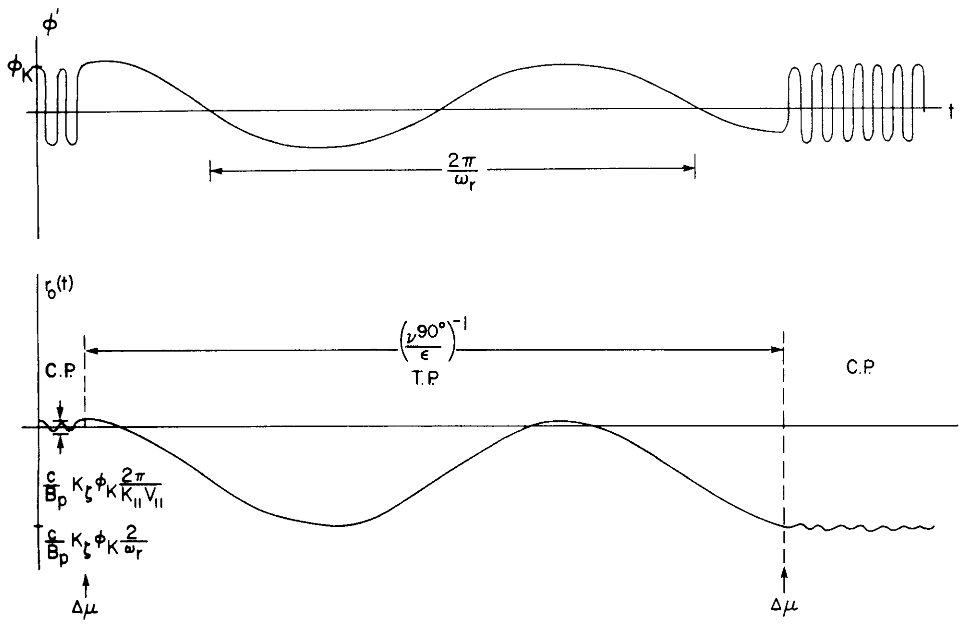

Fig. XII-17. Radial position of particle undergoing trapping and detrapping when $\frac{\nu^{90°}}{\epsilon} \ll \omega_r$.

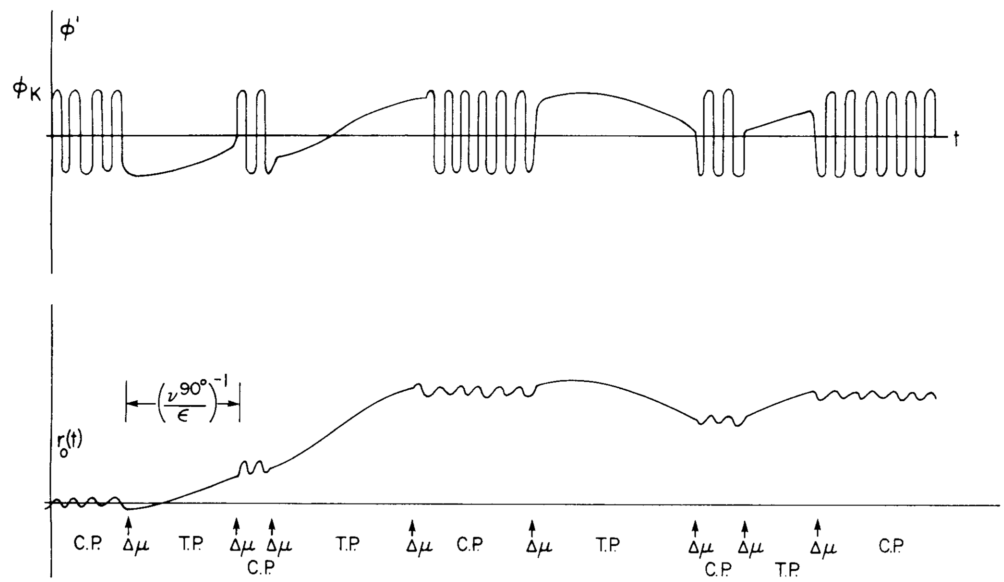

Fig. XII-18. Radial position of particles alternately trapped and circulating when $\frac{\nu^{90°}}{\epsilon} \gg \omega_r$.

From these formulas we write the quasi-linear diffusion coefficients:

$$D_{\mathscr{E}} = \frac{(\Delta\mathscr{E}_o)^2}{2\Delta t} = \begin{cases} \frac{1}{2}\sum_{\underline{K}} (e\phi_K)^2 \frac{\nu}{\epsilon}, & \frac{\nu}{\epsilon} \ll \omega_r \\ \frac{1}{2}\sum_{\underline{K}} (e\phi_K)^2 \frac{\omega_r^2}{\nu/\epsilon}, & \omega_r \ll \frac{\nu}{\epsilon} \end{cases} \tag{14}$$

$$D_r = \frac{(\Delta r_o)^2}{2\Delta t} = \begin{cases} \frac{1}{2}\sum_{\underline{K}} \left(\frac{cK_\zeta\phi_K}{B_p\omega_r}\right)^2 \frac{\nu}{\epsilon}, & \frac{\nu}{\epsilon} \ll \omega_r \\ \frac{1}{2}\sum_{\underline{K}} \left(\frac{cK_\zeta\phi_K}{B_p\omega_r}\right)^2 \frac{\omega_r^2}{\nu/\epsilon}, & \omega_r \ll \frac{\nu}{\epsilon} \end{cases} \tag{15}$$

These describe a global process of diffusion in that the average energy and radius ($\mathscr{E}_o$ and r_o) are diffusing because of the involved trapping-detrapping procedure.

As a check on the physics, we shall find the linear growth rate from the quasi-linear diffusion equation by equating the initial wave-energy gain with the particle kinetic-energy loss.

$$\frac{\partial}{\partial t}\sum_{\underline{K}} \omega \frac{\partial\epsilon}{\partial\omega} \frac{|E_K|^2}{8\pi} = -\frac{\partial}{\partial t}\sum_j \int d^3v\mathscr{E}f_{oj}. \tag{16}$$

The dissipative trapped ion mode is a positive energy wave with $\omega \frac{\partial\epsilon}{\partial\omega} = \frac{\sqrt{2\epsilon}}{K^2\lambda_D^2}\frac{\omega_*}{\omega_r}$. The right-hand side of Eq. 16 is evaluated with

$$\frac{\partial f_o}{\partial t} = \left\{C + D_{\mathscr{E}}\frac{\partial^2}{\partial\mathscr{E}^2} + 2D_{\mathscr{E}r}\frac{\partial^2}{\partial\mathscr{E}\partial r} + D_r\frac{\partial^2}{\partial r^2}\right\} f_o.$$

The equilibrium satisfies $Cf_o = 0$. Then, by changing variables from $\mathscr{E}, r$ to $\mathscr{E}, L_j$, where $L_j = r + \frac{\omega_{*j}}{\omega_r}\frac{r_n}{T}\mathscr{E}$, the diffusion equation reduces to

$$\frac{\partial f_o}{\partial t} = D_{\mathscr{E}}\frac{\partial^2 f_o}{\partial\mathscr{E}^2}.$$

By using a Maxwellian equilibrium with a density gradient, the integral in Eq. 16 is readily performed and we find

$$\sum_{\underline{K}} \frac{\sqrt{2\epsilon}\ ne^2}{T}\, \gamma \phi_{\underline{K}}^2 \frac{\omega_*}{\omega_r} \approx \sum_j \frac{3}{2} \sqrt{2\epsilon}\ nD_{\mathscr{E}j} \frac{-\omega_{*j}}{\omega_r} \frac{1}{T}.$$

For simplicity we assume $T_e = T_i$. Thus

$$\gamma^L = -\frac{3}{4} \frac{\nu_i}{\epsilon} + \frac{3}{4} \frac{\omega_r^2}{\nu_e/\epsilon}.$$

Except for the coefficient 3/4 this result is the same as Eq. 4, and it demonstrates that the frequency scaling of ion and electron contributions to γ^L differs because opposite limits of Eq. 14 apply for the two species.

We have qualitatively extended the quasi-linear theory to situations in which $\nabla T \neq 0$. The wave constrains particles to move along phase space paths with slopes (from Eqs. 12 and 13) $\frac{dr}{d\mathscr{E}} = \frac{cK_\zeta}{B_p \omega_r e_j} = \frac{-\omega_{*j}}{\omega_r} \frac{r_n}{T}$. These paths are plotted for the ion mode with $\frac{d \ln T}{d \ln n} \equiv \eta = -1$ in Fig. XII-19. Note when $T = T_o \exp(-r\eta/r_n) \neq$ constant the equal density contours are curved, so high- and low-energy particles may shift in different directions as they diffuse "downhill." To find the net change in the energy moment of a distribution we must account for the energy dependence of ν in the diffusion coefficients which weights different regions of phase space. Thus the $\frac{\nu}{\epsilon} \ll \omega_r$ limit of Eq. 14 is appropriate for ions and, since $\nu(\mathscr{E}) \propto \mathscr{E}^{-3/2}$, $D_{\mathscr{E}}$ is largest for low $\mathscr{E}$ ions. For electrons the

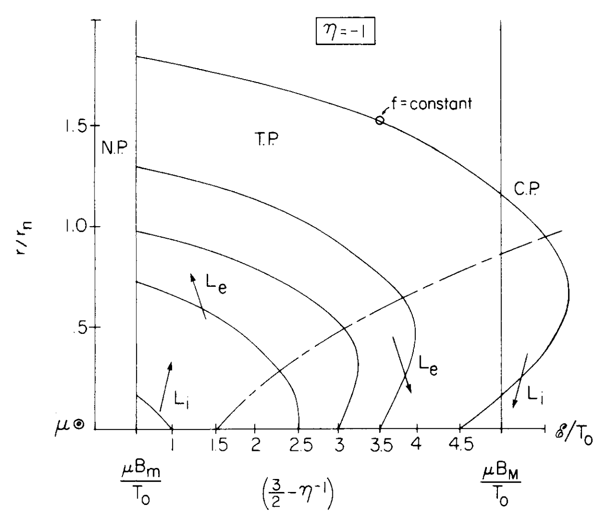

Fig. XII-19. Typical $f = n_o N_o \exp\left\{\left[\frac{3}{2}\eta - 1\right] \frac{r}{r_n} - \frac{\mathscr{E}}{T_o} e^{\eta r/r_n}\right\}$ with $\eta < 0$, showing ion and electron diffusion paths. Dashed curve: $\frac{r}{r_n} = \eta^{-1} \ln\left[\frac{1 - \frac{3}{2}\eta}{1 - \eta\mathscr{E}/T_o}\right]$.

$\omega_r \ll \nu/\epsilon$ limit is correct, and it is seen that $D_{\mathscr{E}}$ is largest for high $\mathscr{E}$ electrons. In Fig. XII-19 the low-energy ions and high-energy electrons both gain kinetic energy as they diffuse along their paths, so we conclude that for sufficiently negative η the instability will not grow.

Figure XII-20 is typical of a moderate positive η with the ions damping and the electrons driving wave growth. When η is sufficiently large and positive the dominant low-energy ions will lose energy as they diffuse along their phase space paths. This situation, depicted in Fig. XII-21, is due to the increased distortion of the constant f contours and shows that both species will drive wave growth.[4]

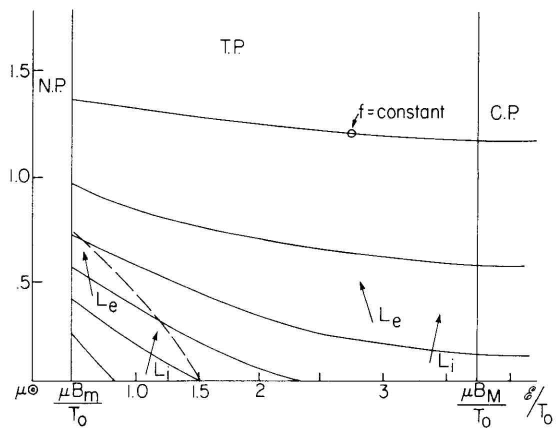

Fig. XII-20. Typical $f = n_o N_o \exp\left\{\left[\frac{3}{2}\eta - 1\right]\frac{r}{r_n} - \frac{\mathscr{E}}{T_o} e^{\eta r/r_n}\right\}$ when $0 < \eta < 2/3$.

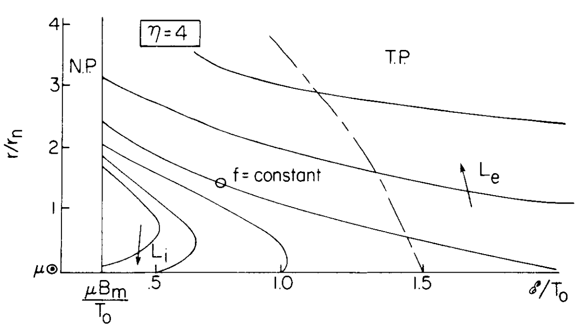

Fig. XII-21. Typical $f = n_o N_o \exp\left\{\left[\frac{3}{2}\eta - 1\right]\frac{r}{r_n} - \frac{\mathscr{E}}{T_o} e^{-\eta r/r_n}\right\}$ when $\frac{2}{3} < \eta$.

We have seen that a trapped particle remains correlated with the wave until it is collisionally detrapped. The secular energy change that it picks up is a function of the length of time it remained trapped and is independent of particle motion after the trapped portion of the orbit. Thus d_c is the frequency for collisional detrapping:

$$d_c \approx \frac{D_\mu}{(\mathscr{E}/B_m - \mathscr{E}/B_M)^2} \approx \frac{\nu}{\epsilon},$$

where we used an approximation of C to account for collisionally induced particle diffusion in μ, i.e., $C \approx D_\mu\, \partial^2/\partial\mu^2$ with $D_\mu = mV_\parallel^2\mu\, \nu/B$. Use of this d_c in Eq. 11 yields Eq. 4. We recognize that particles near the trapped-circulating boundary are likely to escape trapped space rather quickly, i.e., with a frequency $d_c(\mathscr{E},\mu) \approx D_\mu/(\mu-\mathscr{E}/B_M)^2$. With this "improved" version of d_c we find that the linear ion collisional damping is slightly increased (cf. Rosenbluth et al.[4]).

Nonlinear Theory

One evident nonlinear effect is the change of trapped particle energy from the wave's influence. Again we solve Eq. 7 for trapped particles but allow collisional changes in μ while they remain trapped. Then we find $\mathscr{E}$ has small secular changes and we can construct a coefficient $D_{\mathscr{E}}^T(\phi)$ that describes local energy diffusion of particles within trapped space. Consequently there is a frequency $D_{\mathscr{E}}^T(\phi)/(\mu B_M - \mu B_m)^2$ at which particles are detrapped (in energy!) by a combination of wave turbulence and collisions. Since the trapping-detrapping sequence is associated with the global process of wave-particle energy exchange, we identify this nonlinear detrapping frequency as a (parallel) decorrelation frequency $d_\parallel(\phi)$. As a check on the Fokker-Planck derivation of $D_{\mathscr{E}}^T$ we iterated Eq. 8 in the conventional quasi-linear fashion to obtain $D_{\mathscr{E}}^T$ in terms of an integral over the collisional orbits of particles that remain trapped. The two derivations yield similar results.

Substituting $d = d_c + d_\parallel(\phi)$ in Eq. 11, we observe that the nonlinear growth rate vanishes once

$$\frac{e\phi_{sat}}{T} \approx \frac{2\epsilon}{(RqK_\parallel)^2}. \qquad (17)$$

It is doubtful, however, that ϕ could ever reach such a large amplitude with $e\phi > \epsilon T \sim \mathscr{O}[\mu B_M - \mu B_m]$. This indicates a wave height greater than the magnetic well depth, and "trapped particles" would no longer exist as such.

Along the same lines of enhanced detrapping we analyzed the collisionless mechanism proposed by Jablon[5] to saturate our mode. It is found that the collisions plus turbulence rate $d_\parallel$ far exceeds Jablon's collisionless turbulent detrapping rate. In fact, collisionless nonlinear detrapping is also insignificant compared with the linear purely collisional frequency $d_c(\mathscr{E},\mu)$. We conclude that nonlinear detrapping is not the dominant saturation mechanism.

Next we consider the cross-field diffusion from $\underline{E} \times \underline{B}$ drifts. The two perpendicular coefficients were first derived by a Fokker-Planck treatment in which the bounce averaged radial velocity is a generalized Ware drift.[6] We point out that the same results are obtainable by iterating Eq. 8:

$$\begin{Bmatrix} D_r \\ D_b \end{Bmatrix} = \sum_{\underline{K}} \begin{Bmatrix} \left(\dfrac{cK_\zeta \phi_K}{B_p}\right)^2 \\ \left(\dfrac{cK_r \phi_K}{B}\right)^2 \end{Bmatrix} \frac{d + \gamma}{\omega_r^2 + (d+\gamma)^2}. \tag{18}$$

At saturation $\gamma \to 0$, and this expression is readily evaluated for electrons with $d_e \approx d_{ce} \gg \omega_r$. On the other hand, ions are collisionless; their dynamics is strongly controlled by the nonlinear cross-field diffusion with $d_{ci} \ll d_\perp$. Since two-dimensional collisionless diffusion theory is not yet well understood, we cannot evaluate Eq. 18 for ions directly. Instead we set $\begin{Bmatrix} D_{ri} \\ D_{bi} \end{Bmatrix} = \begin{Bmatrix} D_{re} \\ D_{be} \end{Bmatrix}$ from quasi-neutrality considerations. We also note that collisionless, two-dimensional $\underline{E} \times \underline{B}$ diffusion does not lead to wave-particle energy exchange, since $e\langle \underline{E}_\perp \times \underline{B} \cdot \underline{E}_\perp \rangle = 0$. The perpendicular diffusion is linked to a complicated mode-coupling process which damps mode growth nonlinearly by shuffling wave energy to spectral regions where various linear mechanisms remove wave energy. We surmise that the damping decrement may be simply related to spatial diffusion with $d_\perp = K_\perp^2 D_\perp$. Supporting evidence of this relationship is obtained by renormalizing the fluid equations.

When $d_\perp(\phi)$ is put in Eq. 11 we find that saturation occurs at

$$\frac{e\phi_{sat}}{T} \approx \frac{\sqrt{\epsilon}}{\overline{K}_r r_n}, \tag{19}$$

and the radial transport coefficient is

$$D_r \approx \frac{\overline{\gamma}_K^L}{2\overline{K}_r^2}. \tag{20}$$

Comparison with Eq. 17 shows that this mechanism saturates wave growth long before parallel decorrelation can become effective. The shortcoming of the theory is that our ignorance of spectral shape prevents a precise evaluation of Eqs. 19 and 20. (Bars over K_r and γ_K^L mean averages over the nonlinear spectrum.) If, as Kadomtsev and Pogutse suggest,[7] the spectrum has $K_b \approx K_r$, then D_r is nearly independent of $\underline{K}$ if γ_K^L

from Eq. 4 is used in Eq. 20. Note, however, $\gamma_K^L \neq \left(\frac{\sqrt{2\epsilon}}{2}\,\omega_*\right)^2 / (\nu_e/\epsilon) \propto K_b^2$ if large K_b modes are significant in the spectrum; in this case the $\frac{\nu_e}{\epsilon} \ll \frac{\sqrt{2\epsilon}}{2}\,\omega_*$ limit of Eqs. 11 and 18 applies. A detailed spectral analysis probably requires consideration of phase space clump formation.[8]

Several authors[9] have done one-dimensional mode-coupling calculations (neglecting radial mode numbers) for these modes. While mode coupling appears to be the important saturation mechanism, we question the applicability of such calculations to a truly two-dimensional nonlinear problem.

Another possibility that we dismiss is turbulent broadening of the circulating and trapped-particle Landau resonances contained in the $\mathcal{R}$ term of Eq. 11. As long as $(\omega_r/\omega^T)^3 \ll 1$ we find that no amount of broadening can ever saturate wave growth.

A time-scale analysis shows that collisions prevent a quasi-linear plateau from forming in energy. Consequently, quasi-linear diffusion is also not a dominant influence on saturation.

We conclude that cross-field diffusion is the principal nonlinear saturation mechanism. Eqs. 19 and 20 describe that saturated state, but we cannot predict details of the spectrum.

Our methods were applied to the dissipative trapped electron mode with similar results:

$$D_r \approx \frac{\left(1 + \frac{T_e}{T_i}\,\bar{b}_i\right)}{1 + \frac{T_e}{T_i}}\;\frac{\bar{\gamma}_K^L}{2\bar{K}_r^2}$$

$$\frac{e\phi_{sat}}{T} \approx \left[\frac{1 + \frac{T_e}{T_i}\,\bar{b}_i}{1 + \frac{T_e}{T_i}}\,\sqrt{2\epsilon}\,\{\eta + \bar{b}_i\}\right]^{1/2} \frac{1}{\bar{K}_r r_n}.$$

In the preceding discussion the following coordinates are used:

r-b-s

Orthogonal field line coordinates

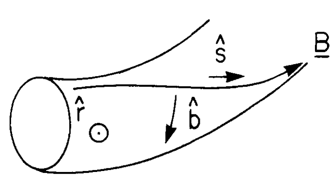

r-θ-ζ

Orthogonal toroidal coordinates

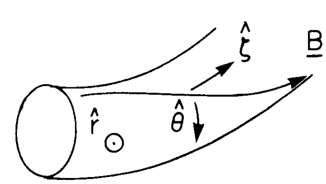

References

1. B. B. Kadomtsev and O. P. Pogutse, Zh. Eksp. Teor. Fiz. 51, 1734 (1966); Sov. Phys. – JETP 24, 1172 (1967).
2. R. D. Hazeltine, Plasma Physics 15, 77 (1973).
3. C. A. Primmerman, L. M. Lidsky, and P. A. Politzer, Phys. Rev. Letters 33, 957 (1974).
4. M. N. Rosenbluth, D. W. Ross, and D. P. Kostomarov, Nucl. Fusion 12, 3 (1972).
5. C. J. Jablon, Phys. Rev. Letters 28, 880 (1972).
6. A. A. Ware, Phys. Rev. Letters 25, 15 (1970).
7. B. B. Kadomtsev and O. P. Pogutse, in M. A. Leontovich (Ed.), Reviews of Plasma Physics, Vol. 5 (Consultants Bureau, New York, 1970), p. 261 ff.
8. T. H. Dupree, Phys. Fluids 15, 334 (1972).
9. R. E. LaQuey, S. M. Mahajan, P. H. Rutherford, and W. M. Tang, Phys. Rev. Letters 34, 391 (1975).

2. NONLINEAR ORBIT PERTURBATION AND ION HEATING

U. S. Energy Research and Development Administration (Contract E(11-1)-3070)

Charles F. F. Karney, Abraham Bers

Introduction

In proposed Tokamak RF heating schemes using waves near the lower hybrid frequency, fields with large $k_\perp a_i$ can be generated, either directly by linear conversion into lower hybrid waves or by the parametric decay into lower hybrid waves and ion Bernstein waves. The fields can significantly perturb the motion of an ion, and hence can nonlinearly heat the ions. In this report we present the results of a numerical solution of the orbit equation and give an approximate formula for the ion energy gain.

Basic Equations

We consider an ion in a uniform magnetic field $B_o\hat{z}$ and perpendicularly traveling electrostatic wave

$$E(\bar{r}, t) = \hat{y}E_o \cos(ky - \omega t + \phi). \tag{1}$$

The Lorentz force equation for this particle is

$$\frac{d\bar{v}}{dt} = \frac{q}{m}[\bar{v}\times \bar{B} + \bar{E}(\bar{r}, t)]$$

$$= \frac{q}{m}[\bar{v}\times B_o\hat{z} + \hat{y}E_o \cos(ky - \omega t + \phi)]. \tag{2}$$

If we normalize time to $1/\Omega$ ($\Omega = qB_o/m$), length to $1/k$, and velocity to Ω/k, then (2) becomes

$$\frac{d\bar{v}}{dt} = \bar{v} \times \hat{z} + \alpha\hat{y} \cos(y - \nu t + \phi), \tag{3}$$

where $\alpha = \frac{qE}{m} \frac{k}{\Omega^2}$, and $\nu = \omega/\Omega$. The x-component of (3) is

$$\ddot{x} = \dot{y} \tag{4}$$

and the y-component of (3) is

$$\ddot{y} + \dot{x} = \alpha \cos(y - \nu t + \phi). \tag{5}$$

We choose initial conditions such that the guiding center is initially at $x = y = 0$, i.e., at $t = 0$:

$$\dot{x} = r \cos\theta \qquad \dot{y} = r \sin\theta$$

$$x = -r \sin\theta \qquad y = r \cos\theta$$

Then (4) can be integrated to give

$$\dot{x} = y \tag{6}$$

and (5) may then be written

$$\ddot{y} + y = \alpha \cos(y - \nu t + \phi). \tag{7}$$

Solution of Equations

We solve (6) and (7) with a predictor-corrector method, which we start with the Taylor's series solution. In Fig. XII-22 we present the result for $\nu = 30$, $\alpha = 30$ with two different initial velocities. Note that in case (a) with the initial velocity $= 22\ \Omega/k$, the orbits are closed. The energy gain by the ion in this case is very nearly zero. If we increase the initial velocity to $24\ \Omega/k$, we see a very different behavior. When the particle is traveling in the y direction, it is trapped momentarily by the wave with which it exchanges a significant amount of energy, which causes the ion orbit to open. Remembering that without a magnetic field the trapping condition for a particle is

$$\left| \frac{\omega}{k} - v_y \right| < v_{tr}, \tag{8}$$

where v_{tr} is the trapping width $(qE/mk)^{1/2}$. We guess from Fig. XII-22 that the condition for trapping in the presence of a magnetic field is that at some point during the cyclotron orbit (8) is satisfied. We can then write the trapping condition as

$$v_o > \frac{\omega}{k} - v_{tr} \equiv v_{thresh}, \tag{9}$$

where v_o is the initial perpendicular velocity of the ion. With the parameters of Fig. XII-22, Eq. 9 predicts a threshold of 24.4 Ω/k for v_{thresh}, which is close to the threshold observed in Fig. XII-22.

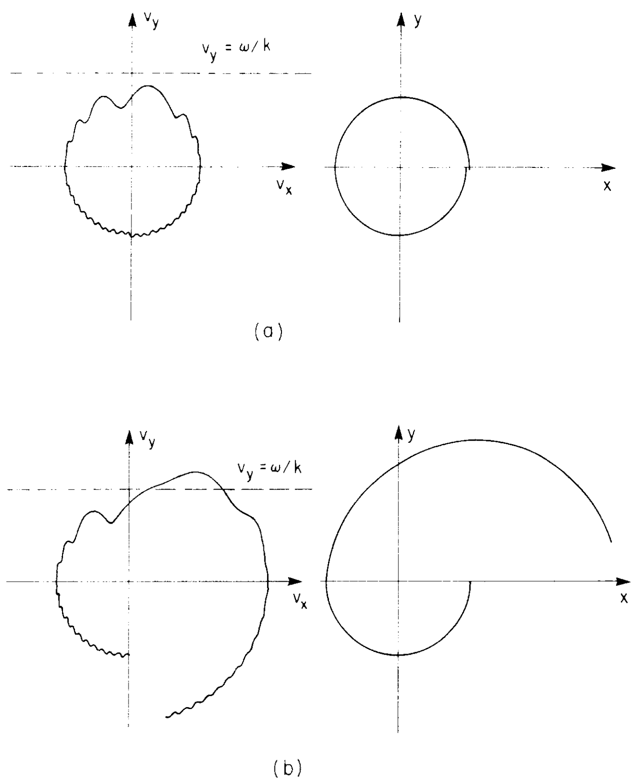

Fig. XII-22. Ion orbits with $\omega = 30\ \Omega$ and $\alpha = 30$.
(a) $v_o = 22\ \Omega/k$.
(b) $v_o = 24\ \Omega/k$.

a. Energy Gained by the Ions

Equation 9 is the condition under which the particle exchanges some energy with the wave. We have yet to determine how much it gains. By solving the differential equations with constant ω and E but different values of v_o and ϕ (the electric field phase) we can generate a plot of $\langle \Delta\mathscr{E} \rangle$, the phase average energy gain per particle per cyclotron period, against v_o. Such a plot is shown in Fig. XII-23. We notice a sharp threshold to the energy gain close to v_{thresh}. The curve peaks close to the threshold and drops off at higher velocities. Since the maximum occurs close to the threshold it suggests that the value of the maximum is given by

$$\langle\Delta\mathscr{E}\rangle_{max} = \frac{1}{2} m\left[\left(\frac{\omega}{k}+v_{tr}\right)^2 - \left(\frac{\omega}{k}-v_{tr}\right)^2\right]$$

$$= 2\, m \frac{\omega}{k} v_{tr}. \tag{10}$$

This just says that a particle that is just trapped will bounce once in the potential well of the field and come out with velocity $(\omega/k+v_{tr})$. Using (10), we find $\langle\Delta\mathscr{E}\rangle_{max} = 330\ m\Omega^2/k^2$

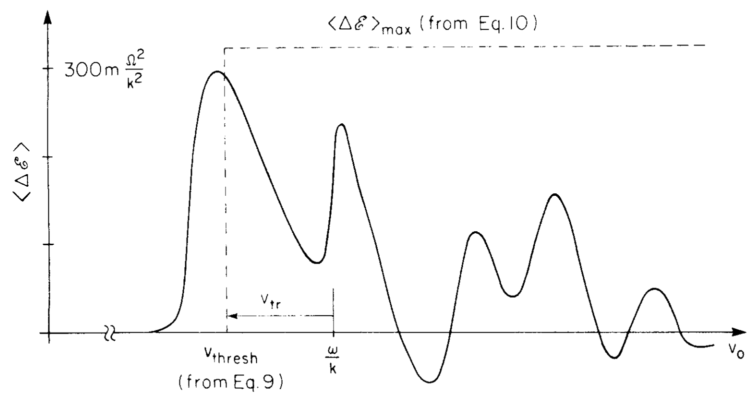

Fig. XII-23. Plot of average energy gain per ion per cyclotron period vs ion velocity for $\omega = 30\ \Omega$ and $\alpha = 30$.

for the parameters of Fig. XII-23. This agrees well with the observed value of approximately $300\ m\Omega^2/k^2$.

We wish to find the energy gain by a perpendicular distribution function f(v) of ions. We integrate $\langle\Delta\mathscr{E}\rangle$ over the distribution functions thus

$$\langle\Delta\mathscr{E}\rangle_{tot} = n_o \int_0^\infty 2\pi v f(v) \langle\Delta\mathscr{E}\rangle\, dv. \tag{11}$$

We substitute a Maxwellian for f, so that

$$f = \frac{1}{2\pi v_T^2} \exp\left(-v^2/2v_T^2\right). \tag{12}$$

Since in (11) we integrate over an exponential function, the main contribution to the integral comes from near $v = v_{thresh}$. Thus we approximate the function $\langle\Delta\mathscr{E}\rangle$ by a function that is zero for $v < v_{thresh}$ and equals $\langle\Delta\mathscr{E}\rangle_{max}$ for $v > v_{thresh}$ (shown as a dashed line in Fig. XII-23). Performing the integral in (11), we obtain

$$\langle\Delta\mathscr{E}\rangle_{tot} = n_o \langle\Delta\mathscr{E}\rangle_{max} \exp\left(-v_{thresh}^2/2v_T^2\right). \tag{13}$$

Naturally, the strongest dependence in (13) appears in the exponential, so we predict a large $\langle \Delta\mathscr{E} \rangle_{tot}$ if $v_{thresh} \sim v_T$, or from (9)

$$k_\perp a_i = \frac{\omega}{\Omega} - \left(\frac{eE}{m}\frac{k}{\Omega^2}\right)^{1/2}. \tag{14}$$

As an example of the strength of this interaction consider a large-amplitude Bernstein decay wave with $E_o = 10^4$ V/cm, $\omega = 10\,\Omega$, $k_\perp a_i = 10$ and $n_o = 10^{14}/\text{cm}^3$, T_i = 1 keV and B_o = 50 kG. Evaluating (13), we find that $\langle \Delta\mathscr{E} \rangle_{tot}/n_o T = 0.25$, whereas $\frac{1}{4}\epsilon_o E_o^2/n_o T_i = 10^{-4}$. Clearly the wave is very strongly nonlinearly damped.

3. THREE-DIMENSIONAL EFFECTS IN THE NONLINEAR FILAMENTATION OF LOWER HYBRID CONES

U.S. Energy Research and Development Administration (Contract E(11-1)-3070)

George L. Johnston, Charles F. F. Karney, Flora Y. F. Chu, Abraham Bers

Introduction

In a recent experiment in which large-amplitude lower hybrid oscillations were excited in a plasma Gekelman and Stenzel[1] observed that intense localized electric fields and associated density cavities were formed along the resonance cones in regions of the plasma far from the lower hybrid layer. Morales and Lee[2] have developed a theoretical model of the nonlinear self-distortion of the propagation of large-amplitude lower hybrid waves to explain this experiment. They assume that the electric field in the plasma has components in the direction of the magnetic field and in a single direction transverse to it. This two-dimensional assumption excludes other ponderomotive force effects that are generally considered to be dominant in parametric instabilities near the lower hybrid frequency.[3]

We have begun to develop a three-dimensional model of the nonlinear filamentation of lower hybrid cones in order to understand the significance of these additional ponderomotive force effects. We shall not limit our investigation to self-modulation of the externally driven field, but shall include possible coupling to waves in the plasma that have frequencies very close to that of the externally driven field. We have determined the dominant elements of the ponderomotive force density in a cold-fluid model under the assumption that the frequency of the externally excited wave satisfies the conditions $\Omega_i \ll \omega \ll \Omega_e$ and $\omega \approx \omega_{pi}$, and under two sets of assumptions regarding the relative magnitudes of different components of the electric field in the plasma. In Case 1, which corresponds to self-distortion of a wave launched by a single or split waveguide, we assume that $|E_y| \approx |E_z| \approx (m_e/m_i)^{1/2} |E_x|$. In Case 2, which corresponds to self-distortion of a wave launched by an array of waveguides extended in the θ direction or to the interaction of a wave launched by a single or split waveguide with lower hybrid waves in the plasma, we assume that $|E_x| \approx |E_y| \approx (m_i/m_e)^{1/2} |E_z|$. We have also obtained the low-frequency particle density modulation induced by the ponderomotive force density in a warm-fluid model under the assumptions of quasi-neutrality and extremely low frequency.

Ponderomotive Force Density

The ponderomotive force density of species α is

$$\underline{F}_{\alpha L} = -n_o m_\alpha (\underline{u}_\alpha \cdot \nabla \underline{u}_\alpha)_L. \tag{1}$$

Here $\underline{u}_\alpha$ is the linear fluid velocity perturbation of species α driven by the high-frequency electric field. The unperturbed species number density is n_o, the mass of species α is m_α, and subscript L denotes the low-frequency component of the bilinear combination. We introduce the complex representation

$$\underline{u}_\alpha = \underline{\tilde{u}}_\alpha(\underline{r}, t) \exp(-i\omega t) + \text{c. c.}, \tag{2}$$

where the time-harmonic composition of $\underline{\tilde{u}}_\alpha(\underline{r}, t)$ is very small compared with ω. The complex amplitude $\underline{\tilde{u}}_\alpha(\underline{r}, t)$ is expressed in terms of the cold-fluid susceptibility by

$$\underline{\tilde{u}}_\alpha(\underline{r}, t) = \frac{\omega}{4\pi n_o q_\alpha i} \underset{\approx}{\chi}^\alpha \cdot \underline{\tilde{E}}(\underline{r}, t). \tag{3}$$

The susceptibility is evaluated at frequency ω. We express the electric field in terms of the electrostatic potential

$$\phi(\underline{r}, t) = \tilde{\phi}(\underline{r}, t) \exp(-i\omega t) + \text{c. c.} \tag{4}$$

The bilinear combination of fluid velocity perturbations which we retain to determine the low-frequency component is

$$(\underline{u}_\alpha \cdot \nabla \underline{u}_\alpha)_L = \underline{\tilde{u}}_\alpha \cdot \nabla \underline{\tilde{u}}_\alpha^* + \text{c. c.}, \tag{5}$$

where

$$\underline{\tilde{u}}_\alpha \cdot \nabla = \frac{-\omega}{4\pi n_o q_\alpha i} \left[\left(\chi_{xx}^\alpha \partial_x \tilde{\phi} + \chi_{xy}^\alpha \partial_y \tilde{\phi}\right) \partial_x + \left(\chi_{yx}^\alpha \partial_x \tilde{\phi} + \chi_{yy}^\alpha \partial_y \tilde{\phi}\right) \partial_y + \left(\chi_{zz}^\alpha \partial_z \tilde{\phi}\right) \partial_z\right] \tag{6}$$

and

$$\underline{\tilde{u}}_\alpha^* = \frac{-\omega i}{4\pi n_o q_\alpha} \left[\hat{i}\left(\chi_{xx}^{\alpha *} \partial_x \tilde{\phi}^* + \chi_{xy}^{\alpha *} \partial_y \tilde{\phi}^*\right) + \hat{j}\left(\chi_{yx}^{\alpha *} \partial_x \tilde{\phi}^* + \chi_{yy}^{\alpha *} \partial_y \tilde{\phi}^*\right) + \hat{k} \chi_{zz}^{\alpha *} \partial_z \tilde{\phi}^*\right]. \tag{7}$$

The approximate forms of the nonvanishing elements of the susceptibility tensor in the case $\Omega_i \ll \omega \ll \Omega_e$ and their orders under the additional assumption that $\omega \approx \omega_{pi}$ are

$$\chi_{xx}^e = \chi_{yy}^e = \frac{\omega_{pe}^2}{\Omega_e^2} = O\left(\omega_{pe}^2/\Omega_e^2\right)$$

$$\chi_{xy}^e = -\chi_{yx}^e = -i\,\frac{\omega_{pe}^2}{\omega\Omega_e} = O\left[(m_i/m_e)^{1/2}(\omega_{pe}/\Omega_e)\right]$$

$$\chi_{zz}^e = -\frac{\omega_{pe}^2}{\omega^2} = O\,(m_i/m_e)$$

$$\chi_{xx}^i = \chi_{yy}^i = -\frac{\omega_{pi}^2}{\omega^2} = O\,(1)$$

$$\chi_{xy}^i = -\chi_{yx}^i = -i\,\frac{\Omega_i\omega_{pi}^2}{\omega^3} = O\,(\Omega_i/\omega_{pi})$$

$$\chi_{zz}^i = -\frac{\omega_{pi}^2}{\omega^2} = O\,(1).$$

We note that for the conditions of interest values of the quantity ω_{pe}/Ω_e lie between 0.5 and unity and values of the quantity ω_{pi}/Ω_i lie between 20 and 40.

We order the partial derivatives as follows:

Case 1. $\partial_x = O\,(1);\ \ \partial_y = \partial_z = O\left[(m_e/m_i)^{1/2}\right].$

Case 2. $\partial_x = \partial_y = O\,(1);\ \ \partial_z = O\left[(m_e/m_i)^{1/2}\right].$

The basis for these orderings is the following. In a uniform plasma, the y- and z-components of the spatial-harmonic composition of the linear propagation are determined by the launching structure. If its dimensions in the y and z directions are comparable, as is the case for single or split waveguides, the range of the k_y is comparable to the range of the k_z, and thus it is appropriate to assume that $|E_y| \approx |E_z|$. The dielectric properties of the plasma determine the ratio of $|E_z|$ to $|E_\perp|$.

If the launching structure is composed of an array of waveguides extended in the

θ direction, the range of the k_θ and the range of the k_r may become comparable to each other within some region of the plasma. There it would be appropriate in a resolution of the field into a local Cartesian coordinate system to assume that $|E_x| \approx |E_y|$. Alternatively, if we wish to consider the nonlinear interaction of the externally excited wave with lower hybrid waves in the plasma, we do not want to be restricted by the ordering of Case 1. In the absence of more specific information about the relative magnitudes of different components of the electric field in the plasma, it is appropriate to assume that the two components transverse to the magnetic field are of comparable magnitude. In either of these cases, we realize the ordering of Case 2.

To obtain the dominant terms in the ponderomotive force density, we determine the bilinear combination of dominant terms in the operator $\tilde{\underline{u}}_\alpha \cdot \nabla$ and the vector $\tilde{\underline{u}}_\alpha^*$, noting that ordering is not possible among different components of the vector $\tilde{\underline{u}}_\alpha \cdot \nabla\tilde{\underline{u}}_\alpha^*$. We shall show that in the limit of very low frequencies the z-component of the ponderomotive force density is dominant in determining the low-frequency particle density modulation. Accordingly, the z-component of the ponderomotive force density is of particular interest.

We consider first the electron ponderomotive force density. Its z-component is given by

$$F_{eLz} = -\frac{1}{4\pi}\frac{\omega^2}{\omega_{pe}^2}\left(\tilde{D}_e\tilde{S}_{ez}^* + \text{c. c.}\right), \tag{8}$$

where

$$\tilde{D}_e = (\underset{\approx}{\chi}^e \cdot \nabla\tilde{\phi}) \cdot \nabla \tag{9}$$

and $\tilde{S}_{ez}^*$ is the z-component of the vector

$$\tilde{\underline{S}}_e^* = \underset{\approx}{\chi}^{e*} \cdot \nabla\tilde{\phi}^*. \tag{10}$$

Table XII-1 exhibits the results of the ordering for Case 1. Part (a) contains all information necessary to determine the order of F_{eLz}. Part (b) contains the results of the ordering of $\tilde{\underline{S}}_e^*$. The principal result in Case 1 is that the terms of $\tilde{D}_e$ containing χ_{xy}^e and χ_{yx}^e, which are absent from the two-dimensional treatment, are of the same order as the largest terms in the two-dimensional treatment.

In similar fashion, Table XII-2 exhibits the results of the ordering for Case 2. Here the principal result is that the terms of $\tilde{D}_e$ that contain χ_{xy}^e and χ_{yx}^e are between one and two orders of magnitude larger than the largest terms in the two-dimensional treatment.

The z-component of electron ponderomotive force density, including these terms, is

Table XII-1. Ordering for Case 1.

(a) Constituents of F_{eLz}		
$\tilde{D}_e = (\underset{\approx}{\chi}^e \cdot \nabla\tilde{\phi}) \cdot \nabla$	$\chi_{ij}^e \approx$	Order of Term
$= \left[\left(\chi_{xx}^e \partial_x \tilde{\phi}\right) \partial_x\right.$	$\frac{\omega_{pe}^2}{\Omega_e^2}$	$\frac{1}{4}$ - 1
$+ \left(\chi_{xy}^e \partial_y \tilde{\phi}\right) \partial_x$	$-i \frac{\omega_{pe}^2}{\omega\Omega_e}$	$\frac{\omega_{pe}}{\Omega_e} \sim \left(\frac{1}{2} - 1\right)$
$+ \left(\chi_{yx}^e \partial_x \tilde{\phi}\right) \partial_y$	$i \frac{\omega_{pe}^2}{\omega\Omega_e}$	$\frac{\omega_{pe}}{\Omega_e} \sim \left(\frac{1}{2} - 1\right)$
$+ \left(\chi_{yy}^e \partial_y \tilde{\phi}\right) \partial_y$	$\frac{\omega_{pe}^2}{\Omega_e^2}$	$\frac{m_e}{m_i} \frac{\omega_{pe}^2}{\Omega_e^2} \ll 1$
$\left.+ \left(\chi_{zz}^e \partial_z \tilde{\phi}\right) \partial_z\right]$	$-\frac{\omega_{pe}^2}{\omega^2}$	1
$\tilde{S}_{ez}^* = \hat{z} \cdot \underset{\approx}{\chi}^{e*} \cdot \nabla\tilde{\phi}^*$		
$= \left(\chi_{zz}^{e*} \partial_z \tilde{\phi}^*\right)$	$-\frac{\omega_{pe}^2}{\omega^2}$	$\left(\frac{m_i}{m_e}\right)^{1/2} \sim 40$

(b) Components of $\underline{\tilde{S}}_e^*$		
$\underline{\tilde{S}}_e^* = \underset{\approx}{\chi}^{e*} \cdot \nabla\tilde{\phi}^*$	$\chi_{ij}^{e*} \approx$	Order of Term
$= \left[\hat{x}\left(\chi_{xx}^{e*} \partial_x \tilde{\phi}^*\right.\right.$	$\frac{\omega_{pe}^2}{\Omega_e^2}$	$\frac{1}{4}$ - 1
$\left.+ \chi_{xy}^{e*} \partial_y \tilde{\phi}^*\right)$	$i \frac{\omega_{pe}^2}{\omega\Omega_e}$	$\frac{\omega_{pe}}{\Omega_e} \sim \left(\frac{1}{2} - 1\right)$
$+ \hat{y}\left(\chi_{yx}^{e*} \partial_x \tilde{\phi}^*\right.$	$-i \frac{\omega_{pe}^2}{\omega\Omega_e}$	$\left(\frac{m_i}{m_e}\right)^{1/2} \frac{\omega_{pe}}{\Omega_e} \sim (20-40)$
$\left.+ \chi_{yy}^{e*} \partial_y \tilde{\phi}^*\right)$	$\frac{\omega_{pe}^2}{\Omega_e^2}$	$\left(\frac{m_e}{m_i}\right)^{1/2} \frac{\omega_{pe}^2}{\Omega_e^2} \ll 1$
$\left.+ \hat{z}\left(\chi_{zz}^{e*} \partial_z \tilde{\phi}^*\right)\right]$	$-\frac{\omega_{pe}^2}{\omega^2}$	$\left(\frac{m_i}{m_e}\right)^{1/2} \sim 40$

Table XII-2. Ordering for Case 2.

(a) Constituents of F_{eLz}		
$\tilde{D}_e = (\underset{\approx}{\chi}^e \cdot \nabla\tilde{\phi}) \cdot \nabla$	$\chi_{ij}^e \approx$	Order of Term
$= \left[\left(\chi_{xx}^e \partial_x \tilde{\phi}\right) \partial_x\right.$	$\dfrac{\omega_{pe}^2}{\Omega_e^2}$	$\frac{1}{4}$ - 1
$+ \left(\chi_{xy}^e \partial_y \tilde{\phi}\right) \partial_x$	$-i\,\dfrac{\omega_{pe}^2}{\omega\Omega_e}$	$\left(\dfrac{m_i}{m_e}\right)^{1/2} \dfrac{\omega_e}{\Omega_e} \sim (20\text{-}40)$
$+ \left(\chi_{yx}^e \partial_x \tilde{\phi}\right) \partial_y$	$i\,\dfrac{\omega_{pe}^2}{\omega\Omega_e}$	$\left(\dfrac{m_i}{m_e}\right)^{1/2} \dfrac{\omega_e}{\Omega_e} \sim (20\text{-}40)$
$+ \left(\chi_{yy}^e \partial_y \tilde{\phi}\right) \partial_y$	$\dfrac{\omega_{pe}^2}{\Omega_e^2}$	$\frac{1}{4}$ - 1
$\left.+ \left(\chi_{zz}^e \partial_z \tilde{\phi}\right) \partial_z\right]$	$-\dfrac{\omega_{pe}^2}{\omega^2}$	1
$\tilde{S}_{ez}^* = \hat{z} \cdot \underset{\approx}{\chi}^{e*} \cdot \nabla\tilde{\phi}^*$		
$= \left(\chi_{zz}^{e*} \partial_z \tilde{\phi}^*\right)$	$-\dfrac{\omega_{pe}^2}{\omega^2}$	$\left(\dfrac{m_i}{m_e}\right)^{1/2} \sim 40$
(b) Components of $\underline{\tilde{S}}_e^*$		
$\underline{\tilde{S}}_e^* = \underset{\approx}{\chi}^{e*} \cdot \nabla\tilde{\phi}^*$	$\chi_{ij}^{e*} \approx$	Order of Term
$= \left[\hat{x}\left(\chi_{xx}^{e*} \partial_x \tilde{\phi}^*\right.\right.$	$\dfrac{\omega_{pe}^2}{\Omega_e^2}$	$\frac{1}{4}$ - 1
$\left.+ \chi_{xy}^{e*} \partial_y \tilde{\phi}^*\right)$	$i\,\dfrac{\omega_{pe}^2}{\omega\Omega_e}$	$\left(\dfrac{m_i}{m_e}\right)^{1/2} \dfrac{\omega_{pe}}{\Omega_e} \sim (20\text{-}40)$
$+ \hat{y}\left(\chi_{yx}^{e*} \partial_x \tilde{\phi}^*\right.$	$-i\,\dfrac{\omega_{pe}^2}{\omega\Omega_e}$	$\left(\dfrac{m_i}{m_e}\right)^{1/2} \dfrac{\omega_{pe}}{\Omega_e} \sim (20\text{-}40)$
$\left.+ \chi_{xy}^{e*} \partial_y \tilde{\phi}^*\right)$	$\dfrac{\omega_{pe}^2}{\Omega_e^2}$	$\frac{1}{4}$ - 1
$\left.+ \hat{z}\left(\chi_{zz}^{e*} \partial_z \tilde{\phi}^*\right)\right]$	$-\dfrac{\omega_{pe}^2}{\omega^2}$	$\left(\dfrac{m_i}{m_e}\right)^{1/2} \sim 40$

$$F_{eLz} = -\frac{1}{4\pi}\partial_z\left\{-\frac{\omega_{pe}^2}{\Omega_e^2}\left[(|\partial_x\tilde{\phi}|)^2+(|\partial_y\tilde{\phi}|)^2\right]+\frac{\omega_{pe}^2}{\omega^2}(|\partial_z\tilde{\phi}|)^2+i\frac{\omega_{pe}^2}{\omega\Omega_e}\left[(\partial_y\tilde{\phi})(\partial_x\tilde{\phi}^*)-(\partial_y\tilde{\phi}^*)(\partial_x\tilde{\phi})\right]\right\}. \tag{11}$$

The last two terms are the significant additional terms introduced by the three-dimensional treatment. We note that these terms are very different physically from those arising from a two-dimensional treatment. They have their origin in an $\underline{E} \times \underline{B}$ force, which is generally considered dominant in parametric instabilities near the lower hybrid frequency.[3] The ordering of Case 1 diminishes their importance, with the result that they are reduced to the same order as the terms appearing in the two-dimensional treatment. The ordering of Case 2 maintains them in a dominant role.

The sum of the first two terms in Eq. 11 is of order $(\omega_{pe}/\Omega_e)^2 (m_e/m_i)^{1/2}$. The third term is of order $(m_e/m_i)^{1/2}$. In Case 1 the last two terms are of order $(\omega_{pe}/\Omega_e)(m_e/m_i)^{1/2}$. In Case 2 they are of order (ω_{pe}/Ω_e).

A further matter must be considered with regard to these terms. In order to obtain an analytic formulation of the filamentation problem, Morales and Lee treat ponderomotive and thermal effects as small corrections to linear propagation. They assume that the complex amplitude of the linearized potential is a function of (x-cz). If a three-dimensional generalization of such a linearized potential,

$$\phi(\underline{r}, t) = \tilde{\phi}(\xi x+\eta y-cz)\exp(-i\omega t) + \text{c. c.}, \tag{12}$$

is substituted in the three-dimensional version of F_{eLz} (Eq. 11), the sum of the significant additional terms introduced by the three-dimensional treatment vanishes.

The assumption of a linearized potential of the form of Eq. 12 is inconsistent with propagation from a localized source. In a plane x = constant, the existence of contours of constant $\tilde{\phi}$ on the straight lines $\eta y - cz$ = constant is inconsistent with the intersection of the plane by a finite propagation cone.

In determining the ion ponderomotive force density we may assume that the ions are effectively unmagnetized. The order of the ion ponderomotive force density may be obtained directly from the expression

$$\underline{F}_{iL} = -\frac{1}{4\pi}\frac{\omega_{pi}^2}{\omega^2}\nabla(|\nabla\tilde{\phi}|^2). \tag{13}$$

In Cases 1 and 2 F_{iLz} is of order $(m_e/m_i)^{1/2}$.

Low-Frequency Particle Density Modulation

The particle density modulation in the plasma which is induced by the ponderomotive force density is determined from the low-frequency component of the warm-fluid equations. We make the usual assumption of quasi-neutrality and assume further that the time-harmonic spectral composition of the low-frequency response is very small compared with the electron and ion gyro frequencies.

From the low-frequency component of the Fourier transforms in time of the linearized species continuity equations and equations of motion we obtain the relation

$$-\omega_L^2 \hat{n}_{\alpha L} - \frac{i\omega_L n_o}{\left(\omega_L^2 - \Omega_\alpha^2\right)} \left[\frac{\partial}{\partial x} (i\omega_L \hat{a}_{\alpha Lx} - \epsilon_\alpha \Omega_\alpha \hat{a}_{\alpha Ly}) + \frac{\partial}{\partial y} (\epsilon_\alpha \Omega_\alpha \hat{a}_{\alpha Lx} + i\omega_L \hat{a}_{\alpha Ly})\right] + n_o \frac{\partial}{\partial z} \hat{a}_{\alpha Lz} = 0 \tag{14}$$

in which

$$\hat{\underline{a}}_{\alpha L} = \frac{q_\alpha}{m_\alpha} \hat{\underline{E}}_L - \frac{\gamma_\alpha T_\alpha}{n_o m_\alpha} \nabla \hat{n}_{\alpha L} - \widehat{(\underline{u}_\alpha \cdot \nabla \underline{u}_\alpha)}_L. \tag{15}$$

In these equations ω_L is the Fourier transform variable, the hatted quantities denote Fourier transforms, and ϵ_α is the sign of q_α. To lowest order in the small parameters ω_L/Ω_α, only the last term of Eq. 15 is present. We invert the Fourier transforms, introduce the assumption of quasi-neutrality, $n_{eL} = n_{iL} = n_L$, multiply the resulting equation for each species by $n_o m_\alpha$, and sum over species. We obtain thereby the differential equation for n_L in terms of the species ponderomotive force densities:

$$(\gamma_e T_e + \gamma_i T_i) \frac{\partial n_L}{\partial z} = F_{eLz} + F_{iLz}. \tag{16}$$

As we see from Eqs. 11 and 13, the z-component of the species ponderomotive force densities can be expressed as partial derivatives with respect to z of functions of spatial variables. Therefore an explicit expression for the low-frequency particle density modulation can be obtained by integration.

We are now continuing to investigate the role of three-dimensional effects in the self-distortion of the externally driven field and in its possible coupling to waves in the plasma which have frequencies very close to it.

References

1. W. Gekelman and R. L. Stenzel, Report PPG-227, Plasma Physics Group, University of California Los Angeles, 1975.
2. G. J. Morales and Y. C. Lee, Phys. Rev. Letters <u>35</u>, 930 (1975).
3. M. Porkolab, Report MATT-1069, Plasma Physics Laboratory, Princeton University, Princeton, New Jersey, October 1974.

4. SOLUTION TO BOUNDARY VALUE PROBLEM FOR PROPAGATION OF LOWER HYBRID WAVES

U. S. Energy Research and Development Administration (Contract E(11-1)-3070)

Charles F. F. Karney, Flora Y. F. Chu, George L. Johnston, Abraham Bers

Recently Morales and Lee[1] derived the modified Korteweg-de Vries (mKdV) equation as describing the two-dimensional steady-state propagation of lower hybrid waves in a homogeneous plasma without considering the boundary-value problem of exciting such waves. In addition, in order to obtain the mKdV equation it was necessary to make the restrictive assumption that the coefficient of the amplitude of the time-harmonic component of the potential at frequency ω is real. This invalidates the applicability of the mKdV equation to the problem of lower hybrid wave energy flow from an external source.

Further consideration of the mKdV equation may nevertheless provide some additional insight into the problem of excitation by a source. Accordingly, we present a solution of a boundary-value problem of the mKdV equation. We find that if the source field has no $k = 0$ component the solitons of the mKdV equation always occur in interacting pairs called breathers.

Derivation of the Modified Korteweg-de Vries Equation

We shall now give the main steps of this derivation. We consider lower hybrid fields given by the potential Re $[\phi(x,z)\, e^{-i\omega t}]$, where ω satisfies $\Omega_i \ll \omega \ll \Omega_e$ and z is the direction of $\overline{B}_o$. We shall later introduce the assumption that $\phi(x, z)$ is real. We assume that the plasma is homogeneous and that the magnetic field is uniform. We write the linear dispersion relation for these waves, including thermal effects to lowest order,

$$\frac{\partial}{\partial x} K_\perp \frac{\partial}{\partial x} \phi + \frac{\partial}{\partial z} K_\parallel \frac{\partial}{\partial z} \phi + a \frac{\partial^4}{\partial x^4} \phi + b \frac{\partial^4}{\partial x^2 \partial z^2} \phi + c \frac{\partial^4}{\partial z^4} \phi = 0, \tag{1}$$

where

$$K_\perp = 1 + \frac{\omega_{pe}^2}{\Omega_e^2} - \frac{\omega_{pi}^2}{\omega^2} \qquad K_\parallel = 1 - \frac{\omega_{pi}^2}{\omega^2} - \frac{\omega_{pe}^2}{\omega^2} \tag{2}$$

and

$$a = \frac{1}{4} \frac{\omega_{pe}^2}{\Omega_e^2} \frac{v_{Te}^2}{\Omega_e^2} + \frac{\omega_{pi}^2}{\omega^2} \frac{v_{Ti}^2}{\omega^2} \tag{3a}$$

$$b = -\frac{1}{3} \frac{\omega_{pe}^2}{\omega^2} \frac{v_{Te}^2}{\Omega_e^2} + 2 \frac{\omega_{pi}^2}{\omega^2} \frac{v_{Ti}^2}{\omega^2} \tag{3b}$$

$$c = \frac{\omega_{pe}^2}{\omega^2}\frac{v_{Te}^2}{\omega^2} + \frac{\omega_{pi}^2}{\omega^2}\frac{v_{Ti}^2}{\omega^2} \tag{3c}$$

$$v_{Ts}^2 = 3T_s/m_s.$$

The coefficients a, b, and c are found by expanding the Harris dispersion relation. Morales and Lee derived these coefficients with the use of the fluid equations and thereby missed the $(\partial^4/\partial x^2\partial z^2)\phi$ term. As we shall see, the form of the final equation is unchanged by the inclusion of this term. Note that we have commuted the derivative operators with a, b, and c. This is admissible because we are considering a homogeneous plasma, so the variations in a, b, and c can only be due to nonlinear effects. These variations can be ignored because we are treating the thermal terms as corrections to the cold terms.

We proceed by calculating the ponderomotive force density at zero frequency arising from fields at ω. We calculate from that the density fluctuations at zero frequency. These density fluctuations are then inserted in (1) via ω_{pe} and ω_{pi} in $K_\parallel$ and $K_\perp$ to give us our nonlinear equation. The nonlinear interaction described here is the same as the nonoscillatory instability.

The pondermotive force density for species s is $\bar{F}_s = -n_s m \bar{v}_s \cdot \nabla \bar{v}_s$. Since the ions and electrons may be taken as infinitely magnetized at zero frequency, we need only the z-components of $\bar{F}_s$. Evaluating these components using the cold-fluid equations and assuming $\Omega_i \ll \omega \ll \Omega_e$, we obtain

$$F_{ez}(x,z) = -\frac{\epsilon_o}{4}\frac{\partial}{\partial z}\left[-\frac{\omega_{pe}^2}{\Omega_e^2}\left|\frac{\partial\phi}{\partial x}\right|^2 + \frac{\omega_{pe}^2}{\omega^2}\left|\frac{\partial\phi}{\partial z}\right|^2\right] \tag{4a}$$

$$F_{iz}(x,z) = -\frac{\epsilon_o}{4}\frac{\partial}{\partial z}\left[\frac{\omega_{pi}^2}{\omega^2}\left|\frac{\partial\phi}{\partial x}\right|^2 + \frac{\omega_{pi}^2}{\omega^2}\left|\frac{\partial\phi}{\partial z}\right|^2\right]. \tag{4b}$$

The z-components of the momentum equations at zero frequency are

$$T_s\frac{\partial n_s}{\partial z} = q_s n_s E_z + F_{sz}. \tag{5}$$

Assuming quasi-neutrality, i.e., $n_e = n_i = n$, we can sum the equations for the electrons and ions to obtain

$$\frac{\partial n}{\partial z} = \frac{1}{T_e+T_i}(F_{ez}+F_{iz}) = \frac{1}{T}\frac{\epsilon_o}{4}\frac{\partial}{\partial z}\left[\frac{\omega_{pe}^2}{\Omega_e^2}\left|\frac{\partial\phi}{\partial x}\right|^2 - \frac{\omega_{pe}^2}{\omega^2}\left|\frac{\partial\phi}{\partial z}\right|^2 - \frac{\omega_{pi}^2}{\omega^2}\left|\frac{\partial\phi}{\partial x}\right|^2 - \frac{\omega_{pi}^2}{\omega^2}\left|\frac{\partial\phi}{\partial z}\right|^2\right], \tag{6}$$

where $T = T_e + T_i$. We can simplify the term in square brackets by noting that since there is only one high-frequency mode in our problem, the ratio $\frac{\partial\phi}{\partial x}\Big/\frac{\partial\phi}{\partial z} = \frac{E_x}{E_z} = \tan\theta$ is constant to lowest order, since lower hybrid modes are cold and electrostatic. θ satisfies the cold lower hybrid dispersion relation:

$$1 - \frac{\omega_{pi}^2}{\omega^2} - \cos^2\theta\,\frac{\omega_{pe}^2}{\omega^2} + \sin^2\theta\,\frac{\omega_{pe}^2}{\Omega_e^2} = 0. \tag{7}$$

Hence the term in square brackets becomes $|\nabla\phi|^2$ and can be written

$$\frac{\partial n}{\partial z} = -\frac{\epsilon_o}{4T}\frac{\partial}{\partial z}|\nabla\phi|^2. \tag{8}$$

Integrating, we obtain

$$n = n_o\left[1 - \frac{1}{4}\epsilon_o|\nabla\phi|^2/(n_oT)\right]. \tag{9}$$

We substitute this in the $K_\perp$ and $K_\parallel$ appearing in (1) to obtain

$$K_{\perp o}\frac{\partial^2}{\partial x^2}\phi + K_{\parallel o}\frac{\partial^2}{\partial z^2}\phi + a_o\frac{\partial^4}{\partial x^4}\phi + b_o\frac{\partial^4}{\partial x^2\partial z^2}\phi + c_o\frac{\partial^4}{\partial z^4}\phi$$

$$+\frac{\epsilon_o}{4}\alpha_o\frac{\partial}{\partial x}\left[\frac{|\nabla\phi|^2}{n_oT}\frac{\partial}{\partial x}\phi\right] + \frac{\epsilon_o}{4}\beta_o\frac{\partial}{\partial z}\left[\frac{|\nabla\phi|^2}{n_oT}\frac{\partial}{\partial z}\phi\right] = 0, \tag{10}$$

where zero subscript means that ω_{pe} and ω_{pi} are evaluated with $n = n_o$ and

$$\alpha_o = -\frac{\omega_{pe}^2}{\Omega_e^2} + \frac{\omega_{pi}^2}{\omega^2}; \qquad \beta_o = \frac{\omega_{pe}^2}{\omega^2} + \frac{\omega_{pi}^2}{\omega^2}. \tag{11}$$

An approximation to the solution is obtained by setting to zero the sum of the first two terms of (11). The solution then is $\phi = \phi(x-dz)$ where $d = (-K_{\perp o}/K_{\parallel o})^{1/2}$, which is the well-known result that lower hybrid waves propagate without dispersing. The full solution is obtained by allowing ϕ to have a weak explicit dependence on x. Thus $\phi = \phi(y,t)$, where $y = x - dz$, $t = x$ and $\partial\phi/\partial t = 0(\epsilon)$. We assume that the coefficients a_o, b_o, c_o, α_o, and β_o are all of order ϵ, that ϕ is real, and that $|\nabla\phi| \cong |\partial\phi/\partial x|$, since $d \ll 1$. To order ϵ (10) becomes

$$2K_\perp u_t + (a_o + b_od^2 + c_od^4)u_{yyy} + \left(\frac{\alpha_o + \beta_od^2}{2}\right)\frac{6u^2u_y}{4n_oT/\epsilon_o} = 0, \tag{12}$$

where $u = \partial\phi/\partial y \approx \partial\phi/\partial x$. If we let

$$v = \frac{u}{(4n_oT/\epsilon_o)^{1/2}} = \frac{E_x}{(4n_oT/\epsilon_o)^{1/2}} \tag{13a}$$

$$\xi = \left[\frac{\alpha_o + \beta_o d^2}{2\left[a_o + b_o d^2 + c_o d^4\right]}\right]^{1/2} y \tag{13b}$$

$$\tau = \frac{\left[\frac{1}{2}\left(\alpha_o + \beta_o d^2\right)\right]^{3/2}}{\left[a_o + b_o d^2 + c_o d^4\right]^{1/2} 2K_{\perp o}} t, \tag{13c}$$

then (12) becomes

$$v_\tau + 6v^2 v_\xi + v_{\xi\xi\xi} = 0, \tag{14}$$

which is the standard form of the modified Korteweg-de Vries equation. Note that v is E_x normalized to the plasma energy and ξ and τ are $x - dz$ and x in units of approximately λ_{De}.

Solution of the Modified KdV Equation Using the Inverse Scattering Method

We shall outline the method of solution of Eq. 14, using the inverse scattering transform method, so-named because it may be considered a nonlinear generalization of the Fourier transform method for solving linear problems. Following the discussion by Lax,[2] we can state the requirements on a general nonlinear wave equation

$$N(v) = 0 \tag{15}$$

as follows. If (i) there have been found a linear operator L that acts on a wave function ψ, with eigenvalue λ,

$$L\psi = \lambda\psi, \tag{16}$$

(ii) a linear operator B that gives the (time) evolution of ψ as

$$\psi_\tau = B\psi, \tag{17}$$

and (iii) L and B satisfy the operator equation

$$L_\tau = BL - LB \tag{18}$$

when ϕ satisfies (14), then the eigenvalues of L remain constant as ϕ evolves according to (15), and the inverse scattering transform method of solution may be carried through. The method proceeds in three steps.

1. Direct problem. Given the initial data, $v(0)$, consider it as a "scattering potential" for the operator L. The scattering parameters [(i.e., the eigenvalues and eigenfunctions of (16)] are calculated at $\tau = 0$.

2. Time evolution of the scattering data. Since the eigenvalues λ remain constant with time, time evolution of the eigenfunctions can be calculated by using (17) at large values of ξ where v is equal to some asymptotic values.

3. Inverse problem. From a knowledge of the scattering data at large values of ξ and as a function of τ, $v(\xi, \tau)$ is constructed by using the techniques of inverse scattering theory. For the modified KdV equation, Ablowitz et al. have shown[3] that the conditions of (16) through (18) can be satisfied in the following way. Take ψ to be the two-dimensional vector

$$\psi = \begin{bmatrix} \psi_1 \\ \psi_2 \end{bmatrix}$$

and L and B the matrix operators

$$L = i \begin{bmatrix} \partial/\partial\xi & -v \\ -v & -\partial/\partial\xi \end{bmatrix} \tag{19}$$

$$B = \begin{bmatrix} -4i\lambda^3 + 2iv^2\lambda & 4v\lambda^2 + 2iv_\xi\lambda - 2v^3 - v_{\xi\xi} \\ -4v\lambda^2 + 2iv_\xi\lambda + 2v^3 + v_{\xi\xi} & 4i\lambda^3 - 2iv^2\lambda \end{bmatrix}, \tag{20}$$

then (16) becomes the scattering problem

$$\psi_{i\xi} + i\lambda\psi_1 = v\psi_2 \tag{21a}$$

$$\psi_{2\xi} - i\lambda\psi_2 = -v\psi_1. \tag{21b}$$

We apply this method to the following boundary-value problem. We assume that at $\tau = 0$ $(x = 0)$ the normalized potential v is given by

$$\left.\begin{aligned} v &= -v_o \text{ for } -\ell < \xi < 0 \\ v &= \ \ v_o \text{ for } 0 < \xi < \ell \\ v &= \ \ 0 \ \text{ for } |\xi| > \ell \end{aligned}\right\} \tag{22}$$

(see Fig. XII-24). In solving (21) for ψ, given the potential v in (22), we choose the transmitted wave at $\xi \to -\infty$ to be $\begin{bmatrix}1\\0\end{bmatrix} e^{-i\lambda\xi}$ and define the incident wave at $\xi \to \infty$ to be $\begin{bmatrix}1\\0\end{bmatrix} a\, e^{-i\lambda\xi}$ and the reflected wave to be $\begin{bmatrix}0\\1\end{bmatrix} b\, e^{+i\lambda\xi}$. Substituting (22) in (21) and matching boundary conditions at $\xi = 0, \pm\ell$, we obtain

$$a(\lambda, 0) = \frac{e^{2i\lambda\ell}}{k^2}\left[(1-\Lambda^2)s^2 - 2ik\Lambda sc + k^2c^2\right] \tag{23}$$

$$b(\lambda, 0) = \frac{2i\Lambda s^2}{k^2}, \tag{24}$$

where $\Lambda = \lambda/v_o$, $k = (1+\Lambda^2)^{1/2}$, $s = \sin(kA)$, $c = \cos(kA)$, and A is the area of the pulse, v_o^{ℓ}. At zeros of $a(\lambda, 0)$ for which $\text{Re}\,[i\lambda] < 0$, it is clear from Fig. XII-24 that we have bound states characterized by an exponential decay of the reflected wave to the right and of the transmitted wave to the left. These bound states are of primary concern

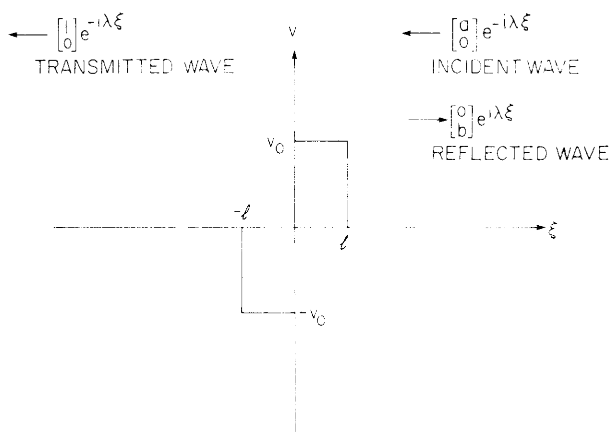

Fig. XII-24. Boundary conditions imposed by two oppositely phased waveguides and boundary conditions on ψ for the scattering problem (Eq. 22).

because, as we shall see, they correspond to solitons that have been introduced into the solution by the initial conditions. From (21), $a(\lambda, 0) = 0$ implies that

$$\left[(1-\Lambda)s - ikc\right]\left[(1+\Lambda)s + ikc\right] = 0 \tag{25}$$

gives the values of λ where bound states occur. It is interesting to note that the bound-state eigenvalues always come in pairs

$$\lambda_j = -\lambda_{j+1}^{*}, \qquad j = 1, 3 \ldots \tag{26}$$

These pairs of eigenvalues give rise to coupled pairs of solitons, usually known as "breathers." It is found that if $\int_{-\infty}^{\infty} v(\xi,0)\, d\xi = 0$, then (26) is always true and only breather solutions occur.

In order to calculate the τ dependence of a and b, we note that $v \to 0$ as $|\xi| \to \infty$ (where a and b are as defined). Thus Eq. 20 for B can be simplified and Eq. 17 can easily be solved. Choosing the same normalization as before (i.e., $\psi \to \begin{bmatrix} 1 \\ 0 \end{bmatrix} e^{-i\lambda\xi}$ as $x \to -\infty$), we find

$$a(\lambda,\tau) = a(\lambda,0) \tag{27a}$$

$$b(\lambda,\tau) = b(\lambda,0)\, e^{8i\lambda^3\tau}. \tag{27b}$$

This completes the second step of the inverse scattering transform method.

The third step involves the reconstruction of $v(\xi,\tau)$ from the asymptotic information contained in (27). This inverse scattering calculation is accomplished[2,3] by solving the (Marchenko) integral equation

$$K(x,y) = \hat{B}^*(x,y) - \int_x^{\infty}\int_x^{\infty} \hat{B}^*(y+z)\, \hat{B}(k+z)\, K(x,k)\, dz\,dk \tag{28}$$

for K(x,y), where

$$\hat{B}(x) = \frac{1}{2\pi}\int_{-\infty}^{\infty} \frac{b(\lambda)}{a(\lambda)}\, e^{i\lambda x}\, d\lambda - i\sum_{j=1}^{N} c_j\, e^{i\lambda_j x}. \tag{29}$$

The sum is over the N discrete eigenvalues, and c_j is the residue of the reflection coefficient b/a at the pole $\lambda = \lambda_j$. From K(x,y) the potential can be calculated as

$$v = -2K(\xi,\xi) \tag{30}$$

(τ enters implicitly into (30) through b, see Eq. 27b). The first term on the right-hand side of (29) introduces the radiative part of the solution which exists as a background to the soliton part. The second term (the sum) introduces the soliton part of the solution. Each term in the sum gives rise to an individual soliton in the final computation of (30). The radiative part of the solution spreads out over the ξ axis and becomes negligible as $\tau \to \infty$. Thus for our purposes it is reasonable to neglect the radiative part and concentrate on the soliton dynamics.

If we set $b(\lambda) = 0$ in (29), then (28), (29), and (30) can be solved to give

$$v = -2PH \tag{31}$$

where

$$P_{1j} = e^{-i\lambda_j^* x} \tag{32}$$

$$H = [I + G^* G]^{-1} M \tag{33}$$

$$M_{j1} = i\mu_j^* P_{1j} \tag{34}$$

$$G_{jk} = \frac{\mu_j \exp\left(i\left(\lambda_j - \lambda_k^*\right)x\right)}{\lambda_j - \lambda_k^*} \tag{35}$$

$$\mu_j = \left.\frac{b(\lambda, \tau)}{\partial a(\lambda)/\partial\lambda}\right|_{\lambda=\lambda_j}. \tag{36}$$

Here P is a $1 \times N$ row matrix, M and H are $N \times 1$ column matrices, and G is an $N \times N$ matrix.

One- and Two-Breather Solutions

From (25) we can derive the condition for roots such that Im $(\lambda) > 0$ and so find the threshold for breathers. With increasing A the complex roots of (25) move from the lower half-plane, so the threshold for a new root to appear with Im $(\lambda) > 0$ is Im $(\lambda) = 0$. If λ and hence Λ are real, then k is real and greater than 1. Hence s and c are real, and setting the imaginary part of the first factor to zero, we find that $c = 0$. This implies that $s = 1$ and setting to zero the real part of the first factor of (25), we have $\Lambda = 1$ (the other factor gives $\Lambda = -1$), and $k = \sqrt{2}$. Thus the condition for there to be n breathers is just

$$\left(n + \frac{1}{2}\right)\frac{\pi}{\sqrt{2}} > A > \left(n - \frac{1}{2}\right)\frac{\pi}{\sqrt{2}}; \qquad A = v_o \ell. \tag{37}$$

Note that the number of breathers is dependent only on the area of the pulse, although for a given area the eigenvalue λ of each breather is proportional to the height, v_o, of the pulse.

If $\pi/2\sqrt{2} < A < 3\pi/2\sqrt{2}$, then the initial pulse contains just one breather. By writing the eigenvalues $\lambda_1 = -\lambda_2^* = \lambda_r + i\lambda_i$ with $\lambda_r > 0$, Eqs. 31-36 can be reduced to

$$v(\xi, \tau) = \frac{4\lambda_i}{\lambda_r}\left[\frac{\lambda_r \cosh\theta_1 \sin\theta_2 + \lambda_i \sinh\theta_1 \cos\theta_2}{\cosh^2\theta_1 + \dfrac{\lambda_i^2}{\lambda_r^2}\cos^2\theta_2}\right], \tag{38}$$

where

$$\theta_1 = 2\lambda_i\xi - \omega_r\tau - \log\left(\frac{|c|\lambda_r}{2\lambda_i|\lambda|}\right)$$

Table XII-3. Eigenvalues and group velocity.

	Initial Pulse		
	One Breather	Two Breathers	
A	$\pi/\sqrt{2}$	$2\pi/\sqrt{2}$	
ℓ	$10\pi/\sqrt{2}$	$10\pi/\sqrt{2}$	
v_o	1/10	1/5	
λ	0.038 + i 0.046	0.011 + i 0.158	0.105 + i 0.039
v_g	-0.009	0.098	-0.126

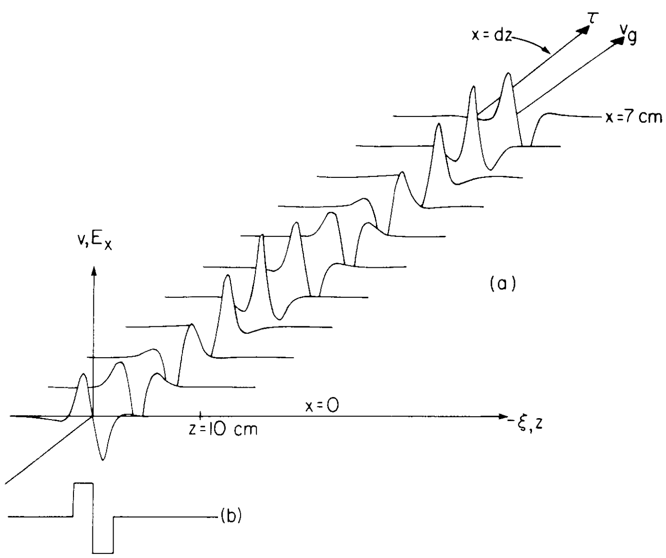

Fig. XII-25.
(a) One-breather solution.
(b) Boundary condition giving (a).
$v_o = 1/10$, $\ell = 10\pi/\sqrt{2}$.

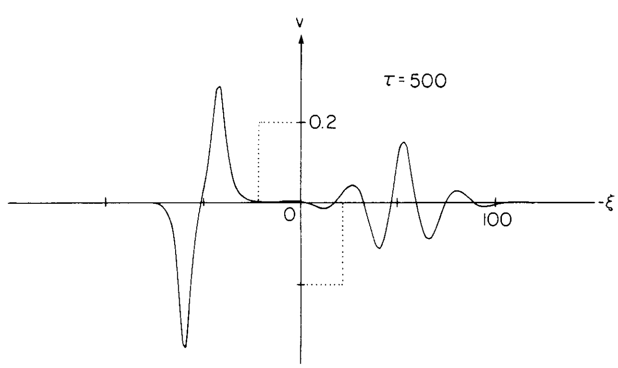

Fig. XII-26. Two-breather solution at $\tau = 500$ for the boundary condition at $\tau = 0$ of $v_o = 1/10$ and $\ell = 10\pi/\sqrt{2}$ (dotted line).

$$\theta_2 = 2\lambda_r \xi + \omega_i \tau - i \log \left(\frac{c}{|c|} \frac{|\lambda|}{\lambda} \right)$$

$$c = \mu_1(\tau = 0)$$

$$\omega_r + i\omega_i = 8i\lambda^3.$$

Interpreting θ_1 in (38) as the envelope phase and θ_2 as the carrier phase, we find that the group velocity of the pulse is

$$v_g = \omega_r/2\lambda_i. \tag{39}$$

If we transform back to coordinates x, z, this means that the breather travels along a path $dz = (1-v_g)x$. For a given area of the pulse λ is proportional to v_o; hence, the deviation of the breather from the linear characteristic direction is proportional to v_o^2.

In Fig. XII-25 we plot $v(\xi, \tau)$ for $A = \pi/\sqrt{2}$, $v_o = 1/10$ (i.e., the electric field energy is 1/100th of the plasma energy), and $\ell = 10\pi/\sqrt{2}$. (For a plasma with $T_e = 1$ keV, $n_o = 10^{14}$ cm^{-3}, and $\omega = \sqrt{2}\, \omega_{LH}$, this corresponds to a source width of 2 cm and an electric field amplitude inside the plasma of 8×10 V.) The eigenvalues and group velocity for this case are given in Table XII-3. We also plot in Fig. XII-25 the boundary conditions at x = 0 (the difference between the boundary conditions at the breather solution at x = 0 is the radiative part of the solution). If we now consider the case $v_o = 1/5$ and $\ell = 10\pi/\sqrt{2}$ so that $A = 2\pi/\sqrt{2}$, then two breathers are present in the solutions. Far from the source the two breathers separate and we can then use (38) to find v_g for each breather (see Table XII-3). Using these values, we calculate the separation of the breathers at, say, $\tau = 500$ (x = 1 cm), to be around 10 cm (see Fig. XII-26).

Conclusion

We have shown how the boundary value problem for the modified KdV equation may be solved using the inverse scattering method. In order to derive the modified KdV equation it was necessary to assume that the field amplitude is real. This implies that energy is propagating both away from and toward the source. The relevant problem for lower hybrid wave excitation in a Tokamak must consider a formulation in which energy propagates away from the source. This means that we must use complex field amplitudes which leads to a different nonlinearity in Eq. 14. We are now working on the solution of this problem.

References

1. G. J. Morales and Y. C. Lee, Phys. Rev. Letters 35, 930 (1975).
2. P. D. Lax, Communs. Pure Appl. Math. 21, 467 (1968).
3. M. J. Ablowitz, D. J. Kaup, A. C. Newell, and H. Segur, Stud. Appl. Math. 53, 249 (1974).

5. MODEL FOR ANOMALOUS ION HEATING IN THE LOW-DENSITY DISCHARGE OF ALCATOR

U. S. Energy Research and Development Administration (Contract E(11-1)-3070)

Miloslav S. Tekula, Abraham Bers

Introduction

The Alcator Tokamak when operated in a low-density (10^{13}/cc), high drift velocity regime ($\langle V_D/V_{Te}\rangle = \langle J/enV_{Te}\rangle \geq 0.4$ in hydrogen) exhibits anomalous radiation and ion heating.[1] In this regime it was observed from soft and hard x-ray spectra that the electron distribution function had a high-energy tail containing approximately 30% of the particles. Furthermore, RF emissions, peaked at ω_{pi} and extending to (5-10) ω_{pi}, were observed. The high-frequency emissions were correlated with the onset of hard x rays and always appeared before the ω_{pi} emissions. Finally, strong ion heating (0.2-1) keV was observed when the ω_{pi} emissions appeared.

To explain these observations, we shall assume that the instabilities that are necessary to drive the observed phenomena are generated in the core of the device where the plasma can be assumed homogeneous and trapped particles are negligible. In Progress Report No. 116 (pp. 128-138) we discussed some of the possible model distribution functions. We have settled on an anisotropic distribution function driven by the dc electric field, which has a Maxwellian bulk with a high-energy tail that is also Maxwellian in $v_\perp$ but is flat in $v_\parallel$ as shown in Fig. XII-27. Such a distribution function may form in the initial stages of the discharge when $E_o \sim E_{crit}$.[2] The quasi steady state $E_o \ll E_{crit}$ is eventually reached, since the applied electric field is a decreasing function of time. The additional runaway electrons that are now generated are not important because they are so few.[3]

With this distribution function we find the following: (a) Trivelpiece-Gould (T-G) waves with $\omega = \omega_{pe}\cos\theta$ are driven unstable. These inhibit the high-energy runaway

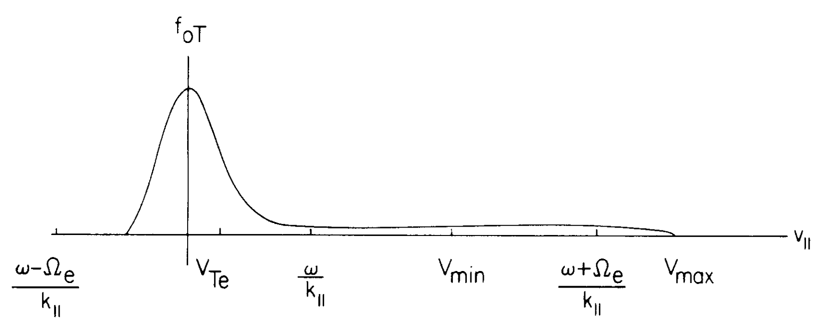

Fig. XII-27. Parallel electron distribution function.

tail and thus account for the observed decrease in hard x rays. (b) The T-G waves in turn downconvert parametrically to lower hybrid (LH) waves directly and also by cascading, to account for the observed peak in the RF emission at ω_{pi}. (c) Finally, the LH waves heat the ions by nonlinear orbit perturbation. We shall show that the rates and fields that are necessary for these processes to proceed are easily met. We have found that the tail and unstable T-G waves are stabilized by the combined effects of quasi-linear scattering and parametric downconversion.

Linear Theory

The tail will be required to carry all the current. We can relate the current to the streaming parameter $\langle V_D/V_{Te}\rangle$ and so we find that

$$\frac{n_T}{n_o} = 2\left\langle\frac{V_D}{V_{Te}}\right\rangle\left(\frac{S_2}{S_1}\right)\left(\frac{a_c}{a}\right)^2\left(\frac{V_{Te}}{V_{max}}\right), \tag{1}$$

where $S_{1,2}$ are profile integrals, a_c is the experimentally estimated current channel, and V_{max} is the maximum parallel speed of the electron distribution function. In the case of Alcator we have $S_2/S_1 = 0.5$, $a_c \approx 8$ cm. Taking $\langle V_D/V_{Te}\rangle = 0.45$ and $V_{max}/V_{Te} = 20$, we find that in order to have 30% of the electrons in the tail we need to take $a/a_c = 0.3$, where a is the effective radius of the tail current.

The dispersion relation for electrostatic waves in a homogeneous magnetoplasma can be obtained from the usual Harris dispersion relation[4]

$$\frac{\epsilon(\omega,k)}{\epsilon_o} = 1 + \sum_s 2\pi\frac{\omega_{ps}^2}{k^2}\int_0^\infty v_\perp\, dv_\perp \sum_n J_n^2(k_\perp a_s)\frac{1}{\xi_{ns}}\left[k_\parallel\frac{\partial F_{os}}{\partial v_\parallel} + 2n\Omega_s\frac{\partial F_{os}}{\partial v_\perp^2}\right] = 0 \tag{2a}$$

with

$$\begin{aligned}\gamma\frac{\partial}{\partial\omega}(\omega\epsilon) = {} & \frac{\pi^2}{2}\,\omega\,\frac{k_\parallel}{|k_\parallel|}\sum_s\frac{\omega_{ps}^2}{k^2}\frac{\Omega_s^2}{k_\perp^2}\int_0^\infty a\, da\, J_o^2(a)\left.\frac{\partial F_{os}}{\partial v_\parallel}\right|_{\omega/k_\parallel} \\ & + \frac{\pi^2}{2}\,\omega\,\frac{k_\parallel}{|k_\parallel|}\sum_s\frac{\omega_{ps}^2}{k^2}\frac{\Omega_s^2}{k_\perp^2}\int_0^\infty a\, da\sum_{n=1}^\infty J_n^2(a)\left[\left.\frac{\partial F_{os}}{\partial v_\parallel}\right|_{V_n^+} + \left.\frac{\partial F_{os}}{\partial v_\parallel}\right|_{V_n^-}\right] \\ & - \frac{\pi^2}{2}\,\omega\,\frac{k_\parallel}{|k_\parallel|}\sum_s\frac{\omega_{ps}^2}{k^2}\int_0^\infty da\sum_{n=1}^\infty n\Omega_s\frac{\partial}{\partial a}J_n^2(a)\left[F_{os}\left(a^2,V_n^-\right) - F_{os}\left(a^2,V_n^+\right)\right],\end{aligned} \tag{2b}$$

where $\xi_{ns} = \omega - n\Omega s - k_{\|}v_{\|}$, $\omega_{ps}^2 = e^2 n_{os}/m_s\epsilon_o$, $\Omega_s = eB_o/m_s$, $k_{\|}, k_{\perp}$ are the parallel and perpendicular wave numbers, ω, γ are the frequency and damping rate, s specifies the species, and J_n is the usual Bessel function $a = k_{\perp}v_{\perp}/\Omega_s$, where $V_{Ts}^2 = T_s/m_s$ and $V_n^{\pm} = (\omega \pm n\Omega_s)/k_{\|}$. In Eq. 2b the first term is the usual Landau resonance contribution. The second term is due to Doppler-shifted Landau resonances. The third term gives the cyclotron effects. We have an instability if $\gamma > 0$.

Let us now look for waves that have $\omega/k_{\|} > V_{Te}$, $k\lambda_{De} \ll 1$, $k_{\perp}a_e \ll 1$. Using a distribution function such as that in Fig. XII-27, we find oscillations at $\omega = \omega_{pe} \cos\theta$. Examining Eq. 2b, for the distribution function in Fig. XII-27 we see that if $\partial F_o/\partial v_{\|}\big|\omega/k_{\|} = 0$, and $\partial F_o/\partial v_{\|}\big|V_n^{\pm} = 0$, but $F_o\left(V_1^+\right) > F_o\left(V_1^-\right)$, these waves are destabilized. The growth rate is given approximately by

$$\frac{\gamma}{\omega_{pe}} = \frac{\pi}{16} \frac{n_T}{n_o} \frac{\omega_{pe}^2}{\Omega_e^2} \Omega e \frac{k_{\|}}{|k_{\|}|} \frac{k_{\perp}^2}{k^3} f_{oT} \left[\frac{\omega + \Omega_e}{k_{\|}}\right], \tag{3}$$

where n_T, n_o is the number of particles in the tail and bulk, respectively, and the distribution function is evaluated $(\omega+\Omega_e)/k_{\|}$. A tail that extends up to energies of 200 keV can destabilize T-G waves with phase velocities between (3-5) V_{Te}. They are driven unstable by the particles with energies between (100-200) keV. The lower bound on the phase velocities is imposed by bulk electron Landau damping. We have found that the

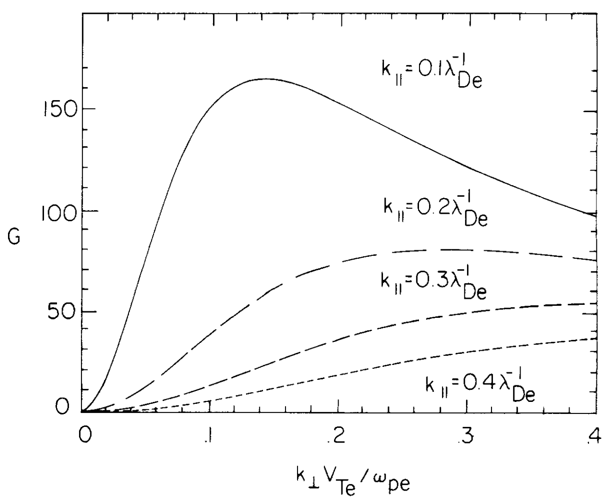

Fig. XII-28.

Linear growth rates. $G = \left[\dfrac{\gamma}{\dfrac{\pi}{16}\dfrac{n_T}{n_o}\dfrac{\omega_{pe}^2}{\Omega_e^2}\omega_{pe}\Omega_e f_{oT}\left(\dfrac{\omega+\Omega_e}{k_{\|}}\right)} = \dfrac{k_{\|}}{|k_{\|}|}\dfrac{k_{\perp}^2}{\left(k_{\perp}^2+k_{\|}^2\right)^{3/2}}\right].$

most unstable T-G waves have $k_\perp = \sqrt{2}\ k_\parallel$ (see Fig. XII-28). The maximum growth rate is $\gamma/\omega_{pi} = 0.4$. The spectrum extends from $k_\parallel \lambda_{De} = .1-.4$ as shown in Fig. XII-29. From this it is clear that LH waves cannot be excited directly.

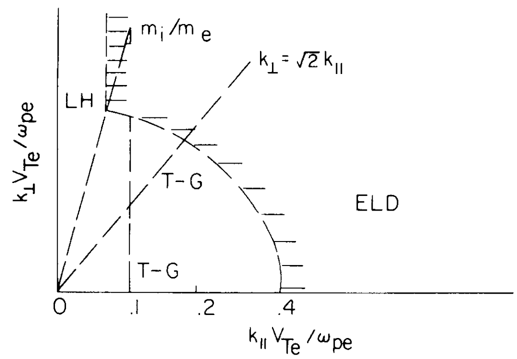

Fig. XII-29. Spectrum of unstable waves.

Quasi-linear Theory

To see how this instability affects the distribution function we study the system of quasi-linear equations:[5]

$$\omega = \omega_{pe} \frac{k_\parallel}{k} \tag{4a}$$

$$\frac{\partial}{\partial t} \phi_k^2 = 2\gamma\phi_k^2 \tag{4b}$$

$$\gamma = \frac{\pi^2}{4} \omega \frac{n_T}{n_o} \frac{\omega_{pe}^2}{k^2} \int_0^\infty v_\perp dv_\perp \int_{-\infty}^{\infty} dv_\parallel$$

$$\times\, \delta\left[v_\parallel - \frac{\omega + \Omega_e}{k_\parallel}\right] J_1^2(a) \left[\frac{\partial}{\partial v_\parallel} + \frac{\omega - k_\parallel v_\parallel}{k_\parallel v_\perp} \frac{\partial}{\partial v_\perp}\right] \langle f_{oT} \rangle \tag{4c}$$

$$\frac{\partial}{\partial t} \langle f_{oT} \rangle = 8\pi^2 \frac{e^2}{m_e^2} \int d^3k\, \phi_k^2 k_\parallel^2 \left[\frac{\partial}{\partial v_\parallel} + \frac{\omega - k_\parallel v_\parallel}{k_\parallel v_\perp} \frac{\partial}{\partial v_\perp}\right]$$

$$\times\, J_1^2(a)\, \delta[\omega + \Omega_e - k_\parallel v_\parallel] \left[\frac{\partial}{\partial v_\parallel} + \frac{\omega - k_\parallel v_\parallel}{k_\parallel v_\perp}\right] \langle f_{oT} \rangle. \tag{4d}$$

This set cannot be solved in closed form. But we can examine the time asymptotic state of the system. To do this we multiply Eq. 4d by $\langle f_{oT}\rangle$ and integrate over all velocities to get a quasi H-theorem:

$$\frac{\partial}{\partial t}\int \langle f_{oT}\rangle^2\, d^3v = -8\,\frac{\pi^2 e^2}{m_e^2}\int d^3k \int d^3v\, k_{\|}^2 \phi_k^2 J_1^2(\alpha)$$

$$\times\, \delta\left[\omega+\Omega_e - k_{\|}v_{\|}\right]\left\{\left[\frac{\partial}{\partial v_{\|}} + \frac{\omega - k_{\|}v_{\|}}{k_{\|}v_{\perp}}\,\frac{\partial}{\partial v_{\perp}}\right]\langle f_{oT}\rangle\right\}^2 \tag{5a}$$

after an integration by parts of the right-hand side. Thus we have found that the time rate of change of a purely positive-definite quantity is negative. This leads us to look for quasi-stationary solutions where the right-hand side of Eq. 5a vanishes. Since we wish to have a steady state with a nonzero spectral energy density, we find that we require

$$\left[\frac{\partial}{\partial v_{\|}} + \frac{\omega - k_{\|}v_{\|}}{k_{\|}v_{\perp}}\,\frac{\partial}{\partial v_{\perp}}\right]\langle f_{oT}\rangle = 0. \tag{5b}$$

This implies that time asymptotically $\langle f_{oT}\rangle$ has to be constant along the following trajectories:

$$\frac{\Delta v_{\|}}{\Delta v_{\perp}} = \frac{k_{\|}v_{\|}}{\omega - k_{\|}v_{\|}}. \tag{5c}$$

In the case of $k_{\perp} > k_{\|}$ (for the most unstable waves) the dispersion relation is given by $\omega \cong \omega_{pe}k_{\|}/k_{\perp}$. From the resonance condition we have $k_{\|} = (\omega+\Omega_e)/v_{\|}$. Combining all this in Eq. 5c, we get

$$\frac{\Delta v_{\|}}{\Delta v_{\perp}} \cong \frac{-v_{\perp}}{v_{\|} - \dfrac{\omega_{pe}}{k_{\perp}}} \tag{5d}$$

which gives circles centered at $\omega_{pe}/k_{\perp}$. Thus, as shown in Fig. XII-30, under the influence of the unstable T-G spectrum, particles in the tail are scattered along the trajectories given by Eq. 5d. That these are indeed the scattering paths can be verified by examining the equations of conservation of energy and parallel momentum between the T-G waves and the resonant particles. Thus a typical resonant particle gets scattered to a lower energy surface and hence gives up its energy to the wave. Particles with energies greater than 200 keV would diffuse along ellipses centered at the origin, but the ellipticity of these diffusion paths is of the order of ω_{pi}/Ω_e, and thus these

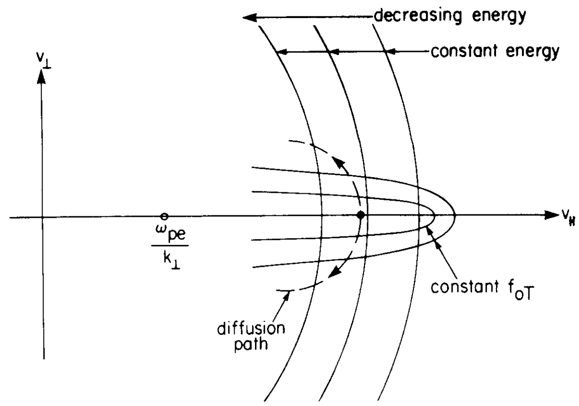

Fig. XII-30. Diffusion paths in velocity space.

particles are not effectively scattered and hence are lost. An order-of-magnitude scaling of the diffusion equation (Eq. 4d) gives for the relaxation rate

$$\frac{\nu_{relax}}{\omega_{pe}} \approx 10^{-4}\left[\epsilon_o\langle E^2\rangle/4n_oT\right], \tag{6}$$

where $\langle E^2\rangle$ is the saturated spectrum of T-G waves, and n_oT is the electron plasma energy.

From the given spectrum we can also estimate the correlation time of the most unstable waves, and we find this given by

$$\gamma\tau_{ac} \approx 300\,\frac{\gamma}{\omega_{pe}}\,k_{\parallel}\lambda_{De}\,\frac{V_{Te}}{\Delta v_{\parallel}}, \tag{7}$$

where $\Delta v_{\parallel}$ is the width of the resonant region. Hence we find $\gamma\tau_{ac} \ll 1$. We also find from Eq. 6 that if we pick reasonable saturated spectra, $\nu_{relax}\tau_{ac} \ll 1$. Under the influence of only quasi-linear scattering the saturated spectrum would achieve a value of the order of

$$\frac{\epsilon_o\langle E^2\rangle}{4n_oT} \approx \frac{n_T}{n_o}\,\frac{(V_{max}-V_{min})^2}{V_{max}}\,\frac{\omega_{pe}}{k_\perp V_{Te}^2}, \tag{8}$$

where V_{min} is the edge of the resonant region ($14V_{Te}$). For the spectrum shown we find that this gives $\epsilon_oE^2/4n_oT \sim 1$. Hence the instability cannot saturate under the influence of only quasi-linear scattering. The additional stabilization is provided by parametric downconversion.

Parametric Downconversion

The coupling of T-G and LH waves is very easy to achieve. We study the coupling between waves[6] that have $k_\perp a_i < 1$ and also $k_\perp a_i \gg 1$. In both cases we need

$$\omega_1 = \omega_2 + \omega_3 \tag{9a}$$

$$\underline{k}_1 = \underline{k}_2 + \underline{k}_3, \tag{9b}$$

where 1 is the pump, 2 the idler, and 3 the lower hybrid waves. There are three processes whereby the energy from the T-G waves gets into LH waves. First, some of the energy comes from T-G waves which have a frequency near ω_{pi} and hence a very steep angle of propagation. In Fig. XII-31a, for example, $\omega_1 = 3\omega_{pi}$, $\omega_2 = 2\omega_{pi}$, $\omega_3 = \omega_{pi}$. Second, as shown in Fig. XII-31b, we could have $\omega_1 = \omega_{pe} \cos\theta_1$, $\omega_2 = \omega_{pe}\cos\theta_2$, and $\omega_3 = \omega_{pi}$. In this case we find that $\theta_1 \sim \theta_2$. Finally, the idler itself can decay into a lower frequency T-G wave and a LH wave (Fig. XII-31b). This final process of cascading accounts for the observed peak in the radiation at ω_{pi}. With $k_\perp a_i \leqslant 1$ the first two processes have comparable growth rates given by

$$\frac{\gamma_{NL}}{\omega_{pe}} \approx 10^{-3} \frac{e\phi_1 k_{\perp 1}^2}{m_e \omega_{pe} \omega_{pi}}. \tag{10}$$

These waves propagate out of the plasma by the inverse of the process used for lower hybrid heating experiments [see Progress Report No. 116 (pp. 128-138) and Quarterly Progress Report No. 102 (pp. 97-111)]. We have also studied the coupling to lower hybrid waves with $k_\perp a_i \geqslant 1$, since these are the waves that account for the ion heating. In Fig. XII-31a the coupling is now between three kinetic modes and hence it is difficult to calculate the coupling coefficient; however, in Fig. XII-31b the coupling is between two fluid modes (the T-G waves) and a kinetic mode (the LH wave), and so we can

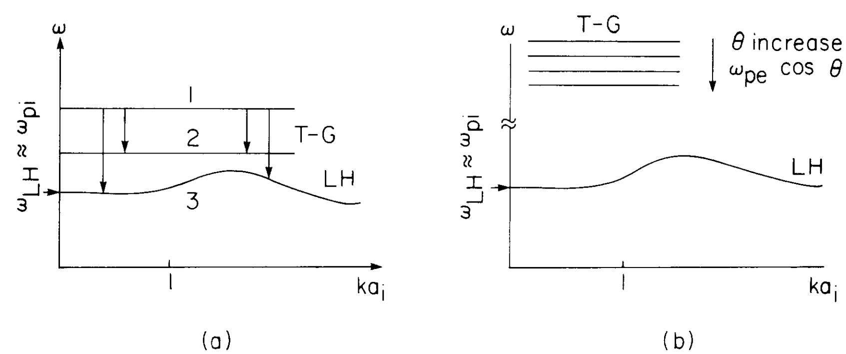

Fig. XII-31. Coupling between Trivelpiece-Gould and lower hybrid waves. (a) $|\theta-\pi/2| \sim (m_e/m_i)^{1/2}$. (b) $|\theta-\pi/2| \gg (m_e/m_i)^{1/2}$.

calculate the coupling coefficient between the two fluid modes because of the symmetry relations that the coupling coefficients obey for three-wave interactions. But when we compute the growth rate of the LH wave we have to take into account properly the mode energy for $k_\perp a_i \geq 1$. Thus we find that the nonlinear growth rate of the LH wave for $k_\perp a_i \geq 1$ is given by

$$\frac{\gamma_{NL}}{\omega_{pe}} = 10^{-3} \frac{e\phi_1 k_{\perp 1}^2}{m_e \omega_{pe} \omega_{pi}}. \tag{11}$$

Nonlinear Orbit Breaking and Ion Heating

Electrostatic waves propagating nearly across B_o and having $k_\perp > a_i^{-1}$ (the inverse ion-cyclotron radius) may trap the ion (during part of its orbit) and give to it sufficient energy to make a strong change in its unperturbed closed path. This may happen for the perpendicular trapping condition

$$V_{tr\perp} \stackrel{\Delta}{=} \sqrt{\frac{eE_\perp}{m_i k_\perp}} = \frac{\omega}{k_\perp} - V_{\perp o}, \tag{12}$$

where $V_{\perp o}$ is the unperturbed ion velocity. The details of this process are given in Part II, Section XII-B.4. The maximum energy transfer occurs very near this threshold and is given approximately by

$$\langle \Delta \mathscr{E} \rangle \cong 2m_i \frac{\omega}{k_\perp} V_{tr\perp} n_o\, e^{-V_{\perp o}^2/2V_{Ti}^2}. \tag{13}$$

Letting $V_{\perp o} \sim V_{Tio}$ (corresponding to the initial ion temperature T_{io}), and using $k_\perp a_i \sim 5$ for the parametrically excited lower hybrid wave at $\omega \sim \omega_{pi} \sim 10\ \Omega_i$, we find from Eqs. 12 and 13 that the maximum energy given to the ions per cyclotron period is approximately $\langle \Delta \mathscr{E} \rangle \sim n_o T_{io}$ at an E-field energy $\langle W_e \rangle_{LH} \sim 8 \times 10^{-3}\ n_o T_e$.

Knowing now the field that is necessary for orbit breaking and ion heating, we can work back and find what the field energy in the T-G waves has to be. For example, for growing T-G waves at $\omega \sim 10\ \omega_{pi}$ the Manley-Rowe relations in the absence of cascading would require approximately ten times the energy in the LH waves. Thus we may assume that the energy in these fields is $\epsilon_o E_{TG}^2/4n_o T \sim 10^{-2}$, which is a rather modest level. We can now use these fields in Eq. 6 and Eq. 10 to get $\nu_{relax} \sim 10^{-5}\ \omega_{pe}$, $\gamma_{NL} \sim .04\ \omega_{pi}$, respectively. The cascading rate from $10\ \omega_{pi}$ would be approximately $\gamma_{NL} \sim .004\ \omega_{pi}$.

Conclusion

An electron distribution function with a high-energy tail is used to explain certain features of the Alcator experiment for low-density discharges when the effective drift velocity is high. The high-energy tail excites T-G waves, and this corresponds to the observed high-frequency oscillations up to $20\omega_{pi}$; these T-G waves also account for the quasi-linear pitch angle scattering of the high-energy tail which accounts for the observed decrease in the hard x rays when the high-frequency (T-G) oscillations appear. This process alone cannot stabilize the T-G waves. Additional stabilization is provided by the parametric downconversions of the T-G waves to LH waves. This occurs in two distinct processes, that is, direct downconversion and cascading. Both processes account for the observed peak in the RF emission at $\omega_{pi} = \omega_{LH}$. Once the LH waves have reached large enough amplitude for ion orbit breaking, we find that the ions are heated. Once this process is established, the electric fields never decrease below this threshold value because the downconversion rate is so fast, and hence a steady state is achieved.

References

1. G. J. Boxman, B. Coppi and Alcator Group, "Low and High Density Operation of Alcator," a paper presented at the VIIth European Conference on Plasma Physics, Lausanne, Switzerland, September 1-5, 1975.
2. L. M. Kovriznykh, Sov. Phys. – JETP 37, 989 (1960).
3. R. M. Kulsrud and Y. C. Sun, Annual Plasma Physics Meeting, American Physical Society, St. Petersburg, Florida, November 10-14, 1975, Paper GA5.
4. A. B. Mikhailovskii, Theory of Plasma Instabilities, Vol. 1 (Consultants Bureau, New York, 1974).
5. C. F. Kennel and F. Engelmann, Phys. Fluids 9, 2377 (1966).
6. E. Ott, Phys. Fluids 18, 566 (1975).

6. LOWER HYBRID WAVE GROUP VELOCITY TRAJECTORIES IN TOROIDAL GEOMETRY

U.S. Energy Research and Development Administration (Contract E(11-1)-3070)

John L. Kulp, George L. Johnston, Abraham Bers

Introduction

An aspect of our investigation of RF heating of Tokamaks is the penetration of RF fields into an inhomogeneous plasma. The study of the propagation of lower hybrid waves excited by a localized source into a linear density gradient has been pursued by Briggs and Parker,[1] Simonutti,[2] Golant,[3] Bers, Karney, and Theilhaber,[4,5] and others.[6-8] In this report we describe a first step toward extending these previous results to a plasma model that includes three-dimensional effects such as toroidal magnetic field goemetry, temperature, current density and particle density profiles, and two-dimensional excitation structures. The questions that we address are: How is the wave propagation modified as compared with the two-dimensional models? and What is the spatial distribution of RF fields through the volume of the torus? The determination of the width of the region containing substantial RF fields is critical to the evaluation of various nonlinear heating schemes employing wave-wave interactions such as parametric downconversion to electrostatic ion cyclotron waves[9] or wave-particle effects (see Part II, Sec. XII-B. 2).

The simplest approach to these questions lies in the investigation of the trajectory of the group velocity of a wave excited by a source at the edge of the plasma. The two-dimensional theory predicts[1] that the electric field produced by a waveguide structure with appropriate orientation will become focused along rays described by the group velocity vector. We expect this result to remain true also in the three-dimensional plasma, since the local behavior of the wave is adequately described at any point by a two-dimensional model, as will be shown. Thus by observing the spatial separation of group velocity rays with wave numbers maximally separated in the accessible excited spectrum, we obtain an estimate of the spreading of the field structure. Spatial dispersion attributable to thermal effects still remains to be investigated.

Local Approximation

The approximation we invoke is that there exists a distance which, on the one hand, is small enough that plasma inhomogeneities can be neglected, yet is long compared with

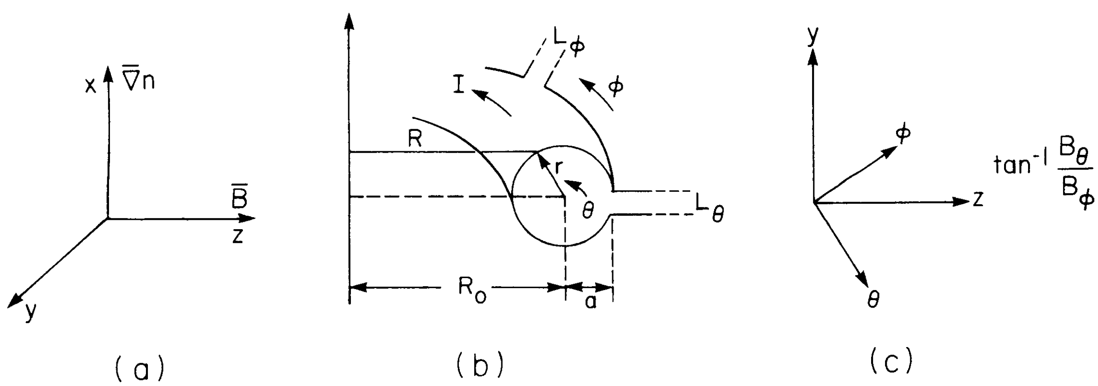

Fig. XII-32. (a) Local Cartesian coordinates.
(b) Toroidal coordinates.
(c) Two-dimensional coordinate transformation.

the distance over which the RF excitation oscillates. A linear homogeneous model of wave propagation is then applied within such a region. To be consistent, a necessary condition of this local approximation is that the wavelengths in the field spectrum be smaller than the typical scale length of the plasma inhomogeneities.

For a toroidal plasma, the magnetic field and plasma density inhomogeneities are most conveniently expressed in the toroidal coordinates r, θ, ϕ (Fig. XII-32). The local wave propagation, however, is easiest to describe in a coordinate system with one coordinate ($\hat{z}$) in the local direction of the magnetic field, $\hat{B}_o$. To facilitate transformations between these coordinate systems, $\hat{x}$ in the local system is chosen in the local direction of $\overline{\nabla}n$ and $\hat{y} = \hat{z} \times \hat{x}$.

To examine the validity of the local approximation we must perform the following steps:

1. Find the scale length of the inhomogeneities in the toroidal coordinate system.
2. Relate the toroidal scale lengths to scale lengths in the local coordinate system.
3. Compare the constraints on the wavelengths of the excitation due to linear wave propagation theory (accessibility, cutoff) and the source shape, with the condition that the wavelength must be shorter than the inhomogeneity scale length. For any plasma parameter f (e.g., density or magnetic field), we use the estimate

$$\frac{1}{f}\frac{\partial f}{\partial x_i} \approx \frac{\Delta f}{f_{ave}\Delta x_i} = \frac{f_{max} - f_{min}}{\frac{1}{2}(f_{max}+f_{min})}\frac{1}{\Delta x_i} \tag{1}$$

and assume the scale length to be $\left(\frac{1}{f}\frac{\partial f}{\partial x_i}\right)^{-1}$.

Constraints on λ_x. In the direction of $\overline{\nabla}n$, the magnetic field variation is of order B_θ/B so we neglect it and assume the scale length is $\left(\frac{1}{n}\frac{dn}{dr}\right)^{-1} \sim a$ where a is the minor radius of the torus. Since $\hat{x} = -\hat{r}$, the scale length in the local coordinate system is also a. Thus the scale length in the $\hat{x}$ direction imposes the condition $\lambda_x \ll a$. Now consider restrictions arising from the linear dispersion relation. Near the outside of the plasma there will be a cutoff layer where λ_x is imaginary. Thus the local description of the wave propagation can only be applied at some radius less than the cutoff layer. To see that the required distance beyond cutoff is small, note that near cutoff

$$\frac{\lambda_x}{\lambda_z} \sim \left(\frac{m_i}{m_e}\frac{2x}{a} - 1\right)^{-1/2} \tag{2}$$

where $\omega \approx \omega_{pi\,max}$ and a parabolic density profile have been assumed. If λ_z/a is not large (see below), λ_x/a will become small in a distance $\frac{m_e}{m_i}a$.

Constraints on λ_y. Neglecting B_θ/B_ϕ, $\hat{y}$ is essentially in the $\hat{\theta}$ direction. The inhomogeneity scale length in the $\hat{\theta}$ direction is $\left(\frac{1}{B}\frac{\partial B}{r\partial\theta}\right)^{-1} \approx a\frac{\pi}{2}\epsilon$ which imposes the condition $\lambda_y \ll a\frac{\pi}{2}\epsilon$, $\epsilon = \frac{a}{R_o}$. The spectrum excited by a rectangular waveguide provides another loose constraint on λ_y, since most of the power in the spectrum is found where $\lambda_y \gtrsim L_y/2$. L_y is the dimension of the waveguide in the $\hat{y}$ direction. Since $L_y/2 \ll a\frac{\pi}{2}\epsilon$, there is always a large range of the λ_y spectrum satisfying the scale-length constraint.

Constraint on λ_z. The scale length of the magnetic field variation along the direction of the magnetic field line is found by multiplying the result for the $\hat{y}$ direction by the ratio $\frac{B_\phi}{B_\theta} = q\epsilon$, giving $\lambda_z \ll a\frac{\pi}{2} q\epsilon^2$. This restriction must be compared to the accessibility condition for penetration to the center of the plasma,[3]

$$\lambda_z < \frac{2\pi c/\omega}{1 + \left.\frac{\omega_{pe}^2}{\omega_{ce}^2}\right|_{r=0}}. \tag{3}$$

For most Tokamak experiments and reactor designs,[4]

$$\frac{2\pi c/\omega}{1 + \left.\frac{\omega_{pe}^2}{\omega_{ce}^2}\right|_{r=0}} \ll a\frac{\pi}{2} q\epsilon^2 \tag{4}$$

so that accessibility is the more stringent condition.

The problem of describing the modification of the transverse (λ_y, λ_z) spectrum of the RF excitation as it penetrates from the waveguide source to a point beyond cutoff is now being investigated. Since we are starting our description of RF penetration beyond cutoff, we will assume that only the modification is due to the accessibility "filtering" described by Bers, Karney, and Theilhaber.[5]

Group Velocity Trajectories

The trajectory of the group velocity in three dimensions, $\bar{S}(\omega, \bar{k}, s)$, is found by integrating from some initial position $\bar{S}_o$ along a path L for a distance s,

$$\bar{S}(\omega, \bar{k}, s) - \bar{S}_o = \int_L d\bar{s}, \tag{5}$$

where L is specified by $\bar{v}_g(\omega, \bar{k}, \bar{r}) \times d\bar{s} = 0$. We are at liberty to specify the trajectory along a given orthogonal coordinate, since $\bar{v}_g \times d\bar{s} = 0$ provides only two independent constraints. Consider a straight line trajectory for the z-coordinate in a Cartesian coordinate system and $\bar{S}_o = 0$. Then Eq. 5 becomes

$$\bar{S}_c(\omega, \bar{k}, s) = \left[\int_{z_o}^{z} \frac{\partial x}{\partial z} dz,\ \int_{z_o}^{z} \frac{\partial y}{\partial z} dz,\ z - z_o\right]. \tag{6}$$

The derivatives $\frac{\partial x}{\partial z}, \frac{\partial y}{\partial z}$ are specified from $\overline{v}_g \times d\overline{s} = 0$,

$$\frac{\partial x}{\partial z} = \frac{v_{gx}}{v_{gz}} = \frac{\frac{\partial D}{\partial k_x}}{\frac{\partial D}{\partial k_z}}, \quad \frac{\partial y}{\partial z} = \frac{v_{gy}}{v_{gz}} = \frac{\frac{\partial D}{\partial k_y}}{\frac{\partial D}{\partial k_z}}. \tag{7}$$

In toroidal coordinates, we pick the path along the ϕ coordinate,

$$\overline{S}_T(\omega, \overline{k}, s) = \left[\int_{\phi_o}^{\phi} \frac{\partial r}{\partial \phi}\, d\phi,\ \int_{\phi_o}^{\phi} \frac{\partial \theta}{\partial \phi}\, d\phi,\ \phi - \phi_o\right]. \tag{8}$$

Since it is not convenient to compute $\overline{v}_g$ in toroidal coordinates, we use the transformations

$$\frac{\partial r}{\partial \phi} = \frac{\partial r}{\partial x} \frac{\partial x}{\partial z} \frac{\partial z}{\partial \phi}, \quad \frac{\partial \theta}{\partial \phi} = \frac{\partial \theta}{\partial y} \frac{\partial y}{\partial z} \frac{\partial z}{\partial \phi} + \frac{\partial \theta}{\partial z} \frac{\partial z}{\partial \phi}. \tag{9}$$

These derivatives are computed shortly.

A convenient method is required for computing the spatial dependence of $\overline{k}(\omega, \overline{r})$ without solving $D(\omega, \overline{k}, \overline{r}) = 0$. By assuming steady-state penetration of the wave, the constraint $D(\omega, \overline{k}, \overline{r}) = 0$ can be used[10] to show

$$\hat{v}_g \cdot \frac{\partial}{\partial \overline{r}} k = -p \frac{\frac{\partial D}{\partial \overline{r}}(\omega, \overline{k}, \overline{r})}{\left|\frac{\partial D}{\partial \overline{k}}(\omega, \overline{k}, \overline{r})\right|} \tag{10}$$

where p is the sign of $\frac{\partial D}{\partial \omega}$ and $\hat{v}_g$ is the unit vector in the direction of the group velocity. Then $\overline{k}$ is found from

$$\overline{k}(\omega, s) - \overline{k}_o(\omega) = \int_L d\overline{s} \cdot \frac{\partial}{\partial \overline{s}} \overline{k}. \tag{11}$$

Propagation of Lower Hybrid Waves: Cold-Plasma Model

For investigating the penetration of electrostatic waves in the regime $\omega_{ci} \ll \omega \ll \omega_{ce}$, we apply the general group velocity ray formulas to an electrostatic cold-plasma model. Using Theilhaber's results,[5] we find the electrostatic assumption valid for $\frac{\omega_{ci}}{\omega_{LH}} \ll \frac{\omega}{\omega_{LH\ max}} < 1.255$ and $n_z > 1 \rightarrow 1.35$ or $\frac{\omega_{ce}}{\omega_{LH}} \gg \frac{\omega}{\omega_{LH\ max}} > 1.255$ and $n_z > 1.35 \rightarrow 1.82$,

$n_z = \frac{k_z c}{\omega}$. For n_z not satisfying these constraints, either the wave will be reflected, or electromagnetic corrections to the dispersion relation will be required.

The electrostatic dispersion relation appropriate to the cold-plasma model is

$$D(\omega, \bar{k}) = \frac{c^2}{\omega^2} \left(k_x^2 K_\perp + k_y^2 K_\perp + k_z^2 K_{||} \right) = 0, \tag{12}$$

where $K_\perp$ is the perpendicular component of the dielectric tensor, and $K_{||}$ is the parallel component. By using this dispersion function, the derivatives describing the group velocity trajectory in the local coordinate system become

$$\frac{\partial y}{\partial z} = \frac{k_y}{k_z} \frac{K_\perp}{K_{||}}, \qquad \frac{\partial x}{\partial z} = \pm \frac{K_\perp}{K_{||}} \left(\frac{-K_{||}}{K_\perp} - \frac{k_y^2}{k_z^2} \right)^{1/2}. \tag{13}$$

The dielectric tensor components for $\omega_{ci} \ll \omega \ll \omega_{ce}$ are

$$K_\perp = 1 - \frac{\omega_{pi}^2}{\omega^2} + \frac{\omega_{pe}^2}{\omega_{ce}^2} \tag{14}$$

$$K_{||} = 1 - \frac{\omega_{pe}^2}{\omega^2}. \tag{15}$$

It is useful to note that $\partial y/\partial z$ and $\partial x/\partial z$ depend only on wave number through k_y/k_z, since $K_\perp$ and $K_{||}$ are independent of $\bar{k}$. For a warm-plasma model we would also expect a dependence on $k_z \lambda_{De}$. Electromagnetic corrections would introduce a $k_z c/\omega$ dependence. The variation of $\bar{k}$ along the ray will be computed in the sequel.

Magnetic Field Geometry

While the local coordinate system is the most convenient one for computing $D(\omega, \bar{k})$ and its derivatives, it is most useful to plot the group velocity trajectory in the coordinate system of a Tokamak device. Furthermore, the magnetic field amplitude and plasma density are easiest to compute in toroidal coordinates. This coordinate system is shown in Fig. XII-32b. The toroidal magnetic field $B_\phi(r, \theta)$ is assumed to be uniform in ϕ,

$$B_\phi(r, \theta) = B_{\phi o} \frac{R_o}{R} = \frac{B_{\phi o}}{1 + \frac{r}{R_o} \cos \theta}. \tag{16}$$

Neglecting displacement of the plasma from the center of flux surfaces, we compute the poloidal magnetic field as

$$B_\theta(r) = -\frac{\mu_o I(r)}{2\pi r}$$

$$I(r) = 2\pi \int_0^r J_\phi(r')\, r'dr'. \tag{17}$$

Let $B_{\theta o} = \frac{\mu_o I(a)}{2\pi a}$, then

$$B_\theta(r) = -B_{\theta o}\frac{a}{r}\int_0^{r/a} f_J(x)\, x\, dx. \tag{18}$$

We shall consider a current profile typical of the high-density operation of Alcator[11]

$$f_J(x) = \frac{35}{4}\,(1-x\alpha_c)^{3/2}, \qquad \alpha_c = \frac{a}{a_c}. \tag{19}$$

This profile is obtained by assuming $J_\phi \sim T_e^{3/2}$ and using experimental electron temperature data. We define the safety factor

$$q(r,\theta) = \frac{B_\phi(r,\theta)\, r}{|B_\theta(r)|\, R(r,\theta)} = \frac{q_o \alpha^2 \frac{r}{a}}{-f_\theta\left(\frac{r}{a}\right)\left(\alpha + \frac{r}{a}\cos\theta\right)^2}$$

$$q_o = \frac{B_{\phi o} a}{B_{\theta o} R_o}, \qquad \alpha = \frac{R_o}{a}$$

$$f_\theta\left(\frac{r}{a}\right) = \frac{B_\theta(r)}{B_{\theta o}}. \tag{20}$$

<u>Coordinate Transformations</u>

We shall now present the coordinate transformations required to relate the displacements along the direction of the group velocity that is computed in the local Cartesian coordinate system to toroidal coordinates of the plasma. These transformations are also used to relate successive local coordinate systems whose orientations change with the curving of magnetic field lines. By assuming that the density gradient is in the direction of the minor radius and flux surfaces are normal to the density gradient, the coordinate transformation becomes two-dimensional because $\hat{r} = -\hat{x}$ (see Fig. XII-32c). In the plane perpendicular to $\hat{r}$, unit vectors $\hat{e} = [e_x, e_y, e_z]$, $[e_r, e_\theta, e_\phi]$ transform as follows:

$$\begin{bmatrix} e_y \\ e_z \end{bmatrix} = \frac{1}{\left(1 + f_b^2(r,\theta)\right)^{1/2}} \begin{bmatrix} 1 & f_b(r,\theta) \\ -f_b(r,\theta) & 1 \end{bmatrix} \cdot \begin{bmatrix} e_\theta \\ e_\phi \end{bmatrix}$$

$$f_b(r,\theta) = -\frac{B_\theta(r)}{B_\phi(r,\theta)} = -\frac{f_\theta\left(\frac{r}{a}\right) R(r,\theta)}{q_o \alpha R_o}. \tag{21}$$

The coordinate transformation equations above can be used to compute the derivatives describing the change of variables in the integrations defining $\overline{S}(\omega, \overline{k}, s)$.

$$\frac{\partial z}{\partial \phi} = \frac{\left(1 + f_b^2(r,\theta)\right)^{1/2}}{1 + f_b(r,\theta)\frac{\partial y}{\partial z}} R(r,\theta)$$

$$\frac{\partial \theta}{\partial \phi} = \frac{\frac{\partial y}{\partial z} - f_b(r,\theta)}{1 + f_b(r,\theta)\frac{\partial y}{\partial z}} \frac{R(r,\theta)}{r}$$

$$\frac{\partial r}{\partial x} = -1. \tag{22}$$

The use of these formulas in computing the rays will be discussed in the sequel. We shall return to these expressions to explain the observed behavior of the rays.

Another transformation between two local coordinate systems at adjacent points on the ray is required. With such a transformation, k_y/k_z at r', θ' can be found from

$$\frac{k_y'}{k_z'} = \frac{\left(\frac{k_y}{k_z} - f_b(r,\theta)\right)\frac{r}{r'} + f_b(r',\theta')\left(f_b(r,\theta)\frac{k_y}{k_z} + 1\right)\frac{R}{R'}}{-f_b(r',\theta')\left(\frac{k_y}{k_z} - f_b(r,\theta)\right)\frac{r}{r'} + \left(f_b(r,\theta)\frac{k_y}{k_z} + 1\right)\frac{R}{R'}}. \tag{23}$$

Variation of $\overline{k}$ along the Group Velocity Ray

The variation of $\overline{k}$ along the ray for an electrostatic cold-plasma model is found by applying Eq. 10 with $p = 1$. Thus

$$\left|\frac{\partial D}{\partial \bar{k}}(\omega, \bar{k})\right| = \frac{2c^2}{\omega^2}\left|k_z K_{\|}\right|\left(1+\frac{K_{\perp}}{-K_{\|}}\right)^{1/2}. \tag{24}$$

Using an expression for $\frac{\partial D}{\partial \bar{r}}(\omega, \bar{k})$ derived for a cold plasma, we can show that

$$\frac{1}{k_z}\frac{\partial k_z}{\partial s} = \frac{\hat{v}_g \cdot \bar{\nabla} k_z}{k_z}$$

$$= \frac{|k_z|}{k_z}\frac{\omega_{pe}^2}{\omega_{ce}^2}\frac{-f_b}{\left(1+f_b^2\right)^{3/2}}\frac{1}{K_{\perp}\left(1+\frac{K_{\perp}}{-K_{\|}}\right)^{1/2}}\frac{\sin\theta}{R}$$

and

$$\frac{\frac{\partial k_y}{\partial s}}{\frac{\partial k_z}{\partial s}} = -\frac{1}{f_b}. \tag{25}$$

Equations 23 and 25 are sufficient for describing the evolution of k_y/k_z from point to point along the ray.

Computation and Display of the Group Velocity Trajectories

The computational scheme for obtaining the group velocity trajectories has the following parts:

Boundary conditions – starting the ray

Recursion formulas for stepping along the ray

Singular points – resonance, cutoff, $r = 0$

Implementation and display of the trajectory.

a. Boundary Conditions

At the edge of the plasma a waveguide excites a plasma response with a k_θ, k_ϕ spectrum determined by the dimensions of the waveguide. We assume a rectangular waveguide with dimensions L_θ, L_ϕ. Then the spectrum is roughly bounded from above by $k_\theta \sim \frac{\pi}{L_\theta}$, $k_\phi \sim \frac{\pi}{L_\phi}$. We have mentioned how this response couples through to the cutoff layer where $\omega = \omega_{pe\ local}$. For our purposes, we assume that the spectrum reaches the cutoff layer essentially unmodified except for the restrictions of the accessibility conditions. This assumption is reasonable, since the distance to the cutoff layer is small, $\sim a(m_e/m_i)^{1/2}$. The conclusive solution to this question rests on the calculation of the RF coupling problem.[12] Any error introduced here will not strongly affect our results, since the correction is small and the dependence of the group velocity on k_y/k_z is weak except near r = 0, as we shall show.

Our initial values of k_θ and k_ϕ at the cutoff layer are transformed into the local coordinate system at that point to provide an initial k_y and k_z. Subsequently, we need only compute k_y/k_z in each successive local coordinate system. The starting point of the group velocity ray is given by $r_{cutoff}, \theta_o, \phi_o$, where θ_o and ϕ_o are chosen to correspond to a point at the edge of the exciting structure from which we wish to trace the group velocity of the wave. For finite k_y/k_z, the cutoff distance is found by solving

$$\frac{k_x^2}{k_z^2} = -\frac{k_y^2}{k_z^2} - \frac{K_{\parallel}}{K_{\perp}} = 0, \tag{26}$$

which yields

$$\frac{r_{cutoff}}{a} = \sqrt{1 - \frac{\omega^2}{\omega_{pe\,max}^2}\left(1 + \frac{k_y^2}{k_z^2}\right)} \tag{27}$$

where the loose restriction $\frac{k_y}{k_z} < \sqrt{\frac{m_i}{m_e}}$ has been assumed.

b. Recursion Formula

Suppose k_y/k_z for a wave of interest is known at a point r, θ, ϕ. Assume that we are tracing out the trajectory by stepping around the torus in increments of $\Delta\phi$. Then Eqs. 22 tell us how to compute Δz, Δy, and Δx, and finally $\Delta\theta$ and Δr. To do this we must first compute $f_b(r,\theta)$ (Eq. 21) and $-K_{\parallel}/K_{\perp}$ (Eqs. 14,15). These require in turn computing $f_n(r)$ and $f_\theta(r)$. Once these are computed, we move to a new point on the ray by $r' \leftarrow r + \Delta r$, $\theta' \leftarrow \theta + \Delta\theta$, $\phi' \leftarrow \phi + \Delta\phi$. But before we can continue at this point, we must find k'_y/k'_z. This is accomplished by computing $\Delta k_z/k_z$ at r, θ, ϕ with the use of Eq. 25, and then computing k_y/k_z at r', θ', ϕ' in the coordinate system of r, θ, ϕ. Finally, k_y/k_z is expressed in the new local coordinate system at r', θ', ϕ' with the use of Eq. 23.

c. Singular Points

Several singularities occur in this calculation. First, when the quantity $\frac{-K_{\parallel}}{K_{\perp}} - \frac{k_y^2}{k_z^2}$ becomes negative imaginary terms are produced in Eqs. 13 and 22. This happens at the cutoff layer. This problem can be circumvented at the beginning of the ray by a judicious choice of starting point. As the ray eventually continues through the center of the plasma and comes out toward the edge, however, the cutoff layer will again be encountered. Exactly what happens there is not known, but we make the assumption that because the layer is small most of the energy of the wave tunnels out to the wall and an unimportant amount is reflected back into the plasma. Thus we simply terminate the calculation of the ray at this point.

Another singularity occurs when $K_\perp = 0$. This is the point in the plasma where $\omega = \omega_{LH}(r,\theta)$ (Fig. XII-33). Here the group velocity is 0 and Δk_z is infinite. This resonance is a result of our cold-plasma assumption. A treatment including thermal effects would predict a turning of the wave at a density less than that where $\omega = \omega_{LH}$. We hope

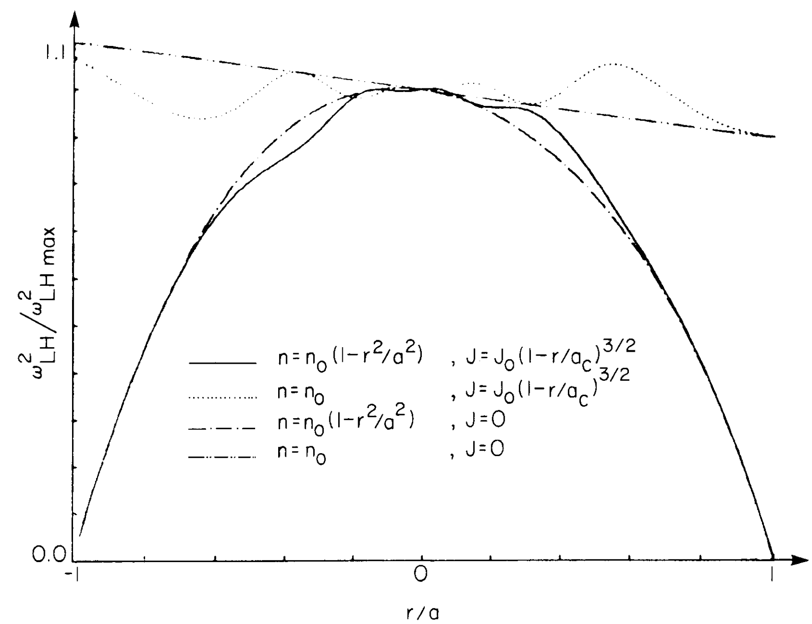

Fig. XII-33. Profile of the local value of the lower hybrid frequency.

to pursue this in future work, but at present we must stop the calculation at this point because the cold-plasma model is insufficient for describing further development of the group velocity ray.

The "singularity" at $r = 0$ is not a real but rather a computational singularity. Since the magnetic field and density are smoothly varying at $r = 0$, the ray is also expected to behave undramatically there. Equation 22 shows, however, that at $r \to 0$, $r\Delta\theta$ remains finite which implies $\Delta\theta \to \infty$. But $r\,\Delta\theta \sim \Delta\phi$ so that by defining $\Delta\phi$ to vary with r we can keep $\Delta\theta$ arbitrarily small (this can be shown to be convergent). Some problems may enter in computing $I(r)$ near $r = 0$ because of its $1/r$ dependence. Fortunately, this dependence is often canceled analytically by the r dependence of $f_\theta(r)$.

d. Implementation

The control structure (order of computation) of the ray calculation is rather complex. It is worthy of note that a remarkably simple method of specifying and executing this calculation was made possible by using the MACSYMA system.[13] The mechanism is called the associated array function. The details of the implementation of this calculation will be provided in a forthcoming M. I. T. Plasma Research Report. We note that k_x was not explicitly calculated in this scheme. To compare the variation of k_x, as the ray moves through the density gradient between two- and three-dimensional models, we use the

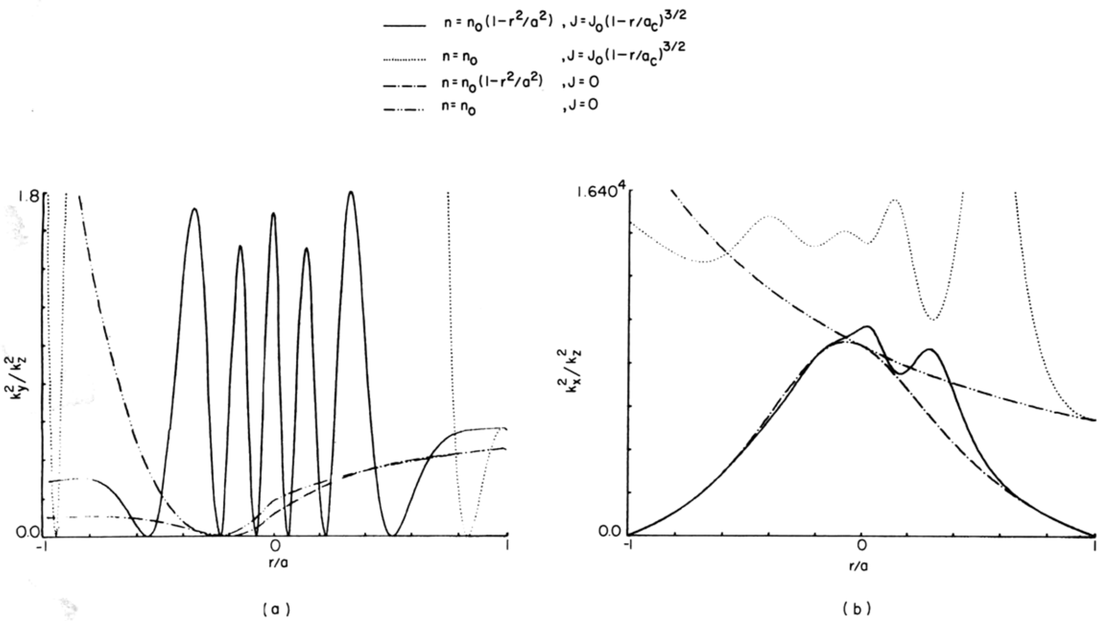

Fig. XII-34. (a) Azimuthal wave number vs radius. (b) Wave number in the direction of the density gradient vs radius.

computed values of k_y^2/k_z^2 (Fig. XII-34a) and $-K_{\parallel}/K_{\perp}$ to find k_x^2/k_z^2 from $(k_x^2+k_y^2)\ K_{\perp} + k_z^2K_{\parallel} = 0$ (Fig. XII-34b).

The group velocity trajectory is displayed by plotting two projections (Figs. XII-35 through XII-37). A projection into a minor cross-section plane is obtained by plotting $r \cos \theta$, $r \sin \theta$ along the ray. This is displayed in the center of the figures. The outer ring is a top view of the torus, plotting $R \cos \phi$, $R \sin \phi$ along the ray.

<u>Interpretation of the Computed Rays</u>

The parameters required to specify a group velocity ray in a cold toroidal plasma are the following.

Magnetic Field Geometry

α — aspect ratio R_o/a

q_o — safety factor $\dfrac{B_\phi(R_o)\, a}{B_\theta(a)\, R_o}$

Plasma Profiles

$f_n(r)$ — particle density $\dfrac{n(r)}{n(\phi)}$

$f_\theta(r)$ — integrated current density $\dfrac{B_\theta(r)}{B_\theta(a)}$

Plasma Parameter

$\left.\dfrac{\omega_{ce}^2}{\omega_{pe}^2}\right|_{r=0}$ — cold-plasma parameter. Essentially normalizes $f_n(r)$ and $f_\theta(r)$.

Source Spectrum

$\dfrac{\omega}{\omega_{LH_{max}}}$ — normalized frequency

$\dfrac{m}{n}$ — ratio of toroidal mode numbers

$$\left.\frac{k_\theta}{k_\phi}\right|_{r=a} = \frac{m/a}{n/(R_o+a)} = \frac{L_\phi}{L_\theta}$$

$$\frac{m}{n} = \frac{L_\phi/(R_o+a)}{L_\theta/a} = \frac{a}{R_o+a}\,\frac{k_\theta}{k_\phi}$$

We have not exhaustively explored this parameter space. The most interesting changes in the properties of the ray are seen by varying profiles and source frequency. In Fig. XII-35, we use parameters that are typical of the high-density regime of Alcator[11] and vary the frequency from less than $\omega_{LH_{max}}$ to several times it. Next, Fig. XII-36 shows the effect of varying current and density profiles with $\omega = 1.1\,\omega_{LH_{max}}$. The effect of finite source width is shown in Fig. XII-37 where two rays are plotted from the edges of the waveguide source.

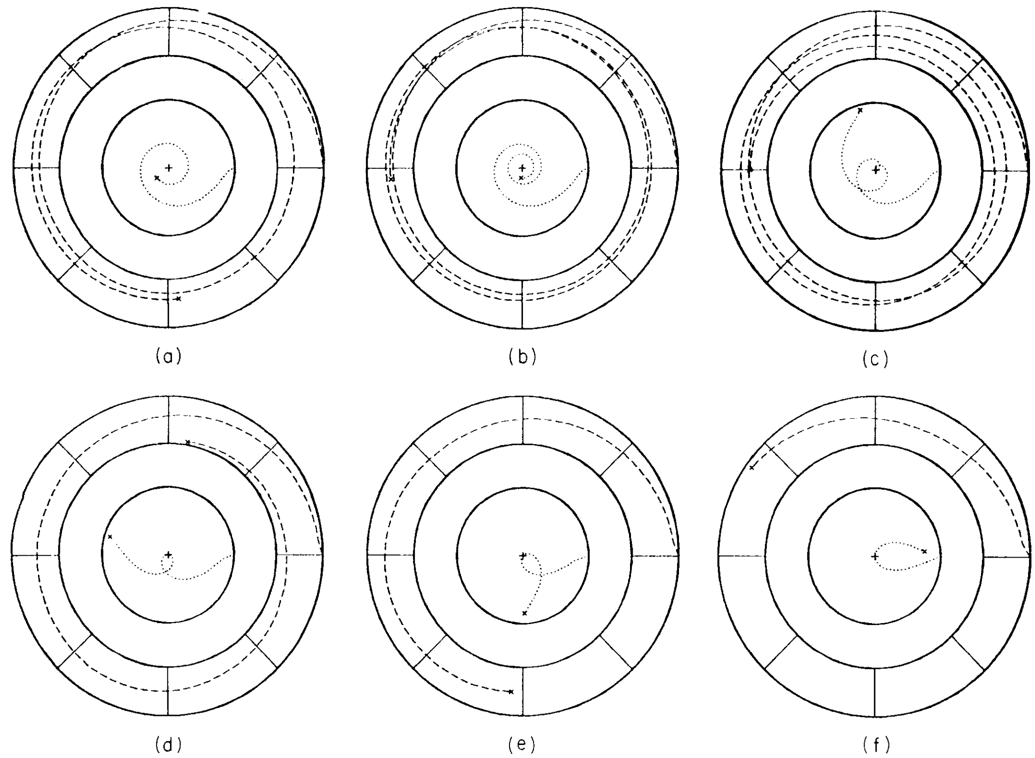

Fig. XII-35. Group velocity ray trajectories for varying source frequencies.

Parameters: $\frac{\omega_{ce}^2}{\omega_{pe}^2} = 2.5$, $\frac{R_o}{a} = 5.68$, $q_o = 4.19$

(a) $\frac{\omega}{\omega_{LH\,max}} = 0.99$ (b) $\frac{\omega}{\omega_{LH\,max}} = 0.995$ (c) $\frac{\omega}{\omega_{LH\,max}} = 1.2$

(d) $\frac{\omega}{\omega_{LH\,max}} = 1.8$ (e) $\frac{\omega}{\omega_{LH\,max}} = 2.5$ (f) $\frac{\omega}{\omega_{LH\,max}} = 4.0$

The group velocity ray trajectory can be characterized by the relative rates of displacement in the radial ($\hat{r}$), azimuthal ($\hat{\theta}$), and toroidal ($\hat{\phi}$) directions as a function of distance along the ray (s). For a given plasma model, these rates are easily computed in the local coordinate system (Eq. 13). Thus

$$\frac{\partial r}{\partial s} = -\frac{\partial x}{\partial z}\frac{\partial z}{\partial s}$$

$$\frac{\partial \theta}{\partial s} = \frac{\partial \theta}{\partial z}\frac{\partial z}{\partial s} + \frac{\partial \theta}{\partial y}\frac{\partial y}{\partial z}\frac{\partial z}{\partial s}$$

$$\frac{\partial \phi}{\partial s} = \frac{\partial \phi}{\partial z}\frac{\partial z}{\partial s} + \frac{\partial \phi}{\partial y}\frac{\partial y}{\partial z}\frac{\partial z}{\partial s}. \tag{28}$$

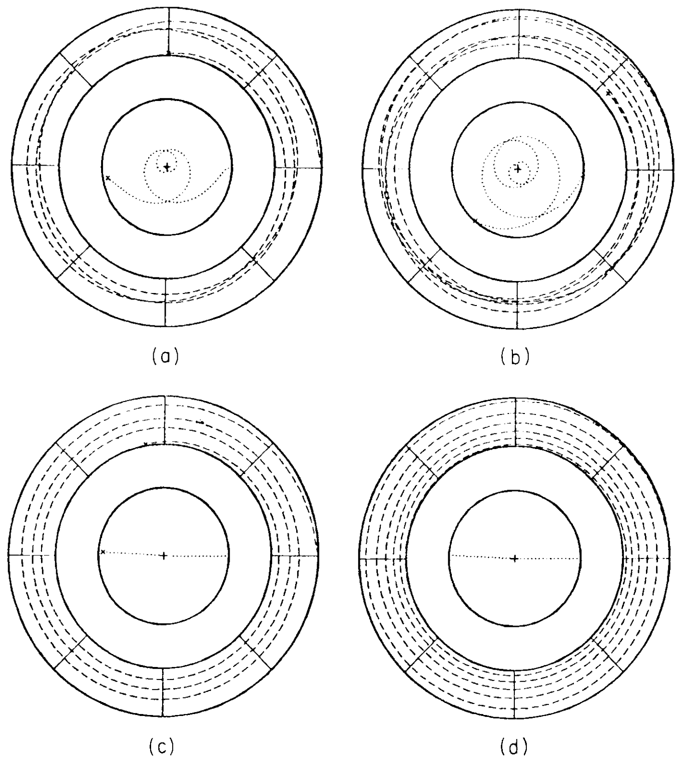

Fig. XII-36. Group velocity ray trajectories varying current and density profiles. $\dfrac{\omega}{\omega_{LH\ max}} = 1.1.$

(a) $n = \left(1 - \dfrac{r^2}{a^2}\right), \quad J \sim \left(1 - \dfrac{r}{a_c}\right)^{3/2}$

$a_c = 8.0$

(b) $n = \text{constant}, \quad J \sim \left(1 - \dfrac{r}{a_c}\right)^{3/2}$

(c) $n = \left(1 - \dfrac{r^2}{a^2}\right), \quad J = 0$

(d) $n = \text{constant}, \quad J = 0$

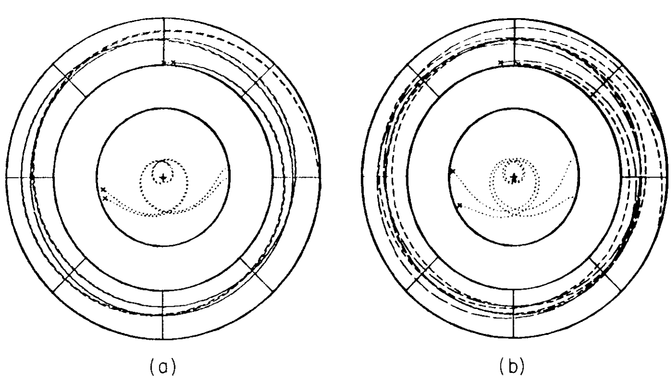

Fig. XII-37.

Group velocity ray trajectories from spatially separated starting points.
(a) Azimuthal (θ) separation. $\Delta\theta = .15$.
(b) Toroidal (ϕ) separation. $\Delta\phi = .08$.

By using (13) and (22), it is now straightforward to make relative comparisons of displacement rates. Several qualitative observations can be explained with the use of these relations.

1. The radial rate of ray penetration depends strongly on the source frequency ω.

2. With a monotonically decreasing current profile and source frequencies near $\omega_{LH\,max}$, the rates of penetration can be ordered:

$$R\frac{\partial\phi}{\partial s} \gg r\frac{\partial\theta}{\partial s} > \frac{\partial r}{\partial s}.$$

3. The presence of a density gradient causes more rapid penetration.

4. The ray trajectory depends weakly on the shape of the waveguide, as reflected in the ratio (k_y/k_z). This ratio does not attain values much greater than 1.

5. Rays originating at spatially separated points become focused (Fig. XII-37).

6. The θ dependence of the ray is directly related to the shape of the current density profile, as is manifest through $B_\theta(r)$.

To apply Eq. 13 to Eq. 28, approximate expressions for $K_\parallel$ and $K_\perp$ are needed. Beyond cutoff, $-K_\parallel \approx \frac{m_i}{m_e}\frac{f_{n(r)}C_p}{f^2}$, where $f_n(r) = \frac{n(r)}{n_o}$, $f = \frac{\omega}{\omega_{LH\,max}}$, and $C_p = 1 + \left.\frac{\omega_{pe}^2}{\omega_{ce}^2}\right|_{max}$. Similarly, $K_\perp$ can be written

$$K_\perp \approx 1 - \frac{f_n(r)\,C_p}{f^2} + \left.\frac{\omega_{pe}^2}{\omega_{ce}^2}\right|_{max}\frac{f_n(r)}{f_B^2(r,\theta)}, \tag{29}$$

where $f_B(r,\theta) = \frac{\omega_{ce}}{\omega_{ce\,max}}$ and C_p is typically between 1 and 2. If we assume $f_B \sim 1$ by expanding to lowest order in B_θ/B, we find

$$\frac{K_\perp}{-K_\parallel} = \frac{m_e}{m_i}\frac{1}{C_p}\left[\frac{f^2}{f_n(r)} + \left.\frac{\omega_{pe}^2}{\omega_{ce}^2}\right|_{max} f^2 - C_p\right]. \tag{30}$$

When we let $\frac{k_y}{k_z} \ll \left(\frac{m_i}{m_e}\right)^{1/2}$, which is consistent with our observations, and consider the regime $\left[\frac{1}{f_n(r)} + \left.\frac{\omega_{pe}^2}{\omega_{ce}^2}\right|_{max} - \frac{C_p}{f^2}\right]^{1/2} \ll \frac{m_i}{m_e}$, (28) becomes

$$\frac{\partial r}{\partial s} \approx f\left(\frac{m_e}{m_i}\frac{1}{C_p}\right)^{1/2}\left[\frac{1}{f_n(r)} + C_p\left(1 - \frac{1}{f^2}\right) - 1\right]^{1/2}\frac{\partial z}{\partial s} \tag{31}$$

$$\frac{\partial\theta}{\partial s} \approx -\left\{\frac{1}{r}\frac{k_y}{k_z}f^2\frac{m_e}{m_i}\frac{1}{C_p}\left[\frac{1}{f_n(r)}+C_p\left(1-\frac{1}{f^2}\right)-1\right]+\frac{f_b(r,\theta)}{r}\right\}\frac{\partial z}{\partial s} \tag{32}$$

$$\frac{\partial\phi}{\partial s} \approx \frac{1}{R(r,\theta)}\frac{\partial z}{\partial s}. \tag{33}$$

These expressions show us that to lowest order in f_b

1. The radial penetration rate is essentially two-dimensional in that it is independent of the azimuthal coordinate θ.

2. The three-dimensional effects enter primarily because of the magnetic field geometry; that is, the dominant f_b/r dependence in $\partial\theta/\partial s$ and the $1/R$ dependence of $\partial\phi/\partial s$. A corollary to this is that the ratio of toroidal-to-azimuthal displacement is given by the local value of $q(r,\theta)$.

Our previous observations can now be explained by using (31)-(33).

1. For $f_n(r) \sim 1$ (near the center of the plasma) and $f > 1$, $\frac{\partial r}{\partial s} \sim f\left(\frac{m_e}{m_i}\right)^{1/2}\frac{\partial z}{\partial s}$. This is the result of Briggs and Parker.[1] Note the relatively strong dependence of $\partial r/\partial s$ on f as compared with the f dependence of $\partial\theta/\partial s$ or $\partial\phi/\partial s$.

2. The orderings are evident for $f \sim 1$:

$$R\frac{\partial\phi}{\partial s} \sim \frac{\partial z}{\partial s}$$

$$r\frac{\partial\theta}{\partial s} \sim -f_b$$

$$\frac{\partial r}{\partial s} \sim \left(\frac{m_e}{m_iC_p}\right)^{1/2} < f_b.$$

3. The radial and azimuthal penetration rates are significantly enhanced when $f_n(r) \ll 1$.

4. k_y/k_z enters weighted only by $\left(\frac{m_e}{m_i}\right)^{1/2}$, so if k_y/k_z is not large, its effect on the ray will be small. The variations of k_y/k_z along the ray can be seen from (25). This variation can only be strong for $f < 1$ and $K_\perp \approx 0$, i.e., near lower hybrid resonance. This can occur at several points along the ray, as shown in Fig. XII-38. As we have mentioned, the cold plasma model breaks down at these points and thermal corrections are necessary to describe the ray behavior accurately.

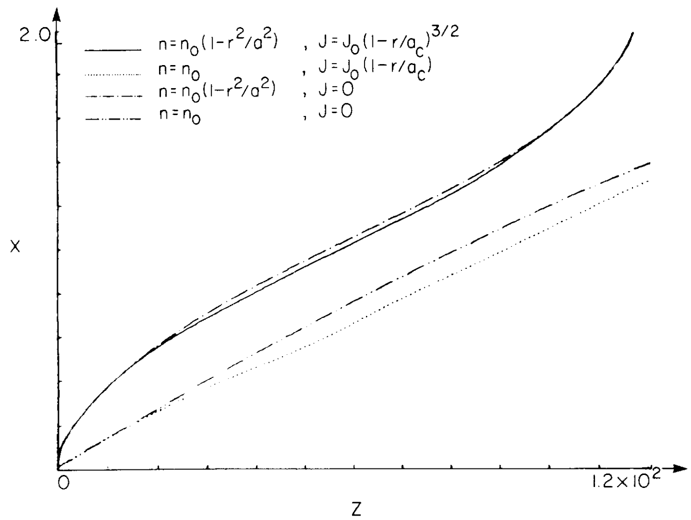

Fig. XII-38. Group velocity ray trajectories projected into the x-z plane of the local coordinate system.

To summarize, the relative toroidal vs radial penetration rate is approximately

$$\frac{\dfrac{\partial r}{\partial s}}{R\,\dfrac{\partial \phi}{\partial s}} \approx f\left(\frac{m_e}{m_i}\,\frac{1}{C_p}\right)^{1/2} \tag{34}$$

while the relative azimuthal vs radial rate is

$$\frac{\dfrac{\partial r}{\partial s}}{r\,\dfrac{\partial \theta}{\partial s}} \approx \frac{1}{f_b}\left(\frac{m_e}{m_i}\,\frac{1}{C_p}\right)^{1/2} \tag{35}$$

and

$$\frac{\dfrac{\partial \theta}{\partial s}}{\dfrac{\partial \phi}{\partial s}} \approx q(r, \theta). \tag{36}$$

Conclusion

The new results obtained in our investigation thus far include:

1. A computational scheme for group velocity ray tracing in three dimensions has been developed for Tokamak plasmas.

2. The penetration of the ray depends strongly on the frequency of the source but

weakly on the shape. Rays starting from displaced positions at the outside of the plasma tend to be focused.

3. The azimuthal dependence of the ray is determined primarily by the poloidal magnetic field, and thus the distribution of the ray through the volume of the torus is affected by the current profile.

We plan to include the effect of finite temperature and temperature profiles in future work. The purpose of this extension is to determine the modification of the ray by spatial dispersion and to clarify the effect of the wave-number spectrum of the source as the ray reaches the linear mode conversion turning point.[2] Recent results also indicate that electromagnetic corrections may also be important.

References

1. R. J. Briggs and R. R. Parker, "Transport of RF Energy to the Lower Hybrid Resonance in an Inhomogeneous Plasma," Phys. Rev. Letters 29, 852 (1972).
2. M. D. Simonutti, Ph.D. Thesis, Department of Electrical Engineering, M.I.T., 1971.
3. V. E. Golant, Sov. Phys. – Tech. Phys. 1, 1980 (1972).
4. A. Bers and C. F. F. Karney, "Study of the Feasibility of Heating a Tokamak Plasma by Parametric Decay of Low-Frequency Electron Plasma Waves," Quarterly Progress Report No. 114, Research Laboratory of Electronics, M.I.T., July 15, 1974, pp. 123-131.
5. A. Bers, C. F. F. Karney, and K. Theilhaber, "Whistler Wave Excitation and Its Parametric Down-Conversion to Electrostatic Ion Cyclotron Waves," Progress Report No. 115, Research Laboratory of Electronics, M.I.T., January 1975, pp. 184-204.
6. T. H. Stix, "Radiation and Absorption via Mode Conversion in an Inhomogeneous Collision-free Plasma," Phys. Rev. Letters 15, 878 (1965).
7. R. K. Fisher and R. Gould, Phys. Fluids 14, 857 (1971).
8. U. M. Glagoiev, "Propagation and Absorption of Hybrid Waves in a Weakly Inhomogeneous Plasma Layer," Plasma Phys. 14, 301 (1972).
9. C. F. F. Karney and A. Bers, "Parametric Excitation of Ion Waves by Resonance Cone Fields near the Lower Hybrid Frequency," Quarterly Progress Report No. 113, Research Laboratory of Electronics, M.I.T., April 15, 1974, pp. 105-112.
10. A. Bers, "Linear Waves and Instabilities," in Plasma Physics (Gordon and Breach Science Publishers, New York, London, Paris, 1975); also M.I.T. Plasma Research Report 7210, July 1972.
11. G. J. Boxman et al., "Low and High Density Operation of Alcator," a paper presented at the VIIth European Conference on Plasma Physics, Lausanne, Switzerland, September 1-5, 1975.
12. K. S. Theilhaber and A. Bers, "Whistler Wave Field Structure inside a Linear Density Profile," Progress Report No. 116, Research Laboratory of Electronics, M.I.T., July 1975, pp. 117-128.
13. MACSYMA Reference Manual, The Mathlab Group, Project MAC, M.I.T., November 1975.

Research — Experimental

7. PRELIMINARY RESULTS ON THE VERSATOR TOKAMAK

U.S. Energy Research and Development Administration (Contract E(11-1)-3070)

David S. Stone, Alan S. Fisher, Burton Richards

The Versator Tokamak, designed originally by Robert J. Taylor and constructed under his close supervision, was moved, in July 1974, from the Francis Bitter National Magnet Laboratory to the Research Laboratory of Electronics. A photograph of Versator in its new surroundings is shown in Fig. XII-39.

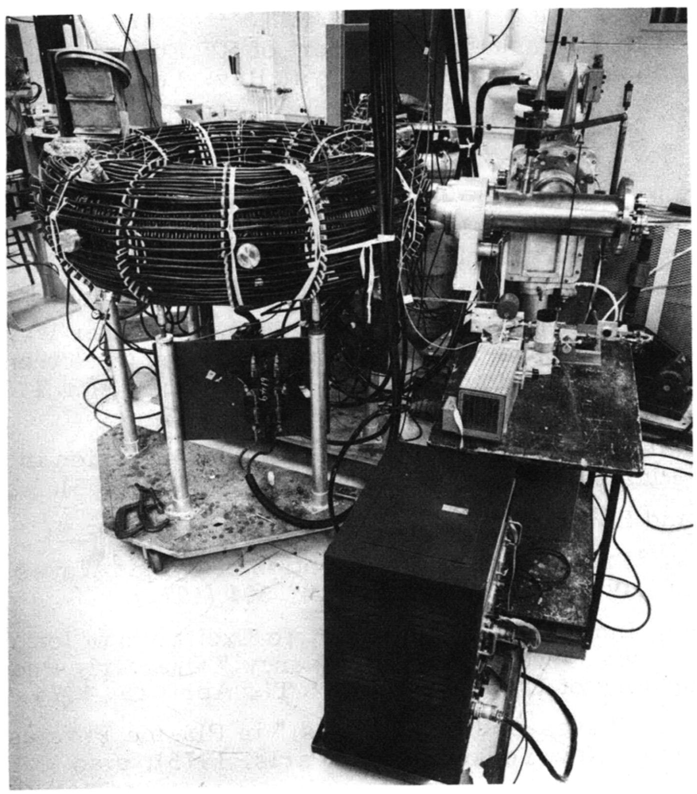

Fig. XII-39. Versator Tokamak in new location.

Construction of Electrical Systems

At the time of the move most of Versator's power systems and peripherals were preempted by the Rector Tokamak project at the Francis Bitter National Magnet Laboratory. During the summer of 1974, magnetic field coils were rewound on Versator and construction of new power supplies and electronics apparatus began. Capacitor banks for toroidal field [low- and high-voltage ohmic heating (OH)] and for vertical field were assembled. A 30-kHz preionization oscillator was built. Appropriate sequencing and triggering electronics equipment was also prepared. After some testing, the OH capacitor banks were enlarged and their triggering electronics was improved. All of this work was completed by July 1975.

Capacitor Switching and Dumping

The timing of the discharging of various capacitor banks during each "shot" is controlled by a sequencing board as shown schematically in Fig. XII-40. For typical discharge conditions the main field bank and 30-kHz preionization oscillator are triggered at time t = 0. As the main field bank discharges, current is driven through the main field and horizontal field coils. While the toroidal magnetic field builds up, the oscillator breaks down the hydrogen in the machine to approximately .1% ionization. At time t = 5 ms the high-voltage OH pulse is applied to the OH transformer. This completes the ionization and starts up the plasma current. When the high-voltage pulse level falls below the voltage on the low-voltage OH bank (after ~1 ms), the latter is triggered automatically. The energy in the low-voltage bank is then discharged into the OH coils,

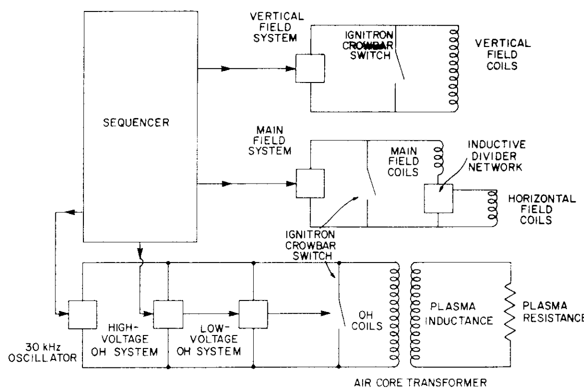

Fig. XII-40. Versator electrical systems.

and the plasma current rises gradually, accompanied by rapid collisional plasma heating. The plasma current finally subsides as the energy stored in the low-voltage OH bank is exhausted. A small vertical field is also needed during the plasma current pulse to prevent radial expansion of the plasma current loop. The vertical field capacitor bank is normally sequenced to be discharged into the vertical field coils concurrently with the discharge of the OH banks, as the vertical field must be roughly proportional to the plasma current.

Rudimentary measurements have permitted us to compose a preliminary list of parameters.

Table XII-4. Versator parameters.

Operating Parameters	
Major radius	54 cm
Minor radius	14 cm
High-voltage OH bank	7 kV, 188 μF, 4.6 kJ
Low-voltage OH bank	825 V, 40,000 μF, 13.6 kJ
Main field bank	4 kV, 5,000 μF, 40 kJ
Maximum main field	5.9 kG
Preliminary Plasma Parameters	
Density	10^{12}-10^{13} cm^{-3}
Electron temperature*	up to ~120 eV
Plasma current	up to 5 kA
Current pulse length	8-11 ms
Energy confinement time	0.4-1.6 ms
Beta poloidal	approximately 1.0

*Electron temperature averaged over the plasma current cross section derived from the Spitzer conductivity, under the assumption Z = 3.

Diagnostics

On Versator, at present, the following diagnostics are operational:

1. Hard x-ray detector
2. Visible spectrometer
3. Double Langmuir probe
4. 8-mm microwave interferometer
5. Inductive diagnostics

Further diagnostics that will be added are as follows:

6. Soft x-ray bremsstrahlung diagnostics (January 1976)
7. Laser Thomson scattering (February 1976)
8. UV vacuum spectrometer (July 1976)
9. Charge exchange cell (Middle of 1976)

Discussion of Preliminary Results

During September and October 1975 we concentrated on improving the length of the Versator discharge current pulse. A typical current pulse obtained shortly after the electrical systems were completed in July 1975, is shown in Fig. XII-41. Note that the length of the pulse is ~1.5 ms. This current oscillogram indicates that a strong quenching of the discharge was occurring even before the low-voltage ohmic heating (OH) pulse was applied to the plasma column. We used two approaches to improve the length of the discharge current pulse.

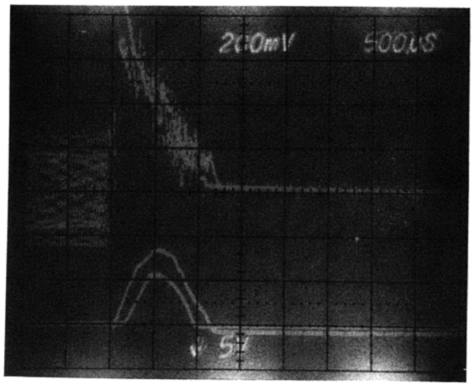

Fig. XII-41.

Typical early plasma currents and loop voltages vs time. Rapid quenching of plasma current is caused by excessive impurity levels and toroidal field errors. Upper traces: typical loop voltages 20 V/div. Lower traces: typical plasma currents 5 kA/div. Horizontal axis: time 500 μs/div.

a. Discharge Cleaning

We began by discharge cleaning the machine with a 30-kHz cw oscillator tied in to the OH coils for 15-35 hours per week. This technique continually keeps the gas ~0.1% ionized with the aid of a small dc toroidal magnetic field. Bombardment of the chamber walls by the weakly ionized gas then gradually drives off unwanted impurities. The vacuum chamber had been open to the air for several months during the spring of 1975 and it was likely that large quantities of water vapor had been adsorbed on the chamber walls. These "impurities" were at least partly responsible for the rapid quenching of the plasma current that we observed.

b. Correction of Toroidal Field Errors

Small errors in the toroidal magnetic field were also responsible for Versator's poor operating performance. It is well known that in Tokamak plasmas error fields of the order of a few gauss may upset the stability of the plasma loop enough to drive it into the walls in the early stages of the discharge and may hinder the development of a current channel.[1-3] Versator is equipped with horizontal and vertical field correction coils, as well as diagnostics for sensing the up/down or radially in/out motion of the plasma loop. The horizontal field was adjusted until the up/down motion of the plasma loop appeared to be stabilized. The vertical field is not only required for cancellation of vertical field errors but also for preventing radial expansion of the plasma loop during the current pulse. The in/out inductive diagnostics aided us in properly adjusting the strength of the vertical field.

c. Unstable Operating Conditions

Near the end of October 1975, by discharge cleaning and magnetic field corrections, we achieved great improvements. The current pulse was lengthened to 8-12 ms, with maximum currents of ~5 kA. Plasma current and loop-voltage oscillograms that are typical of these discharges are shown in Fig. XII-42. We found these conditions to be strongly dependent on the strength of the high-voltage OH pulse. A high-voltage OH pulse of 2.2 kV achieved the desired results, while higher voltages caused rapid quenching of the discharge. It was also necessary to use high low-voltage OH pulses of at least 700 V (the maximum voltage available on the low-voltage OH is 825 V) to maintain the plasma current pulse for at least 8 ms.

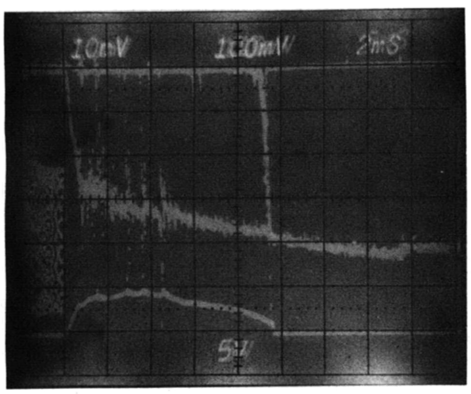

Fig. XII-42.

Typical unstable operating conditions. Hard x-ray emission, loop voltage, and plasma current vs time. The current has reached the Kruskal-Shafranov limit. Upper trace: hard x-ray detector 10 mV/div. Middle trace: loop voltage 10 V/div. Lower trace: plasma current 5 kA/div. Horizontal axis: time 2 ms/div.

d. Presence of Instabilities

It was evident that this discharge had some MHD instabilities associated with it. The spikes in both the loop voltage and the plasma current indicated the presence of instabilities and that rapid cooling of the plasma was associated with them. The other diagnostics confirmed the presence of unstable conditions during these spikes. The visible spectrometer showed maxima in visible light emitted from the plasma during these unstable conditions, while the Langmuir probe indicated local density variations by a factor of two in the plasma column. Large bursts of hard x rays were also emitted from the chamber during these unstable events. These emissions occurred as runaway electrons, created near the beginning of the current pulse, were dumped into the walls of the vacuum chamber by large amplitude oscillations of the plasma loop. An x-ray dosimeter placed next to the torus registered ≤ 5 μrad/shot. Energies ranged up to 400 keV. This last fact indicates that the runaway electrons, by which the x rays are created, are generated near the beginning of the current pulse.

e. Stable Conditions

In order to stabilize the plasma loop, it was necessary to use higher toroidal fields and much lower low-voltage OH voltages. Typical stable discharge current and loop-voltage pulses are shown in Fig. XII-43. The current pulse, which lasts approximately 8 ms, is not as long-lived as in the previous unstable discharges. The smoothness of these oscillograms suggests the absence of extreme MHD instability. The other diagnostics qualitatively confirms this hypothesis. Although we have just recently begun to explore this stable regime of discharges, it appears that the strength of the toroidal magnetic field is a critical factor in maintaining stability. Thus far we have been unable to create stable discharges repeatably for a toroidal field of less than (~5) kG. The maximum field available on Versator at the present time is (5.9) kG. (We expect that this will be increased to (13.2) kG by April 1976.)

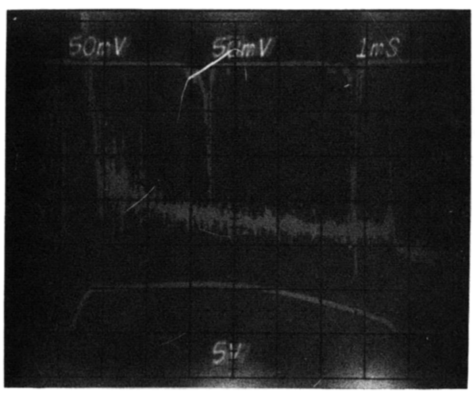

Fig. XII-43.
Typical stable operating conditions. Hard x-ray emission, loop voltage, and plasma current vs time. Upper trace: hard x-ray detector 500 mV/div. Middle trace: loop voltage 5 V/div. Lower trace: plasma current 5 kA/div. Horizontal axis: time 1 ms/div.

f. Comparison of Stable and Unstable Conditions

Preliminary measurements show that the maximum current during stable discharges is roughly proportional to $B_{toroidal}$. Unstable discharges reach comparable maximum currents but have decidedly lower temperatures. Computer modeling of the Versator plasma[4] has shown that plasma electron temperature T_σ derived from the Spitzer conductivity[5] obeys the expression

$$T_\sigma \text{ (in eV)} \cong 1.0\ (I/V)^{2/3},$$

where I is the plasma current in amperes and V is the loop voltage in volts. Using this expression for T_σ, in Fig. XII-44 we plot the maximum plasma temperature against $B_{toroidal}$ for an early run of both stable and unstable discharges. In the regime where it is possible to obtain stable discharge conditions the maximum temperature is approximately twice that obtained during unstable conditions. The highest temperature attained thus far is at least 120 eV, with a main field of (5.8) kG. The plasma energy confinement time τ_E is given by

$$\tau_E = \frac{2\pi^2 a^2 RnT}{IV},$$

where a is the radius of the plasma column, R is the major radius of the torus, n is the average number density, T is the temperature in energy units, I is the plasma current, and V is the loop voltage. For a temperature of 120 eV and an assumed density of 10^{13} cm^{-3}, this discharge has an energy confinement time of from 0.4 to 1.6 ms for a plasma radius of 5-10 cm, respectively.

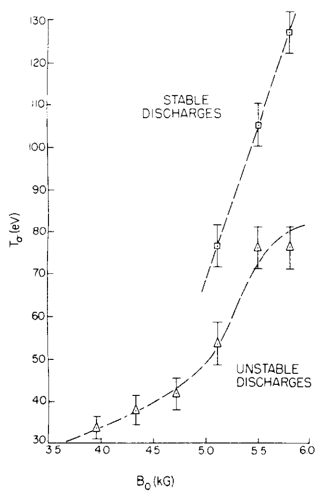

Fig. XII-44.
Electron temperature derived from Spitzer conductivity vs toroidal magnetic field for a typical early run on Versator.

g. Reasons for Unstable Conditions — Kruskal-Shafranov Limit

The unstable discharges described by Fig. XII-42 were obtained by raising the low-voltage OH pulse to a much higher value than that for stable conditions. By overdriving the plasma current in this way, we exceeded the Kruskal-Shafranov limit for MHD stability of the plasma column,[6,7] thereby driving the plasma unstable. The criterion for the onset of this instability is $q \lesssim 3$, where

$$q = \frac{B_{toroidal}}{B_{poloidal}} \frac{a}{R}.$$

Using appropriate values of these parameters for Versator, we have

$$q = 9.2 \frac{B_{toroidal}}{I} \frac{a^2}{100},$$

where I, the plasma current, is in kA, $B_{toroidal}$ is in kG, and a is in cm.

h. Implication of the Presence of a Narrow Current Channel

If we assume $q \lesssim 3$ during all unstable discharges, then a is found to be roughly constant and equal to 5.0 cm for unstable discharges with 2.5-5.0 kA currents and main fields of 4.0 to 5.8 kG, respectively. This implies that the stable plasma loop also has a minor radius of 5.0 cm and, by overdriving the current, the Kruskal-Shafranov limit is exceeded and the plasma becomes unstable.

The minor radius of the vacuum chamber is 14 cm, and hence we should obtain ideally a current density profile with a radius ~10 cm. We suspect that the presence of impurities is responsible for the current profile being much narrower than expected. These impurities come off the chamber walls during the discharge, and so greatly enhance plasma resistivity near the walls that the current is forced to flow in a narrow central channel.

References

1. D. A. Spong and J. F. Clarke, "Runaway Electron Dynamics," Report ORNL-TM-4432, 1973.
2. D. A. Spong, J. F. Clarke, and J. A. Rome, "Relativistic Electron Production in the ORMAK Device," Report ORNL-TM-4120, 1973.
3. J. A. Rome, "Effects of Magnetic Field Errors in ORMAK," Report ORNL-TM-3880, June 1972.
4. A. S. Fisher, "A Computer Model of Field and Heat Diffusion in Versator," S.B. Thesis, Department of Physics and Department of Electrical Engineering, M.I.T., May 1974.
5. L. Spitzer, Physics of Fully Ionized Gases (John Wiley and Sons, Inc., New York, 1962).
6. V. D. Shafranov, "Plasma Equilibrium in a Magnetic Field," in Reviews of Plasma Physics, Vol. II (Consultants Bureau, New York, 1966).
7. H. P. Furth, J. Nucl. Fus. 15, 487 (1975).

8. THERMIONIC CATHODE, LOW-PRESSURE DISCHARGE

U.S. Energy Research and Development Administration (Contract E(11-1)-3070)

Leslie Bromberg, Louis D. Smullin

Introduction

The theory of glow discharges has been limited mainly to cylindrical positive columns. For high pressure the ambipolar theory of Schottky[1] is used, and for low pressures the free-fall theory of Tonks and Langmuir[2] is appropriate. The purpose of these theories, however, is to explain the gradients (axial and radial) and the general characteristics of the discharge with an assumed creation rate.

The problem of obtaining I-V curves in low-pressure discharges has not been addressed in published works. In the high-pressure discharges it has been accomplished when V is the voltage across the positive column but not the entire anode-cathode voltage.

This report describes an attempt to obtain theoretical I-V curves for a source, the multifilament arc (MFA), designed and built at the Lawrence Livermore Laboratory. These sources, which have been described elsewhere,[3] provide a quiescent plasma that has been used to form neutral beams of excellent quality.

Particle Conservation

In the steady state the ion conservation equation reduces to

$$\oint_S n_i\underline{v} \cdot \hat{n}\, da = \int_V d^3\underline{r}\, n_o \int d^3\underline{v}\, f\sigma_i v, \tag{1}$$

where $n_i v$ is the ion flux, $\hat{n}$ the normal to the surface of the walls, f the electron distribution function, and n_o the neutral gas pressure. A similar equation applies to the electrons. Under the assumption that the primaries remain distinct from the bulk of the electrons, Eq. 1 can be expanded. Thus

$$\oint_S n_i\underline{v} \cdot \hat{n}\, da = \underbrace{\frac{I}{e}\left\langle \frac{1 - e^{-s\left(\frac{1}{\ell_i} + \frac{1}{\ell_*}\right)}}{1 + \frac{\ell_i}{\ell_*}} \right\rangle}_{\text{ionization by primaries}} + \int_V d^3\underline{r}\, n_o \underbrace{\int}_{\substack{\text{by plasma}\\ \text{electrons}}} d^3\underline{v}\, f_e \sigma v, \tag{2}$$

where f_e is the cold-electron distribution, I the primary current, the average $\langle\ \rangle$ is over the possible particle trajectories, and ℓ_i and ℓ_* refer to ionization and excitation mean-free paths. In Eq. 2 it is assumed that the primaries can only either ionize or excite once. This is a good assumption, realizing that once they lose the ionizing or exciting energy, the mean-free path for ionizing or exciting of the slower primaries increases because the cross sections are smaller.

When ambipolarity is written so that

$$\oint da \underbrace{\int}_{\substack{\text{escape}\\ \text{electrons}}} f_e\underline{v} \cdot \hat{n}\, da = \oint n_i\underline{v} \cdot \hat{n}\, da \tag{3}$$

the cold-electron population automatically satisfies its conservation equation. In general

Eq. 3 requires the potential between the wall and the plasma to make ion and electron losses equal (floating potential).

The ion loss has been given by Carusso[4] as

$$\oint n_i v \cdot \hat{n}\, da = 0.345\, n_i(0) \left(\frac{2kT_e}{M_i}\right)^{1/2} A_w, \tag{4}$$

where $n_i(0)$ is the maximum ion density, and T_e is the electron temperature. This equation is based on a Maxwellian distribution for the electrons. Note that Eq. 4 is independent of wall potential. The absence of gradients (except near the wall) allows us to identify A_w as the wall area of the source. The influence of a hot-electron component (in this case, the primaries), has been analyzed by using the theory of Demirkhanov.[5] In this case, however, it changes the result less than 6%.

In the case when f_e is not a Maxwellian, this equation yields an "average" energy which will be identified as T_e.

When the temperature is low, or a non-Maxwellian distribution with a depleted tail exists, ionization will only be due to the primaries and Eq. 4 becomes

$$0.345\, n_i \left(\frac{2kT_e}{M_i}\right)^{1/2} A_w = \frac{I}{e} \left\langle \frac{1 - e^{-s\left(\frac{1}{\ell_i} + \frac{1}{\ell_*}\right)}}{1 + \frac{\ell_i}{\ell_*}} \right\rangle. \tag{5}$$

The proper average in Eq. 5 has been done, by using a Monte Carlo simulation.

Cathode Equation

F. W. Crawford[6] has analyzed the case wherein a plane cathode adjacent to a plasma is emitting under space-charge-limited conditions. He finds that the electric field is only large within a few Debye lengths of the emitting surface. In the MFA the Debye length is smaller than the radius of the cathode wire, and hence the plane-wave theory should be applicable.

The result is simply an application of space-charge-limited conditions at the plasma edge and at the cathode surfaces, and use of the Bohm criteria. The equation for the cathode current is

$$I = eA_k n_e \left(\frac{kT_e}{2\pi m_e}\right)^{1/2} J_o\left(\frac{eV_k}{kT_e}\right), \tag{6}$$

where A_k is the cathode area, and n_e is

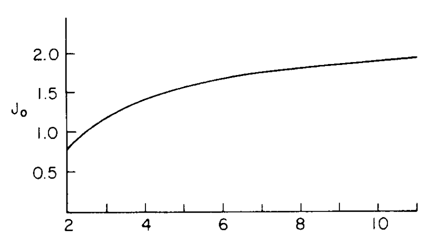

Fig. XII-45. $J_o(x)$ vs x. (From Crawford and Cannara.[6])

the plasma electron density. The function $J_o(x)$ is shown in Fig. XII-45.

Equation 6 is also based on the assumption of a Maxwellian electron distribution. Its validity is not seriously affected by the absence of the tail, as long as the bulk is Maxwellian. This consideration is not true for the plasma ionization term in Eq. 2 or the excitation term in Eq. 7 because these processes depend on the high-energy tail.

We used Eq. 6 to generate I-V curves from published densities of the Berkeley source[3] and compared them with the experimental curves that also were published by Baker and his co-workers.[3] The agreement is better than 30%. One probable reason for the discrepancy is that the temperature is not well known experimentally.

Energy Equation

If it is possible to ignore plasma heating arising from beam-plasma oscillations, then the only heat input to the plasma is through Coulomb friction. We are not ignoring the possibility of a beam-plasma interaction, but we are testing the assumption that a model based on Coulomb friction alone can predict experimental results.

In this case, the conservation of power for the plasma is

$$P_{\text{input}} = \oint_S \langle w_i \rangle\, n_i \underline{v} \cdot \hat{n}\, da + \oint_S da \int d^3\underline{v} \left(\frac{1}{2} m_e v^2 - eV_f\right) f_e \underline{v} \cdot \hat{n}$$

$$+ \int_V d^3\underline{r}\, n_o \int d^3\underline{v}\, f_e v(\sigma_i T_i + \sigma_* E_*), \tag{7}$$

where V_f is the potential difference between the wall and the plasma, and the last terms represent the power lost because of ionization and excitation. As in Eq. 2, we assume that the electron distribution is depleted of high-energy electrons, and hence both ionization and excitation by the plasma electrons can be neglected.

For the case wherein the walls are floating, the electron contribution to Eq. 7 is small. This can be understood by noting that most of the electron energy has been given up to the retarding field of the sheath. $\langle w_i \rangle$ is the average energy of an ion as it is collected by the walls. For a hydrogen plasma this energy is between 2 and 4 times the electron temperature.

The power input, rate of energy transfer by Coulomb friction,[7] is given by

$$P_{\text{input}} = \left\langle I \frac{3 \ln \Lambda}{4\pi} \frac{m_e}{u_p^2} \frac{\omega_{pe}^4}{n_e} s \right\rangle, \tag{8}$$

where the mean-free path for energy exchange is assumed large compared with the length of the system. The average in Eq. 8 is over the possible primary trajectories and has also been calculated by using a Monte Carlo simulation. In the case of low pressure, when the exponential term in Eq. 5 can be replaced by the first two terms of the Taylor expansion,

$$\langle s \rangle_{\substack{\text{Energy}\\ \text{Exchange}}} = \langle s \rangle_{\text{Ionization}}.$$

The power conservation equation is

$$\frac{3 \ln \Lambda}{4\pi} \frac{m_e \omega_{pe}^4}{u_p^2 n_e} I \langle s \rangle_E = \langle w_i \rangle \oint n_i \underline{v} \cdot \hat{n}\, da = \langle w_i \rangle \frac{I}{e} \left\langle \frac{1 - e^{-s\left(\frac{1}{\ell_i} + \frac{1}{\ell_*}\right)}}{1 + \frac{\ell_i}{\ell_*}} \right\rangle. \tag{9}$$

In the calculations, we set $\langle w_i \rangle = 2.9\ T_e$, which would be the case if the plasma were Maxwellian.

Discussion

If we set $n_e = n_i$ (the primary density is an order of magnitude lower than n_e), then Eqs. 5, 6, and 9 are a closed set for T_e, I, and n_e. The ion saturation current is given as

$$j_i = 0.345\ n_i \left(\frac{2kT_e}{M_i}\right)^{1/2}.$$

Solutions for hydrogen and deuterium are given in Figs. XII-46 and XII-47. The neutral gas pressure (n_o), which was only estimated by Baker,[3] was varied until the value of the current at V = 45 V became 1000 A. Once this is set, no more parameters are varied. Figure XII-47 was drawn for the same gas pressure as in Fig. XII-46 and the only published point agrees with the theoretically predicted curve.

Two things should be pointed out. First, in the calculations we took into account the possibility of multiple passes of the primary electrons. This occurs when the primaries bounce from a floating wall at an angle. Second, the calculated values of T_e were large enough (in some cases, at least) that had the Maxwellian assumption for the electron distribution been kept, the plasma creation in Eq. 2 would have been very large and no stable solution could have been found for the temperature.

Heating Rate

If we assume, then, that heating is due to friction between primaries and cold electrons, then it is of interest to calculate the heating rate. If the electron collision times and the electron heating times are large compared with the excitation rate, the high-energy tail of f_e will be depleted.

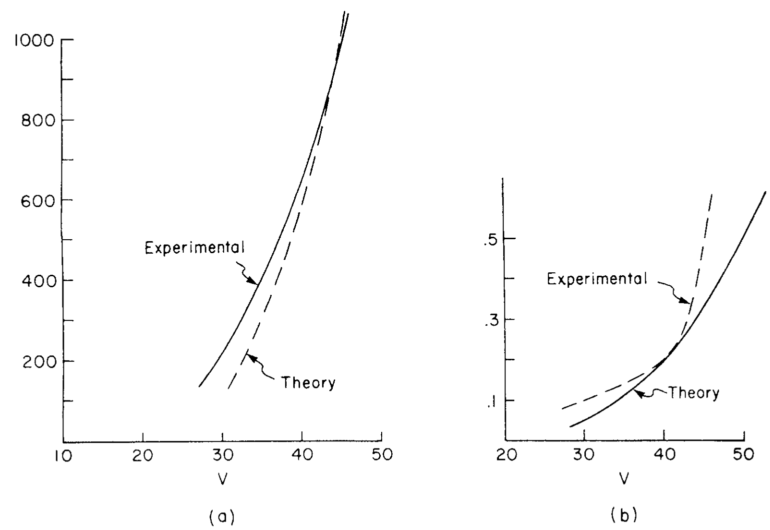

Fig. XII-46. (a) Arc current for a hydrogen discharge. The neutral gas pressure was adjusted until the experimental and theoretical curves agree at 45 V.
(b) Ion saturation current for a hydrogen discharge.

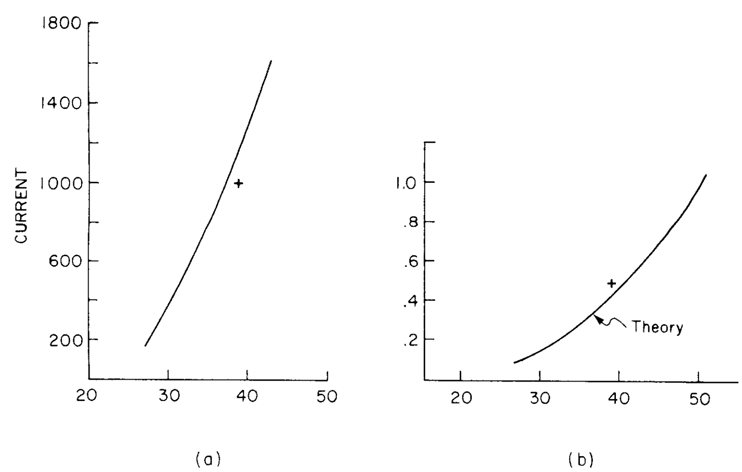

Fig. XII-47. (a) Arc current for a deuterium discharge. The cross is an experimental point.
(b) Ion saturation current for a deuterium discharge. The cross is an experimental point.

Simple calculations show that $\tau_{ee} \approx 1\ \mu s$ and $\tau_* \approx 0.15\ \mu s$ for a 20 eV electron. Clearly, self-collisions will not be able to sustain the tail, since it takes a few collision times to fill it.[8]

The heating rate can be calculated by setting the energy lost by fast electrons equal to the energy input to cold electrons. That is,

$$\frac{d}{dt}\left(\frac{3}{2}nkT_e\right) = I\,\frac{3\ln\Lambda}{4\pi}\,\frac{m_e}{u_p^2}\,\frac{\omega_{pe}^4}{n_e}\langle s\rangle_E. \tag{10}$$

The heating rate calculated from Eq. 10 is substantial, but not enough to keep a long tail.

To see the effect on the distribution function, we solved the Boltzmann equation approximately. Because of the long thermalization time, we neglected it. In the tail the most important processes are frictional heating and energy loss caused by excitation. Under the assumption of a cross section that is a constant for energies larger than the threshold (not a bad approximation for the Lyman-alpha line), the Boltzmann equation for energies larger than the excitation reduces to

$$-a\frac{\partial f_e}{\partial v} - n_o f_e(v)\, v\sigma_* = 0, \tag{11}$$

where

$$a = -n_p\,\frac{4\pi e^4\ln\Lambda}{m_e^2}\,\frac{\partial}{\partial u}\left[\frac{1}{u}\,\Phi\left(u\left(\frac{m_e}{2kT_e}\right)^{1/2}\right)\right]\Bigg|_{u_p}.$$

Here Φ is the error function and u_p is the speed of the primaries. In deriving Eq. 11 we supposed that the electron distribution decreases rapidly with energy.

Solving Eq. 11, we find that the tail of the distribution function is approximately Gaussian, with a "temperature" (different from the temperature of the bulk) given by

$$kT_e \approx \frac{m_e a}{n_o\sigma_*}.$$

This temperature is so low that, as a consequence, the tail will not exist.

Conclusion

The predicted curves agree reasonably well with experimental data. The assumption of no tail to f_e is shown to be self-consistent.

The basic assumption of Coulomb heating as the power input to the plasma was the only available alternative for solving the problem. The nonlinear theory of beam-plasma discharges is still at the stage where definite answers to the efficiency of the coupling cannot be given.

We tried to use the results of Shapiro,[9] based on the quasi-linear theory. Here the power input is independent of the plasma parameters, and the system of equations cannot be solved for I or n_e (all of the equations contain the ratio I/n_e).

References

1. W. Schottky, Phys. Z. 25, 635 (1924).
2. L. Tonks and I. Langmuir, Phys. Rev. 34, 876 (1929).
3. W. R. Baker et al., in Proc. Fifth Symposium on Engineering Problems of Fusion Research, Princeton University, 1973.
4. A. Carusso and A. Cavaliere, Nuovo Cimento 26, 1389 (1962).
5. R. A. Demirkhanov, Yu. V. Kursanov, and L. P. Skripal, Sov. Phys. — Tech. Phys. 19, 891-894 (1975).
6. F. W. Crawford and A. B. Cannara, S.U.-M.L. Report No. 1261, Microwave Laboratory, Stanford University, Stanford, California, November 1964.
7. B. A. Trubnikov, in Reviews of Plasma Physics, Vol. 1 (Consultants Bureau, New York, 1965).
8. W. M. MacDonald, M. N. Rosenbluth, and W. Chuck, Phys. Rev. 107, 350-353 (1957).
9. V. D. Shapiro, Sov. Phys. — JETP 17, 416 (1963).

9. NEUTRAL BEAM INJECTION SYSTEMS

U.S. Energy Research and Development Administration (Contract E(11-1)-3070)

Peter T. Kenyon, Louis D. Smullin

Since the report in Progress Report No. 116 (pp. 78-85), we have extended the range of our measurements in arc power and have studied the effect of varying cathode geometry. We have studied two geometries: a tapered cathode, and 4 "magnetron" (cylindrical) cathodes. Figure XII-48 gives the dimensions of these structures. All cathodes are unipotential, oxide-coated, and are run in the space-charge-limited regime.

The extracted ion current density is plotted in Fig. XII-49 as a function of input arc power for several of these geometries. We have excluded the cathode with the largest diameter ($D_\ell = 2.2$ cm), since it performed poorly with respect to plasma density, and hence we took very little data. We do not yet understand why it behaves so poorly and we shall report on it later. The poor performance of this cathode led us to construct a long slender cathode which has proved to be the best performer in terms of ion current density vs arc power, as is shown in Fig. XII-49.

We have observed that the plasma expands from the cathode in a bottle-shaped

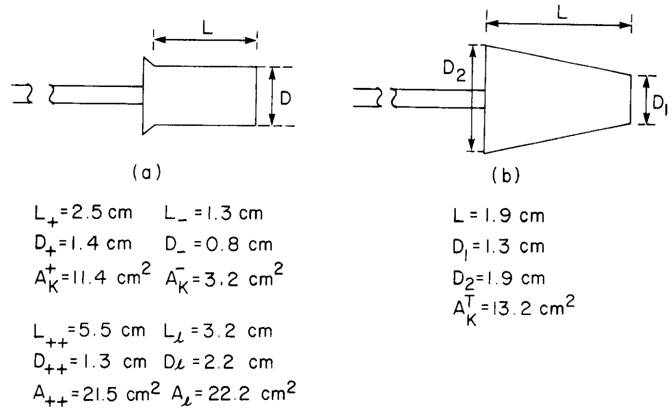

Fig. XII-48. Cathode geometry and dimensions: (a) magnetron cathode, (b) tapered cathode.

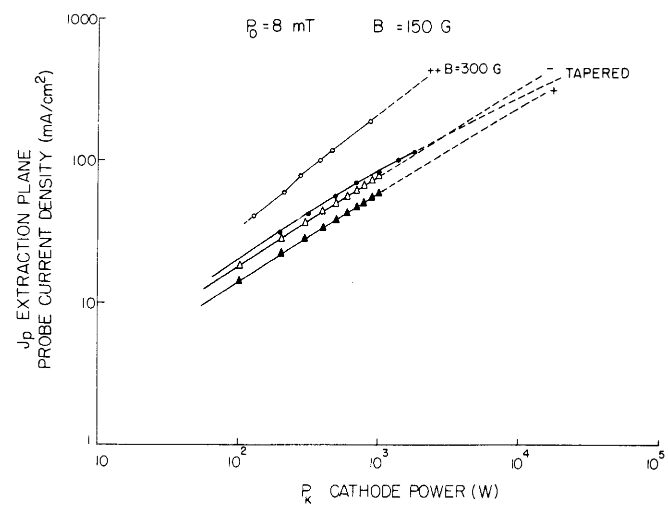

Fig. XII-49. Ion probe current density vs input power for three magnetron cathodes (L_{++} = 5.5 cm, L_{-} = 1.3 cm, L_{+} = 2.5 cm), and the tapered cathode.

configuration (roughly along the diverging solenoidal field lines). This is shown in Fig. XII-50, which gives a comparison of on- and off-axis measurements of ion currents.

The "magnetron" cathode offers the advantage of relatively high impedance. Figure XII-51 shows the I_K vs V_K characteristics with variations in solenoidal fields. These curves indicate the possibility of injecting high beam power at relatively high voltages and lower currents. This permits the use of smaller and simpler cathodes. In the multifilament arc experiment,[1] the discharge voltage ≈ 50-60 V and requires 200-2000 A currents; if operation of 250 V were equally power efficient, the cathode size (and hence heater power) could be reduced by approximately 5.

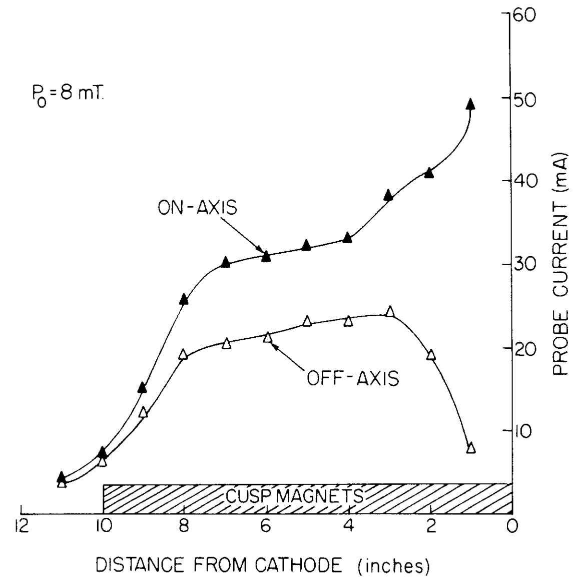

Fig. XII-50. Ion probe current vs distance from the cathode for on- and off-axis measurements showing the plasma expansion characteristics.

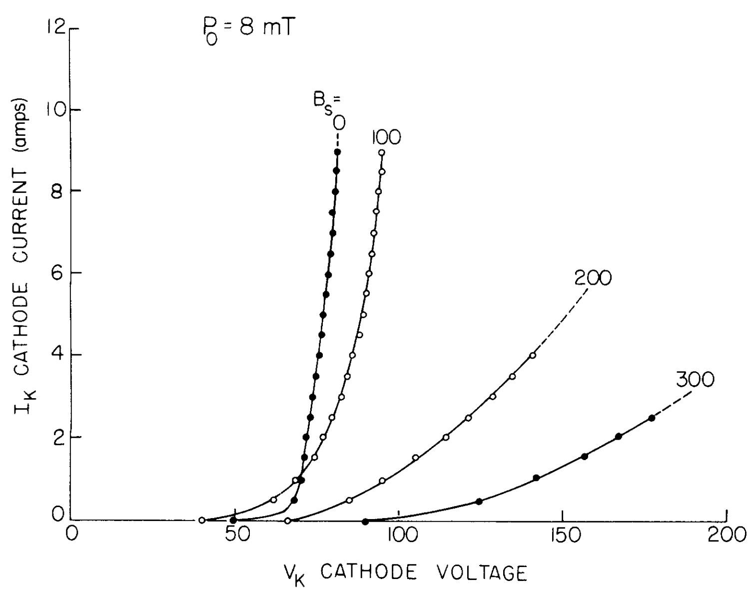

Fig. XII-51. I_K vs V_K characteristics for a magnetron cathode (L_+ = 2.5 cm).

All measurements have been made with single-electrode Langmuir probes. Figure XII-52 shows the electron energy distribution near a floating grid that terminates the discharge, for various distances of the grid from the cathode plane. It can be seen that the distribution has at least two temperatures and that both temperatures decrease at greater distances from the cathode. We believe that there may be a substantial drift component of velocity because of the $\nabla|\underline{B}|^2$ "forces". The existence of such a drift can be determined by utilizing either a velocity analyzer or a two-electrode Langmuir probe. This measurement is now being prepared for our experiment.

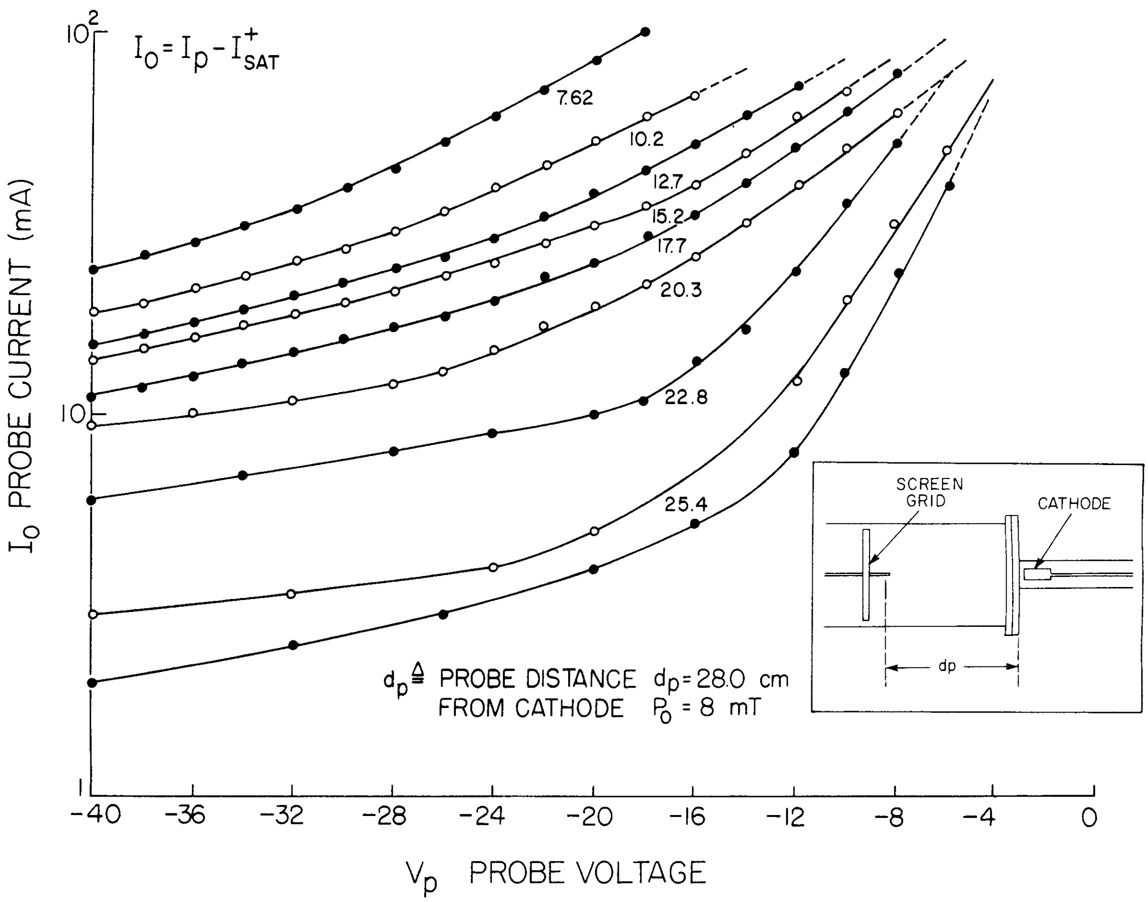

Fig. XII-52. Ion current vs probe voltage for a magnetron cathode ($L_- = 1.3$ cm).

When the tapered cathode was used, we observed RF output up to 3-4 GHz, corresponding to f_p for the observed density. The oscillations cover a very wide band and have the noisy structure typical of beam-plasma oscillations. The oscillations were observed with a wide range of solenoid field strength. In contrast, the cylindrical (magnetron) cathode exhibited such oscillations only for $B \lesssim 100$ G, and nothing above this.

We believe that the low-field oscillations resulted from a radial beam-plasma oscillation, but at higher fields the tighter orbits of the primaries are not consistent with f_p oscillations.

The electron "temperature" (Fig. XII-52) has been measured also for the tapered cathode and is essentially indistinguishable from that of the magnetron cathode. Thus it appears that in both systems the primary beam is "thermalized" in a region close to the cathode where a fairly warm secondary plasma is also produced. If the important mechanism for the tapered cathode is f_p beam-plasma oscillations, we have no corresponding mechanism for the cylindrical cathode except a long dwell time for primaries circling the cathode before drifting into the plasma chamber.

References

1. K. W. Ehlers et al., "Large Area Plasma Sources," Proc. Second Symposium on Ion Sources and Formation of Ion Beams, University of California, Berkeley, 1974.